

ABSTRACT

RYU, GYUNGHYUN. Co-doping Strategies for Controlling Electrical Conduction in Oxide Materials (Under the direction of Elizabeth C. Dickey).

The objective of this dissertation is to understand the fundamentals of the electrical conduction mechanisms and defect chemistry of two important dielectric materials, BaTiO₃ ceramics and wide band gap β -Ga₂O₃ single crystals, with the goal of identifying co-doping strategies that can limit both electronic and ionic conductivity over large oxygen activity ranges.

The conductivity behaviors of several acceptor-doped and (acceptor + donor) co-doped BaTiO₃ ceramics are studied as a function of temperature and oxygen partial pressure (pO_2). The (Mn + Y) co-doped compositions exhibit the lowest insulating bulk conductivity over a wide range of temperatures in air. Moreover, a pO_2 -independent bulk conductivity is obtained over the pO_2 range $10^{0.68}$ atm (air) – 10^{-4} atm across the measurement temperature range of 500 °C to 900 °C. This particular (Mn + Y) co-doped BaTiO₃ composition also exhibits no significant time-dependent electrical degradation at 500 °C under 45 V/cm DC electric field. The pO_2 -independent electrical conductivity is believed to arise from the multivalent nature of Mn.

The insulating electrical conductivity of Fe-doped (010) β -Ga₂O₃ single crystals are similarly studied over a wide range of temperatures and pO_2 . The oxygen partial pressure (pO_2)-invariant electrical conductivity is also observed in this system over the pO_2 range of $10^{0.68}$ atm (air) – 10^{-4} atm from 600 °C to 800 °C. The charge neutrality equation explains that the pO_2 -independence of electrical conductivity originates from the low concentration of intrinsic point defects and acceptor (Fe) and donor (Si) mutual compensation, leading to the Fermi level pinning.

© Copyright 2021 by Gyunghyun Ryu

All Rights Reserved

Co-doping Strategies for Controlling Electrical Conduction in Oxide Materials.

by
Gyunghyun Ryu

A dissertation submitted to the Graduate Faculty of
North Carolina State University
in partial fulfillment of the
requirements for the degree of
Doctor of Philosophy

Materials Science and Engineering

Raleigh, North Carolina
2021

APPROVED BY:

Dr. Elizabeth C. Dickey
Committee Chair

Dr. Douglas Irving

Dr. Ramón Collazo

Dr. Jesse Jur

BIOGRAPHY

Gyunghyun Ryu attended the Changwon National University in South Korea from 2006 to 2014, where he completed his B.Sc. and M.Sc. in Materials Science and Engineering. During his time there, he worked in Myong-Ho Kim's research group studying the ferroelectric and piezoelectric properties of ABO_3 materials. In 2015, he joined in Jon-Paul Maria's group at NC State University as a visiting scholar for 3 months. Then, he started his Ph.D. degree in Materials Science and Engineering at NC State University in 2016, under the direction of Elizabeth C. Dickey.

ACKNOWLEDGMENTS

I would like to thank to my advisor Beth Dickey. I was very pleased to be offered a RA position, and still remember that you said “Ryu, you did amazing jobs in your first year”. This enables me to finish my PhD degree successfully in our group. Your support for my PhD degree is really appreciated. I am also thankful to our group members: Dr. Biya Cai, Dr. Daniel Long, Dr. Nicole Creange, Dr. Matthew Cabral, Dr. Carolyn Grimley, Neal Lewis, John McGarrahan, Stephen Funni, Corrado Harper, Steven Baro, Andrew Auman. Especially, John, our discussions were always interesting and helpful, and you made significant contribution to our sputtering system, pO_2 system, lab safety and etc. I would like to thank to my committee members, Prof. Douglas Irving, Prof. Ramón Collazo, and Prof. Jesse Jur. Thank you for your feedback on my work. I want to express my thanks to my collaborators: Prof. Jon-Paul Maria, Dr. Pramod Reddy, Dr. Preston Bowes, George N. Kotsonis. I thank to Prof. Clive Randall, Prof. Soonil Lee, Prof. Myong-Ho Kim, Dr. Jonathon Baker, Yifeng Wu who gave me great discussion for my PhD works. I also thank to AIF staff members: BB and Elaine Zhou and MSE department staff member: Edna Deas. Finally, my family and friends, your sincere supports helped me a lot to endure my hard time and to finish my degree successfully.

This work was predominantly supported by the Air Force Office of Scientific Research under grant number FA9550-19-1-0222. This work was partially supported by the II-VI Foundation under the Block-Gift Program. In addition, this work was performed in part at the Analytical Instrumentation Facility (AIF) at North Carolina State University, which is supported by the State of North Carolina and the National Science Foundation (award number ECCS-1542015). The AIF is a member of the North Carolina Research Triangle Nanotechnology Network (RTNN), a site in the National Nanotechnology Coordinated Infrastructure (NNCI).

TABLE OF CONTENTS

LIST OF TABLES	vi
LIST OF FIGURES	vii
Chapter 1: Introduction	1
1.1..General background.....	1
1.2..Statement of the problems.....	4
1.3..Objectives.....	6
Chapter 2: Background and Literature Review	8
2.1. Defect chemistry in BaTiO ₃	8
2.1.1. Electronic equilibrium.....	8
2.1.2. Oxygen exchange reaction	9
2.1.3. Full Schottky reaction	10
2.1.4. Partial Schottky reaction	10
2.1.5. Charge neutrality condition	13
2.2. Electrical conductivity in BaTiO ₃	17
2.2.1. Acceptor doped BaTiO ₃	17
2.2.2. Co-doped BaTiO ₃	23
2.3. Degradation behavior in BaTiO ₃	26
2.4. Thermally stimulated depolarization current (TSDC) BaTiO ₃	28
2.5. Defect chemistry and electrical conductivity of β -Ga ₂ O ₃	33
Chapter 3: Materials and Experimental Procedure	35
3.1. Synthesis of BaTiO ₃ ceramics.....	35
3.2. (010) Fe-doped β -Ga ₂ O ₃ single crystal.....	36
3.3. Four-points-probe DC method	36
3.4. AC impedance	38
3.5. Prediction of defect structure	39
Chapter 4: Electrical Conductivity of Mg or Mn Singly Doped BaTiO₃	42
4.1. Introduction.....	42
4.2. Results and discussion	43
4.3. Conclusions.....	54
Chapter 5: Co-doping Strategies for Controlling Electrical Conductivity in BaTiO₃	55
5.1. Abstract.....	55
5.2. Introduction.....	56
5.3. Experimental setup	57
5.4. Results	59

5.5. Discussion	65
5.6. Conclusions	71
Chapter 6: Origin of Electrically Semi-Insulating Properties of Fe-doped β-Ga₂O₃.....	72
6.1. Abstract	72
6.2. Introduction	72
6.3. Experimental procedure	74
6.4. Results and discussion	75
6.5. Conclusions	82
Chapter 7: Conclusions and Future Works	83
7.1. Conclusions	83
7.2. Future works.....	84
7.2.1. Bulk electrical conductivity of BaTiO ₃	84
7.2.2. Grain boundary effects at low-temperature in BaTiO ₃	86
7.2.3. AC and DC conductivities versus pO_2 at low-temperature in BaTiO ₃	87
REFERENCES	88
APPENDIX.....	100
Appendix A: Crystallization Behavior of BaTiO₃ Thin Films.....	101

LIST OF TABLES

Table 1.1	Material properties of major semiconductors for power device applications.[4,13] .	4
Table 2.1	Pre-exponential factor and enthalpy of defect reactions. Bolded values were used for calculations in sections 2.1.5 and 5.4.....	12
Table 4.1	Activation energy of electrical conduction in Mg or Mn-doped BaTiO ₃	53
Table 5.1	Doping levels and molar ratio of BaTiO ₃	58
Table 5.2	Curie temperature and constant in doped BaTiO ₃	63
Table 5.3	Defect reactions and equilibrium constant.	66
Table 6.1	Thermodynamic parameters for solving a charge neutrality equation.....	79
Table 7.1	Activation energy of bulk conductivity at different temperature range.	85
Table 7.2	Slope in log ₁₀ σ versus log ₁₀ pO ₂ measured by the DC and AC techniques in 0.5 mol% Mn-doped at 500 °C.....	87

LIST OF FIGURES

Figure 1.1	Crystal structure of (a) BaTiO ₃ and (b) β -Ga ₂ O ₃	2
Figure 1.2.	Oxygen vacancy concentration-dependent (a) electronic carrier and ionized Fe concentrations and (b) total and partial electrical conductivities of Fe-doped SrTiO ₃ at 210 °C. The sample was equilibrated at 900 °C and p_{O_2} of 10 ⁻⁵ atm and quenched to room temperature. Reproduced with permission from [19].....	5
Figure 2.1	(a) Full equilibrium defect structure at 1150 °C and (b) partial equilibrium defect structure at 1000 °C with the fixed cation vacancies equilibrated from the high-temperature condition (1150°C and $p_{O_2} = 0.21$ atm) in undoped BaTiO ₃	14
Figure 2.2	Electrical conductivity versus p_{O_2} of undoped BaTiO ₃ ceramics and single crystals at 1000 °C.	15
Figure 2.3	(a) Equilibrium defect structure at 1150 °C and (b) partial equilibrium defect structure at 1000 °C with the fixed cation vacancies (equilibrated at $T_E = 1150$ °C and $p_{O_2} = 0.21$ atm) in single-valent acceptor-doped BaTiO ₃	16
Figure 2.4	Equilibrium electrical conductivity of undoped BaTiO ₃ and Ba(Ti _{1-x} Mg _x)O _{3-x} ($x = 0, 0.001, 0.005, 0.01$) at 1000 °C. Reproduced with permission from [55].	17
Figure 2.5	(a) Equilibrium electrical conductivity of undoped and Al-doped BaTiO ₃ at 1000°C. (b) Apparent net acceptor concentration derived from conductivity data, compared with the amount of added Al. Reproduced with permission from [40]...	18
Figure 2.6	Electrical conductivity of (a) undoped BaTiO ₃ and (b) Mn-doped BaTiO ₃ vs. oxygen partial pressure at different temperatures. Reproduced with permission from [43].....	19
Figure 2.7	(a) Equilibrium electrical conductivity of (Ba _{1-x} Ca _x)TiO ₃ and (BaTiO ₃ + xCaO) with $x = 0.5$ mol% and 2 mol% at 1000 °C. (b) Equilibrium electrical conductivities at 800 °C and 1000 °C of (BaTiO ₃ + xCaO) and Ba(Ti _{1-x} Ca _x)O ₃ with $x = 2$ mol %. Reproduced with permission from [54].	20
Figure 2.8	Mg concentration-dependent room temperature electrical resistivities of Mg-doped BaTiO ₃ sintered in different oxygen partial pressures. Reproduced with permission from [60].	21
Figure 2.9	Doping concentration-dependent Cole-Cole plots of (a) Mg or (b) Mn-doped BaTiO ₃ at 480 °C. Reproduced with permission from [48]	22
Figure 2.10	Equilibrium electrical conductivity at 1000 °C of BaTiO ₃ . Reproduced with permission from [62].....	23

Figure 2.11 Electrical conductivity versus oxygen activity of BaTiO ₃ co-doped by Mn and Y with different donor-to-acceptor ratios $m_d/m_a = 0.0$ (a), 0.5 (b), 1.0 (c), 1.8 (d), and 2.1 (e) at 1000 °C. Reproduced with permission from [64].	24
Figure 2.12 (a) Equilibrium electrical conductivities of BaTiO ₃ co-doped with (a) Ho and Mn (b) Dy and Mn at 1200 °C. Reproduced with permission from [65,66].	25
Figure 2.13 Room temperature resistivities of (Ba _{1-2x} R _{2x})(Ti _{1-x} Mg _x)O ₃ sintered at 1380 °C in a reducing atmosphere as a function of x (R = La, Sm, Dy, Ho, Er or Yb). Reproduced with permission from [14].	26
Figure 2.14 Schematic of (a) experimental procedure of TSDC and (b) analysis of TSDC with various polarization mechanisms. Courtesy of Dr. Clive Randall at Penn State University.	28
Figure 2.15 TSDC spectrum of undoped BaTiO ₃ . Reproduced with permission from [69].	29
Figure 2.16 TSDC plots in Mg-doped BaTiO ₃ ceramics with Mg concentration of (a) 0.003 mol%, (b) 0.01 mol% (c) 0.03 mol% (d) 0.06 mol% (e) 0.1 mol%. (f) Comparison of same magnitude of TSDC peaks of lowest (0.003 mol%) and highest Mg concentration (0.1 mol%) of Mg-doped BaTiO ₃ ceramics. Reproduced with permission from [70].	30
Figure 2.17 TSDC plots for Mn-doped BaTiO ₃ MLCC with (a) 0.2 mol% Mn, (b) 0.35 mol% Mn and (c) 0.5 mol% Mn. Reproduced with permission from [72].	31
Figure 2.18 TSDC plots for Mn and V co-doped BaTiO ₃ MLCC with (a) 0.2 mol% Mn and 0.1 mol% V, (b) 0.2 mol% Mn and 0.3 mol% V, and (c) 0.4 mol% and 0.3 mol% V. Reproduced with permission from [73].	32
Figure 3.1 Comparison of (a) four-point and two-point-probe DC conductivities and (b) contact and sample resistances in Fe-doped β -Ga ₂ O ₃ single crystal at different temperature in air.	36
Figure 3.2 (a) Top view of Fe-doped (010) β -Ga ₂ O ₃ single crystal and sputtered Pt electrodes the black arrow indicates the measurement direction (b) time-dependent four-wire resistance with a change in pO_2 at a given temperature.	37
Figure 4.1 Time-dependent DC electrical conductivity at various oxygen partial pressure in (a) Mg-doped BaTiO ₃ and (b) Mn-doped BaTiO ₃ at 900 °C.	43
Figure 4.2 DC electrical conductivity as a function of oxygen partial pressure in Mg or Mn-doped BaTiO ₃ at (a) 900 °C and (b) 500 °C.	44

Figure 4.3	(a) Cole-Cole plot of Mn-doped BaTiO ₃ as a function of temperature. (b) High-frequency arc and (c) corresponding imaginary part of modulus and real part of relative permittivity at 300 °C.....	47
Figure 4.4	Real part of relative permittivity at various temperature in (a) Mg-doped and (b) Mn-doped BaTiO ₃ . Curie-Weiss fitting in (c) Mg-doping and (d) Mn-doping.....	49
Figure 4.5	Observed and fitted Cole-Cole plots of (a) Mg-doped BaTiO ₃ and (b) Mn-doped BaTiO ₃ at 500 °C.	50
Figure 4.6	Observed and simulated AC formalisms of (a) Mg-doped BaTiO ₃ and (b) Mn-doped BaTiO ₃ at 500 °C.....	51
Figure 4.7	Temperature-dependent DC and AC electrical conductivities of (a) Mg-doped BaTiO ₃ and (b) Mn-doped BaTiO ₃ in air.	52
Figure 5.1	DC electrical conductivity as a function of oxygen partial pressure in doped BaTiO ₃ with 0.1 mol% Ti-rich at (a) 900 °C and (b) 500 °C. (c) The comparison of high-temperature DC electrical conductivity with respect to the amount of Ti-excess.....	59
Figure 5.2	Observed and fitted Cole-Cole plots of (a) Mg-doped (b) Mn-doped (c) (Mg+Y) co-doped and (d) (Mn+Y) co-doped BaTiO ₃ at 500 °C in air. Note that the real and imaginary parts of impedance were scaled by the sample geometry for the direct comparison of impedance magnitudes.....	61
Figure 5.3	Curie-Weiss law fitting in (a) Mg-doped (b) Mn-doped (c) (Mg+Y) co-doped and (d) (Mn+Y) co-doped BaTiO ₃	62
Figure 5.4	Temperature-dependent bulk conductivities, extracted from impedance spectra, and activation energies in air.	63
Figure 5.5	Time-dependent current density at 500 °C under (a) 10 V/cm and (b) 45 V/cm DC electric field.	64
Figure 5.6	Predicted concentration of (a) oxygen vacancy, (b) cation vacancy, and (c) electronic charge carrier at 900 °C in (Mg+Y) co-doped BaTiO ₃ with $[Y_{Ba}^{\cdot}]/[Mg_{Ti}^{\prime\prime}] = 0, 0.5, 1.0, 1.5, \text{ and } 2.0$	67
Figure 5.7	Predicted defect concentration of (a) oxygen vacancy, (b) neutral and ionized Mn, and (c) electron and hole in (Mn+Y) co-doped BaTiO ₃ with $[Y_{Ba}^{\cdot}]/[Mn_{Ti}]_T = 0, 0.5, 1.0, 1.5, \text{ and } 2.0$. at 900 °C.....	69
Figure 5.8	Predicted defect concentration of (a) oxygen vacancy and (b) electron and hole in (Mn+Y) co-doped BaTiO ₃ with $[Y_{Ba}^{\cdot}]/[Mn_{Ti}]_T = 0, 0.5, 1.0, 1.5, \text{ and } 2.0$ at 500 °C.	70

Figure 6.1	Electrical conductivity versus oxygen partial pressure in unintentionally doped β - Ga_2O_3 polycrystalline.	73
Figure 6.2	(a) Cole-Cole plots versus temperature in air and capacitance and imaginary part of modulus as a function of frequency at 500 °C in inset Figure. (b) Temperature-dependent electrical conductivities obtained from the different techniques.	76
Figure 6.3	Temperature dependent (a) carrier concentration and (b) mobility.	77
Figure 6.4	(a) Observed and calculated carrier concentrations versus temperature and (b) predicted Fermi level.	79
Figure 6.5	(a) Oxygen partial pressure dependent DC electrical conductivity at various temperature. (b) DC electrical conductivity versus temperature with change in activation energy (inset Figure) at each $p\text{O}_2$ condition.	80
Figure 7.1	Temperature-dependent bulk conductivity of 0.5 mol% Mg-doped, 0.5 mol% Mn-doped, (0.5 mol% Mg and 1.0 mol% Y) co-doped, and (0.5 mol% Mn and 0.5 mol% Y) co-doped BaTiO_3 compositions in air.	85
Figure 7.2	Temperature dependent bulk and grain-boundary conductivities of (a) 0.5 mol% Mg-doped, (b) 0.5 mol% Mn-doped, (c) (0.5 mol% Mg and 1.0 mol% Y) co-doped, and (d) (0.5 mol% Mn and 0.5 mol% Y) co-doped BaTiO_3 in air.	86
Figure 7.3	DC and AC electrical conductivities versus $p\text{O}_2$ of (a) 0.5 mol% Mn-doped and (b) (0.5 mol% Mn and 0.5 mol% Y) co-doped BaTiO_3 at 500 °C.	87

Chapter 1

Introduction

This dissertation addresses the ionic and electronic defect chemistry of two important dielectric materials, BaTiO₃ ceramics and β -Ga₂O₃ single crystals. These dielectrics have very different structural, thermal, and electrical properties, and are therefore used in different application spaces. However, in some application areas there is a common need for these materials to be electrically insulating over broad temperature and voltage ranges. Such high electrical resistivity can be achieved by co-doping strategies, with both donor and acceptors, that limit electronic conduction. The concept of mutual compensation of donors and acceptors is used in common semiconductors of single crystal or thin film materials to pin the Fermi level.[1] This process is not as straightforward in typical ceramic materials due to the fact that charge compensating mechanisms are more complex in ceramics, which largely results from lower chemical purity and the multitude of possible intrinsic lattice defects in more complex crystal structures. Moreover, the intrinsic defect chemistry and Fermi level are also strongly modified as oxides equilibrate with the external oxygen activity (which can vary by at least six orders of magnitude during the processing and application of a typical BaTiO₃ commercial capacitor). Thus, systematic doping approaches are necessary for BaTiO₃ ceramics to engineer their electrical conductivity. In addition to the basic electrical insulating properties of a dielectric, the stability of the resistivity under applied fields is equally important. In general, dielectric degradation, or a time-dependent increase in leakage current, is associated with the electromigration of charged intrinsic point defects in the material. Thus, it is essential that doping strategies limit the ionic lattice defect concentrations in addition to the electronic carrier concentrations, i.e. both the ionic and electronic conductivities must be minimized. This dissertation aims to understand electrical conduction mechanisms in BaTiO₃ ceramics and β -Ga₂O₃ single crystals with doping or co-doping strategies. This goal of the research is to improve the electrical insulating properties and electrical degradation resistance of BaTiO₃ ceramics. Various measurement techniques such as direct current

(DC) conductivity, alternating current (AC) impedance spectroscopy, and Hall conductivity are utilized to characterize the electrical conductivity as a function of oxygen partial pressure (pO_2) and temperature to understand the defect chemistry of the materials and the effects of acceptor and donor co-doping.

1.1. General Background

$BaTiO_3$ is a ferroelectric material which has an ABO_3 perovskite structure. As shown in Figure 1, the A-site is occupied by the Ba^{+2} ion with the twelve-fold coordination, the B-site is an octahedrally coordinated site occupied by a Ti^{+4} , and the anion site is occupied by O^{-2} . A non-centrosymmetric tetragonal structure of $BaTiO_3$ at room temperature gives rise to a spontaneous polarization along the c-axis, and the resulting ferroelectricity is connected to the high permittivity of $BaTiO_3$. [2] The high permittivity of $BaTiO_3$ enables the material to be used as a capacitor, which can store and release electric charge, thus $BaTiO_3$ is widely used in multi-layer ceramic capacitor (MLCC) applications.

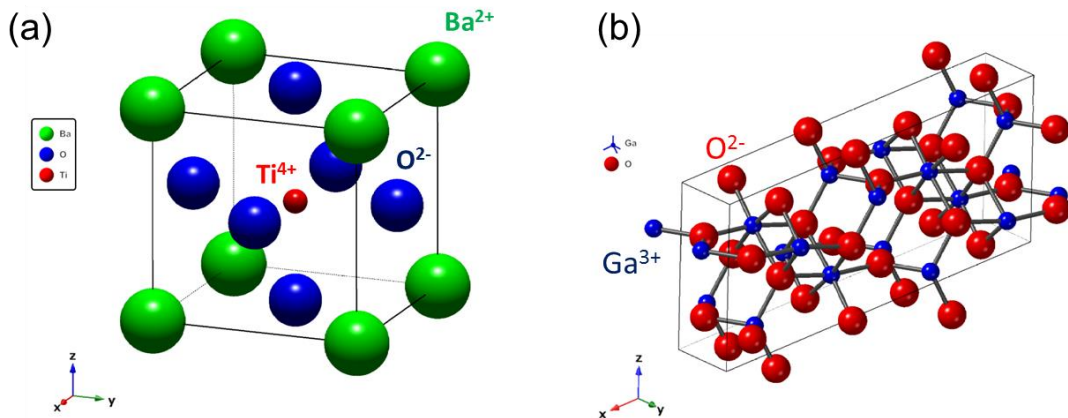


Figure 1.1 Crystal structure of (a) $BaTiO_3$ and (b) β - Ga_2O_3 .

MLCCs are one of the most important components in smartphones, tablets, personal computers and automobiles. [3] As digital technologies develop, there is a gradual increase in demand for MLCCs. Samsung Electro-Mechanics reported that the number of MLCCs required in mobile phones has increased almost 10 times from 2008 to 2018. [3] In addition, around 1,000 MLCCs are used for a computer or LED TV, and more than 10,000 MLCCs are required for an electric vehicle. [3] The performance of MLCCs is highly dependent on the geometry of the

capacitor that is composed of many layers of dielectric and inner electrodes. The capacitance, C , of a MLCC is given by:

$$C = \varepsilon_0 \varepsilon_r \frac{(n-1)A}{d} \quad (1.1)$$

where ε_0 is the permittivity of vacuum, ε_r is the relative permittivity of dielectric, n is the number of stacked inner electrodes, A is the area of electrode, and d is the thickness of the dielectric layers. It is apparent from Eq. (1.1) that the capacitance of an MLCC can be increased by increasing the number of dielectric layers, decreasing the thickness of the dielectric layers or increasing the relative permittivity of the dielectric. Other ferroelectric materials such as (Bi,Na)TiO₃-BaTiO₃, (Na,K)NbO₃, and Pb(Zr,Ti)O₃ based-perovskite materials can be also used for class 2 MLCCs which requires a broad capacitance tolerances and a high permittivity. However, BaTiO₃ is the most appropriate material for class 2 MLCCs due to its high dielectric permittivity, good operational temperature, and its eco-friendly components compared to Pb-based ferroelectric materials.[3]

Monoclinic β -Ga₂O₃ is the most thermodynamically stable phase of Ga₂O₃ in the temperature range of 25 °C – 1800 °C relative to the four other polymorphs of Ga₂O₃, rhombohedral (α), defective spinel (γ), cubic (δ) and orthorhombic (ε).[4] The monoclinic structure of β -Ga₂O₃ is relatively complex as shown in Figure 1.1(b). There are two different Ga lattice sites and three different lattice sites for oxygen. One Ga is octahedrally and the other Ga is tetrahedrally coordinated by oxygen.[5] β -Ga₂O₃ has the $C2/m$ space group with lattice parameters a , b , c , and β are respectively 12.12 – 12.34 (Å), 3.03 – 3.04 (Å), 5.80 – 5.87 (Å), and 103.83 (°).[6]

β -Ga₂O₃ has great advantages for power electronic devices such as transistors and diodes. The band gap is wide between 4.5 and 4.9 eV,[7–9] the electron density can be engineered in the range of $10^{15} \sim 10^{19} /\text{cm}^3$ by Si and Sn doping,[7, 9, 10] and the estimated breakdown field is very large, 8 MV/cm.[11] In Table 1.2, various physical properties of major semiconductors are compared. The Baliga figure of merit (BFOM) defines basic material parameters showing how suitable a material is for power devices, and the higher value indicates the better performance. Although SiC and GaN have attracted attention as key materials for high-efficiency power devices in the near future, β -Ga₂O₃ was proposed to be another promising candidate due to the relatively high BFOM.[4] In addition, Kuramata et al. has successfully grown high-quality β -Ga₂O₃ single crystals from a melt source using the edge-defined film-fed growth (EFG) method,[12] which is

not a possible method for SiC and GaN wafers. This EFG method enables the large volume production of β -Ga₂O₃ single crystals with a fast growth rate, and thus the production cost of devices may be much lower compared to SiC and GaN-based devices.[12]

Table 1.1 Material properties of major semiconductors for power device applications.[4, 13]

Property	Si	GaAs	4H-SiC	GaN	Diamond	β -Ga ₂ O ₃
Bandgap E_g (eV)	1.1	1.4	3.3	3.4	5.5	4.5 ~ 4.9
Relative permittivity ϵ	11.8	12.9	9.7	9.0	5.5	10
Breakdown field E_{br} (MV/cm)	0.3	0.4	2.5	3.3	10	8
Electron mobility μ (cm ² /Vs)	1,400	8,000	1,000	1,200	2,000	300
Baliga's FOM $\epsilon\mu E_{br}^3$	1	15	340	870	24,664	3,444
Thermal conductivity (W/cm·K)	1.5	0.55	2.7	2.1	10	0.27 [010] 0.11 [100]

1.2. Statement of the problem: Dielectric Degradation

With increasing operating voltages and temperatures for dielectrics such as BaTiO₃ and β -Ga₂O₃, several reliability issues have been arising in each community. Although BaTiO₃ ceramics have been a commercially available capacitor material for over fifty years, there are still critical challenges such as dielectric degradation and decrease in dielectric properties with miniaturization.[3] In the past, the inner electrodes were the noble metals such as platinum (Pt) or palladium (Pd), which could be co-sintered with ceramic layers in air at 1300 °C or higher, because the metals are stable with respect to the atmosphere and temperature. However, as the multi-layer technologies have been developing with the miniaturization of MLCCs, the number of inner electrodes increases. This results in the rapid increase in the cost of Pt and Pd. Thus, a variety of inner electrodes have been investigated to reduce the production cost of MLCCs, and the cheap nickel (Ni) or copper (Cu) metals have been used as the inner electrode for 50% or more of MLCCs.[14]

Because Ni and Cu are easily oxidized in air, they have to be co-sintered with the dielectric layers in a reduced oxygen partial pressure environment. This results in the generation of point defects such as oxygen vacancies in the dielectric material during sintering of MLCCs. The

vacancies are compensated by two electrons, which become a major electrically conducting species at room temperature, in turn, making the capacitors electrically conductive. Therefore, the incorporation of acceptors has been widely used to compensate for the excess electrons arising from the oxygen vacancies. This enables the MLCCs to maintain electrically insulating properties at room temperature.

Since the dielectric layers in MLCCs are on the order of a few micron, a typical operation voltage of a few V causes tens of kV/cm electric field within the dielectric layer, eventually initiating electrical degradation (an increase in leakage current) of the MLCC. The phenomenon is regarded as a significant issue in the capacitor community and a lot of studies have been conducted to understand the fundamental mechanisms of degradation in perovskite capacitors.[15–20] The time-dependent degradation has been attributed to the electromigration of point defects such as charged oxygen vacancies under simultaneous temperature and DC field stress, which results in stoichiometry gradients across the dielectric layers. In addition, the prior works show that the concentration of oxygen vacancies are coupled with the electronic carrier concentration[19] as shown in Figure 1.2, therefore, limiting both electronic and ionic conductivity is very important to obtain the semi-insulating conductivity and the improved degradation resistance of BaTiO₃ ceramic capacitors.

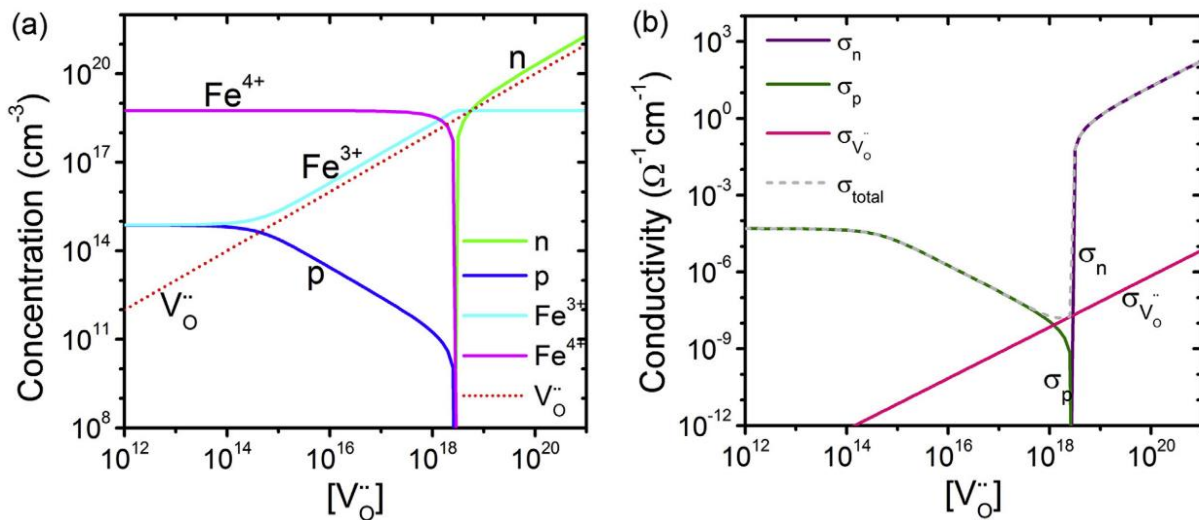


Figure 1.2 Oxygen vacancy concentration-dependent (a) electronic carrier and ionized Fe concentrations and (b) total and partial electrical conductivities of Fe-doped SrTiO₃ at 210 °C. The sample was equilibrated at 900 °C and pO_2 of 10⁻⁵ atm and quenched to room temperature. Reproduced with permission from [19].

Understanding and controlling the degradation behavior is important not only in the ceramic community but also in the semiconductor community. The high-power devices based on β -Ga₂O₃ generally experience a high electric field during their operation at elevating temperature. Even though β -Ga₂O₃ has a high breakdown field, time-dependent degradation may still be of concern. However, there are only a few studies on high-temperature equilibrium defect chemistry,[21–25] and any investigations of time-dependent degradation are not reported yet. Recently, many investigations have been conducted to determine the electrical conduction mechanism of *n*-type Si or Sn doped β -Ga₂O₃. It was concluded that the electrical conductivity of *n*-type β -Ga₂O₃ is highly influenced by the extrinsic factors such as background impurities and doping concentration.[5, 10, 26–29] However, these studies were mostly conducted at a low-temperature range where the role of lattice point defects cannot be fully understood. In addition, a clear understanding of an electrical conduction mechanism in semi-insulating β -Ga₂O₃ has not yet been established.

1.3. Objectives

In both BaTiO₃ ceramics and β -Ga₂O₃ single crystals, it is important to understand the fundamentals of electrical conduction mechanisms and defect chemistry to improve the insulating properties and degradation resistance and the lifetime of devices. Electrical conductivity at room temperature is highly dependent on the sample's processing history, i.e. sintering conditions, dopants types, and their doping level. Thus, the high-temperature equilibrium conductivity as a function of oxygen partial pressure, temperature and doping chemistry should be systematically established. The objectives of this dissertation are to develop a fundamental understanding of electrical conductivity and the role of doping or co-doping in BaTiO₃ and β -Ga₂O₃. Temperature-dependent DC electrical conductivity is measured as a function of time and oxygen partial pressure to realize the equilibrium and partial equilibrium defect chemistry. In addition, the AC impedance characteristics are measured over a wide range of temperatures to understand the frequency-dependent bulk and grain-boundary characteristics. Moreover, time-dependent current densities of doped systems were compared to identify the role of dopants in degradation characteristics.

In Chapter 2, the point defect chemistry of BaTiO₃ is reviewed from a canonical mass-action perspective. In addition, the high-temperature equilibrium electrical conductivities of

BaTiO₃ and β -Ga₂O₃ are reviewed and discussed in terms of defect chemistry. In a few cases, studies on the temperature-dependent AC impedance of BaTiO₃ are reviewed for better understanding of low-temperature partial equilibria in which only a subset of the point defects can kinetically equilibrate with the external atmosphere. Furthermore, literature about the degradation behavior and thermally stimulated depolarization current (TSDC) are reviewed for BaTiO₃, which gives further insight into the defect chemistry and its evolution under an applied electric voltage.

In Chapter 3, the experimental methods for processing BaTiO₃ ceramics and the basic information of the Fe-doped (010) β -Ga₂O₃ are discussed, and the procedures for the DC and AC electrical measurements are explained. Moreover, the mathematical calculations for predicting the defect concentration are included with Matlab code.

In Chapter 4, the electrical conductivity of BaTiO₃ is explored with respect to the type of acceptor dopant between single-valent Mg or multivalent Mn. The *p*-type electrical conductivity of both compositions is discussed in terms of defect chemistry. In addition, the DC and AC electrical characterization reveals that the total electrical conductivity of BaTiO₃ is limited by the bulk conductivity in the high-temperature regime and grain-boundary conductivity in the low-temperature regime. This Chapter sets the stage for the co-doping studies.

In Chapter 5, co-doping strategies are applied to improve the bulk electrical resistance and degradation resistance of BaTiO₃ with co-dopants of either (Mg and Y) or (Mn and Y). Similar to Chapter 5, the various DC and AC electrical characterizations are conducted to explore the co-doping effects on the electrical conductivity. Moreover, the time-dependent degradation behavior is compared to evaluate the relative effectiveness of the two different co-dopants. It is demonstrated that the (Mn and Y) co-doping is much more effective relative to (Mg and Y) co-doping for improving the degradation resistance of BaTiO₃.

In Chapter 6, the origin of semi-insulating electrical properties of Fe-doped (010) β -Ga₂O₃ are investigated using the DC, AC, and Hall techniques. In this study a largely *p*O₂-independent high-temperature electrical conductivity is measured. The behavior is attributed to the low electronic conductivity with low concentration of intrinsic point defects.

In Chapter 7, the overall conclusions of the dissertation and several important future works are discussed.

Chapter 2

Background and Literature Review

2.1. Defect chemistry in BaTiO₃

Understanding point defect chemistry have brought many useful insights to interpret electrical conductivity of oxide materials. The predictions of defect structures have been studied by the theoretical approaches such as canonical defect-modelling[19, 30, 31] and density-functional theory (DFT) calculations.[18, 32–36] Canonical defect-chemistry modelling is based on numerous defect chemical reactions and the laws of mass action, where the system is constrained by the charge neutrality condition. By fitting a defect model to experimental measurements, thermodynamic parameters associated with the various defect reactions can be inferred. Several authors have investigated the possible defect reactions for BaTiO₃[37–46] by measuring the high-temperature equilibrium electrical conductivity. The thermodynamic parameters for corresponding defect reactions were obtained by fitting the observed electrical conductivity using Brower approximations, i.e. simplified defect models that consider only the dominant defects over certain ranges of oxygen activity. The obtained parameters have been used to further construct the low-temperature quenched defect chemistry.[47, 48] In the following, the possible defect reactions in BaTiO₃ are introduced with mass action law and charge neutrality conditions expressed in the Kröger-Vink notation, and the thermodynamic parameters in literature are reviewed.

2.1.1. Electronic equilibrium

The generation of electrons and holes from the electronic equilibrium between valence and conduction band can be written as:

$$n = p \quad (2.1)$$

The equilibrium constant, K_i is:

$$K_i = np = K_i^0 \exp\left(-\frac{\Delta E_g}{k_B T}\right) = N_C N_V \exp\left(-\frac{\Delta E_g^0 - \beta T}{k_B T}\right) \quad (2.2)$$

where n and p are a concentration of electron and hole, respectively. K_i^0 is a pre-exponential factor, ΔE_g is a band gap energy, N_C and N_V are respectively an effective density of state in conduction band and valence bands, ΔE_g^0 is a band gap at 0 K, β is a temperature coefficient of the band gap, k_B is the Boltzmann constant and T is a temperature.

The band gap and the pre-exponential term can be obtained by measuring temperature-dependent electrical conductivity near the n - p transition point in the electrical conductivity versus pO_2 measurements. In the n - p transition point, if the ionic conductivity (σ_{ion}) is constant or negligible, the electron and hole concentration (n and p) have a simple relation with a K_i term as shown in Eq. 2.2. By knowing the ionic conductivity and electron and hole mobilities, the temperature-dependent K_i can be evaluated.

2.1.2. Oxygen exchange reaction

The oxygen exchange reaction in $BaTiO_3$ can be written as a reduction reaction:



The equilibrium constant is:

$$K_{Re} = [V_O^{\cdot\cdot}]n^2P_{O_2}^{1/2} = K_{Re}^0 \exp\left(-\frac{\Delta H_{Re}}{k_B T}\right) \quad (2.4)$$

where K_{Re}^0 is a pre-exponential factor, ΔH_{Re} is an enthalpy of the reduction reaction, i.e. the formation energy of oxygen vacancies. In Eq 2.4, the pre-exponential factor and the formation energy can be evaluated by knowing the concentration of electron and oxygen vacancy as a function of temperature in a very low $p\text{O}_2$ regime with mobility terms.

2.1.3. Full Schottky reaction

By the definition of Schottky reaction, the full Schottky defect reaction in BaTiO_3 entails the formation of Ba and Ti vacancies and anion O vacancy simultaneously:



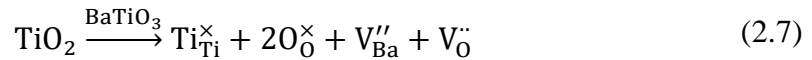
The equilibrium constant can be expressed as:

$$K_S = [V_{\text{Ba}}''] [V_{\text{Ti}}''''] [V_{\text{O}}^{\bullet\bullet}]^3 = K_S^0 \exp\left(-\frac{\Delta H_S}{k_B T}\right) \quad (2.6)$$

where K_S^0 is a pre-exponential factor, ΔH_S is an formation enthalpy of the full Schottky reaction. Nowotny obtained the equilibrium constant of the full Schottky reaction of the undoped and acceptor doped BaTiO_3 compositions by fitting the high-temperature electrical conductivity in the high $p\text{O}_2$ range.[49] Yoon et al. calculated the formation energy of the full Schottky defects in Nb-doped BaTiO_3 ceramics,[50] and used Brower approximations in the intermediated $p\text{O}_2$ range where the extrinsic Nb donors are assumed to be compensated by the full Schottky defects. These values are summarized in Table 2.1.

2.1.4. Partial Schottky reaction

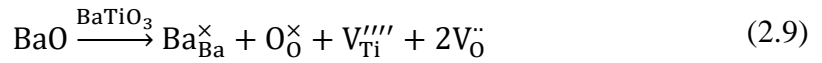
The partial Schottky defect reaction is determined by the cation nonstoichiometry in BaTiO_3 . In Ti-rich BaTiO_3 , since the Ti, Ba and O lattice site ratios must remain 1:1:3, the partial Schottky defect generates Ba and O vacancies as expressed by:



The equilibrium constant for this reaction is:

$$K_{\text{PS,Ti}} = [V_{\text{Ba}}''] [V_{\text{O}}^{\cdot\cdot}] = K_{\text{PS,Ti}}^0 \exp\left(-\frac{\Delta H_{\text{PS,Ti}}}{k_B T}\right) \quad (2.8)$$

where $K_{\text{PS,Ti}}^0$ is a pre-exponential factor, $\Delta H_{\text{PS,Ti}}$ is an enthalpy of the partial Schottky reaction. It is important to note that this partial Schottky reaction occurs within the solubility regime. Once the solubility limit of TiO_2 is exceeded, secondary phase such as BaTi_2O_5 or $\text{Ba}_6\text{Ti}_{17}\text{O}_{40}$ is formed. In the case of Ba-rich BaTiO_3 compositions, the TiO_2 partial Schottky defect is expected:



The equilibrium constant in an ideal solution is:

$$K_{\text{PS,Ba}} = [V_{\text{Ti}}''''][V_{\text{O}}^{\cdot\cdot}]^2 = K_{\text{PS,Ba}}^0 \exp\left(-\frac{\Delta H_{\text{PS,Ba}}}{k_B T}\right) \quad (2.10)$$

where $K_{\text{PS,Ba}}^0$ is a pre-exponential factor, and $\Delta H_{\text{PS,Ba}}$ is an enthalpy of the partial Schottky reaction. Again, the reaction occurs in the solubility regime of BaO into BaTiO_3 , and if the excess of BaO exceeds the solubility, then secondary phases such as Ba_2TiO_4 will form.

The formation enthalpy in the full Schottky and partial Schottky reactions have been rarely investigated compared to other point defects. Lee et al. utilized theoretical and experimental approaches to obtain the formation energy of the full Schottky and partial Schottky defects in the nonstoichiometric high purity undoped BaTiO_3 ceramics.[37] This approach was based on the observation of phase solubility limit between the pure BaTiO_3 and the secondary phases either BaTi_2O_5 and $\text{Ba}_6\text{Ti}_{17}\text{O}_{40}$ on Ti-rich side or Ba_2TiO_4 and $\text{Ba}_{1.054}\text{Ti}_{0.946}\text{O}_{2.946}$ on Ba-rich side.

The various pre-exponential factors and enthalpies of defect reaction are summarized in Table 2.1. Literature reviews reveal that an equilibrium constant for corresponding specific defect reaction can be different even in the same doping system. This is probably due to the different background impurity concentration and the assumptions for the defect model and the mobility terms that the authors made.

Table 2.1 Pre-exponential factor and enthalpy of defect reactions. Bolded values were used for calculations in sections 2.1.5 and 5.4.

Defect reaction	Experimental condition	Pre-exponential factor (K_0)	Enthalpy (eV)	Ref.
Electronic equilibrium	Undoped	$1.06 \times 10^{45} \text{ (cm}^{-6}\text{)}$	3.15 ± 0.39	[38–40]
		$1.69 \times 10^{45} \text{ (cm}^{-6}\text{)}$	2.93 ± 0.23	[41]
		$8.55 \times 10^{44} \text{ (cm}^{-6}\text{)}$	2.91	[49]
	Al-doped	$2.28 \times 10^{42} \text{ (cm}^{-6}\text{)}$	2.15 ± 0.07	[42]
	Mn-doped	$10^{47.1} \text{ (cm}^{-6}\text{)}$	3.41	[51]
		$6.8 \times 10^{44} \text{ (cm}^{-6}\text{)}$	2.90	[43]
Nb-doped	$10^{45} \text{ (cm}^{-6}\text{)}$	2.9	[44]	
Reduction reaction	Undoped	$7.15 \times 10^{73} \text{ (cm}^{-9} \cdot \text{atm}^{1/2}\text{)}$	5.80 ± 0.15	[41]
		$7.09 \times 10^{70} \text{ (cm}^{-9} \cdot \text{atm}^{1/2}\text{)}$	5.89	[51]
		$1.06 \times 10^{71} \text{ (cm}^{-9} \cdot \text{atm}^{1/2}\text{)}$	5.69	[49]
		$3.06 \times 10^{77} \text{ (cm}^{-9} \cdot \text{atm}^{1/2}\text{)}$	7.30	[45]
		$2.56 \times 10^{71} \text{ (cm}^{-9} \cdot \text{atm}^{1/2}\text{)}$	6.10	[44]
	Acceptor-doped	$9.43 \times 10^{72} \text{ (cm}^{-9} \cdot \text{atm}^{1/2}\text{)}$	5.99	[46]
Al-doped	$2.40 \times 10^{74} \text{ (cm}^{-9} \cdot \text{atm}^{1/2}\text{)}$	5.88 ± 0.17	[42]	
Full Schottky reaction	Undoped and acceptor-doped	$3.4 \times 10^{105} \text{ (cm}^{-15}\text{)}$	2.795	[49]
	Nb-doped	$10^{116} \text{ (cm}^{-15}\text{)}$	10.5	[50]
	Undoped (Ti-rich)	-	3.33 ± 0.2	[37]
	Undoped (Ba-rich)	-	3.48 ± 0.2	
Partial Schottky reaction	Undoped (Ti-rich)	-	2.32 ± 0.1	
	Undoped (Ba-rich)	-	2.89 ± 0.1	
Ionization of Al ($\text{Al}_{\text{Ti}}^{\times} \rightleftharpoons \text{Al}'_{\text{Ti}} + \text{h}'$)	Al-doped	$1.9 \times 10^{23} \text{ (cm}^{-3}\text{)}$	1.04	[40]
Ionization of Mn ($\text{Mn}_{\text{Ti}}^{\times} \rightleftharpoons \text{Mn}'_{\text{Ti}} + \text{h}'$)	Mn-doped	$3.19 \times 10^{22} \text{ (cm}^{-3}\text{)}$	1.69	[43]
Ionization of Mn ($\text{Mn}'_{\text{Ti}} \rightleftharpoons \text{Mn}_{\text{Ti}}^{\times} + \text{e}'$)		$3.2 \times 10^{22} \text{ (cm}^{-3}\text{)}$	1.72	[46]
Ionization of Mn ($\text{Mn}''_{\text{Ti}} \rightleftharpoons \text{Mn}'_{\text{Ti}} + \text{e}'$)		$0.8 \times 10^{22} \text{ (cm}^{-3}\text{)}$	1.12	

2.1.5. Charge neutrality condition

The electroneutrality condition for the system, considering all point and electronic defects, is expressed as a charge neutrality equation:

$$\sum_{i=1} [\text{Positive}]_i = \sum_{j=1} [\text{Negative}]_j \quad (2.11)$$

Assuming no background impurities, the charge neutrality equation for BaTiO₃:

$$p + [V_{\text{O}}^{\bullet\bullet}] + \sum_{k=1} [D^x]_k = n + [V_{\text{Ti}}^{\prime\prime\prime}] + [V_{\text{Ba}}^{\prime\prime}] + \sum_{l=1} [A^y]_l \quad (2.12)$$

where $[D^x]$ and $[A^y]$ are the donor and acceptor concentrations, respectively and the x and y indicate the possible charge states. From Eq. 7.2, 7.4, and 7.8, the charge neutrality equation can be re-written as:

$$\frac{K_i}{n} + \frac{K_{\text{Re}}}{n^2 p_{\text{O}_2}^{1/2}} + \sum_{k=1} [D^x]_k = n + 6 \left(\frac{K_S}{K_{\text{Re}}^3} \right)^{1/2} n^3 p_{\text{O}_2}^{3/4} + \sum_{l=1} [A^y]_l \quad (2.13)$$

By knowing the equilibrium constants and the doping level of acceptors and/or donors, the defect concentrations can be predicted as a function of oxygen partial pressure at various temperatures. Using the equilibrium constants of the reduction reaction, electronic equilibrium, and full Schottky reaction obtained by Nowotny,[49] the full and partial equilibrium defect structures are predicted in undoped BaTiO₃ compositions and presented in Fig. 2.1. The details of mathematical calculation can be found in Chapter 3.5. A few calculations were carried out to reproduce the prior calculation by Nowotny[49] using the same temperature and p_{O_2} condition, and they show a good agreement. The full equilibrium defect concentrations as a function of p_{O_2} are explored by solving Eq. 2.13 at the equilibrium temperature ($T_E = 1150$ °C), below which the cation vacancies are assumed to be immobile.[52] Then, the low-temperature ($T_Q = 1000$ °C) quenched defect structures are calculated through the Eq. 2.13 under the assumptions that the concentration of cation vacancy is fixed from the high-temperature equilibration ($T_E = 1150$ °C and $p_{\text{O}_2} = 0.21$ atm) but that of the

electronic carriers (n and p) and oxygen vacancy are allowed to be fully equilibrated at T_Q over entire range of pO_2 .

Figure 2.1 shows the equilibrium and quenched defect concentrations of undoped $BaTiO_3$. In Figure 2.1(a), the equilibrium defect concentration at 1150 °C shows mainly three different pO_2 regimes which are the highly reduced, intermediate, and relatively high pO_2 regime. In the highly reduced pO_2 range ($pO_2 < 10^{-15}$ atm), the reduction reaction is the predominant defect reaction with electrons as a major electrically conducting species. In the intermediate pO_2 range (10^{-15} atm $< pO_2 < 10^2$ atm), the oxygen vacancies are ionically compensated by the cation vacancies. As increasing pO_2 , the electron concentration decreases, while the hole concentration starts to increase. The n - p transition position is located at around 10^{-6} atm of pO_2 . In oxidizing pO_2 range ($pO_2 > 10^2$ atm), the oxygen vacancy concentration starts to decrease, and the holes becomes the major charge carrier compensating the cation vacancies.

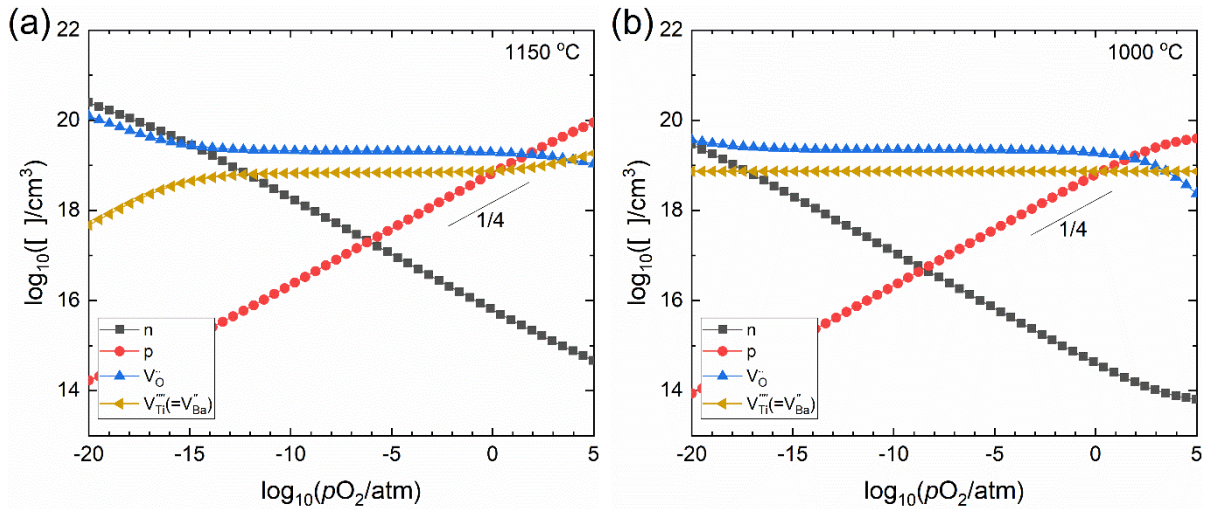


Figure 2.1 (a) Full equilibrium defect structure at 1150 °C and (b) partial equilibrium defect structure at 1000 °C with the fixed cation vacancies equilibrated from the high-temperature condition (1150 °C and $pO_2 = 0.21$ atm) in undoped $BaTiO_3$.

Figure 2.1(b) shows the partial equilibrium defect structure of undoped $BaTiO_3$ in which the cation concentration is frozen-in from the high-temperature equilibrium condition (1150 °C and $pO_2 = 0.21$ atm) to lower temperatures over the entire range of pO_2 . At 1000 °C, the ionic compensation is observed over a wide range of oxygen partial pressure. When the pO_2 is higher than 10^{-8} atm, the hole concentration is higher than electron concentration, and therefore, a p -type

electrical conductivity is expected in these pO_2 range, which is agreed to the electrical conductivity measured by Nowotny.[53] The electrical conductivity of undoped $BaTiO_3$ ceramics and single crystal (open triangle) [53] at 1000 °C is summarized in Figure 2.2. It is worth noting that the magnitude of electrical conductivity and the $n-p$ transition point vary particularly in high pO_2 range. This implies that purity and history of sample processing are important factors determining the electrical conductivity in undoped $BaTiO_3$.

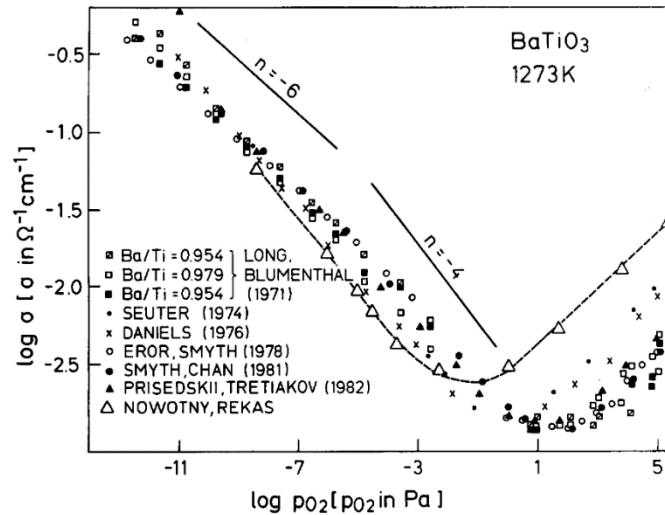


Figure 2.2 Electrical conductivity versus pO_2 of undoped $BaTiO_3$ ceramics and single crystals at 1000 °C.

The defect concentrations were further explored in single-valent acceptor-doped $BaTiO_3$. It was assumed that acceptors (doping level is $10^{20} /\text{cm}^3$) exclusively occupy the Ti-site and they are doubly ionized, i.e. A''_{Ti} . In addition, the A/B was kept to 1:1, meaning that the full Schottky reactions was included during calculation. Similar to undoped $BaTiO_3$, the full and partial equilibrium defect concentrations are shown in Figure 2.3. Although the overall full equilibrium defect equilibria in Figure 2.3(a) is similar to that of undoped $BaTiO_3$, two clear differences are seen. One is that the oxygen vacancy concentration is mainly compensated by A''_{Ti} over the entire ranger of pO_2 . The other is that there is a decrease in the concentration of Schottky defects. Because the acceptors, which are negatively charged species, are intentionally doped in $BaTiO_3$, the system prefers to have less amount of negatively charged cation vacancies.

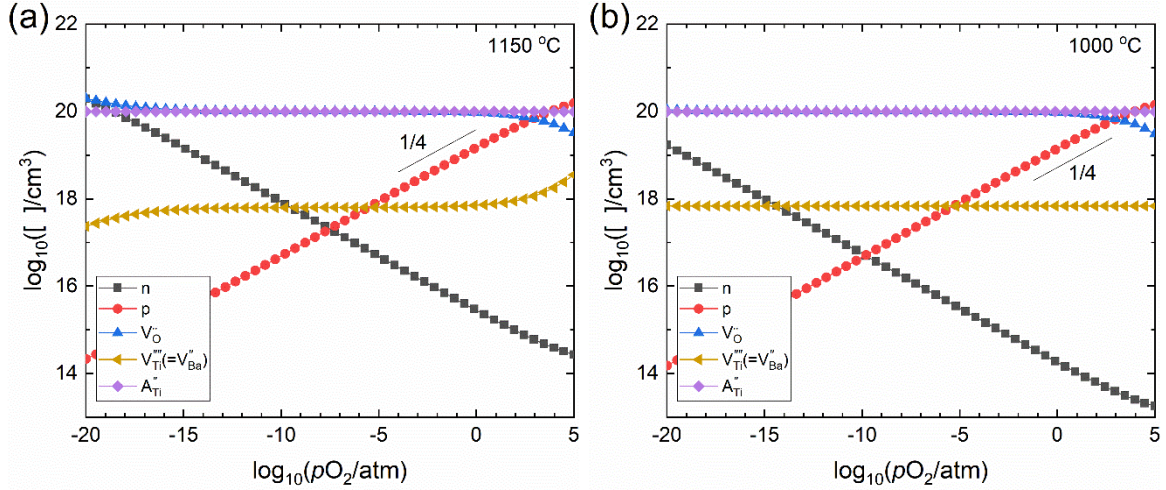


Figure 2.3 (a) Equilibrium defect structure at 1150 °C and (b) partial equilibrium defect structure at 1000 °C with the fixed cation vacancies (equilibrated at $T_E = 1150$ °C and $p\text{O}_2 = 0.21$ atm) in single-valent acceptor-doped BaTiO₃.

The quenched defect concentration at 1000 °C is shown in Figure 2.2(b). Again, the p -type electrical conductivity is expected in high $p\text{O}_2$ range where the hole concentration is predominant. In the entire range of $p\text{O}_2$, the cation vacancy concentration is fixed by the high-temperature equilibrium concentration at T_E of 1150 °C and $p\text{O}_2$ of 0.21 atm. In the case of oxygen vacancy concentration, it is extrinsically fixed by acceptors whose level is 10²⁰ /cm³ and is higher than that in undoped BaTiO₃. Thus, it is expected that acceptor-doped BaTiO₃ show the ionic conductivity at the intermediate $p\text{O}_2$ range where the low electronic conductivity is expected due to the low concentration of electrons and holes. This is more clearly seen as decreasing temperature where electronic conductivity is reduced, while the ionic conductivity is fixed due to the constant number of oxygen vacancies.[54]

It is apparent that the defect chemistry changes significantly by doping and equilibrium and the oxygen partial equilibrium conditions. In the following sections, the experimental conductivity results are reviewed in the various acceptor-doped and co-doped BaTiO₃ compositions. In general, the high-temperature electrical conductivity can be well understood by the canonical defect chemistry in simple acceptor-doped BaTiO₃. In some cases, the developed canonical defect models can predict only a portion of the comprehensive behavior of defect concentrations.

2.2. Electrical conductivity in BaTiO₃

2.2.1. Acceptor-doped BaTiO₃

The high-temperature equilibrium electrical conductivity of Mg-doped BaTiO₃ was explored by Jeong and Han.[55] Mg acts an acceptor when it sits on the Ti site, i.e. Ba(Ti_{1-x}Mg_x)O₃, as it has a net negative charge, Mg_{Ti}''. The electrical conductivity as a function of oxygen partial pressure at 1000 °C is seen in Figure 2.4, and all Mg-doped samples show the *p*-type behavior of electrical conductivity in the high *p*O₂ range (> 10⁻⁴ atm). As increasing Mg concentration, the *n*-*p* transition position shifts leftward and the magnitude of conductivity increased. In addition, the conductivity becomes more *p*O₂-invariant at the intermediate *p*O₂ range which is explained as the oxygen vacancies becoming the dominant charge carrier.

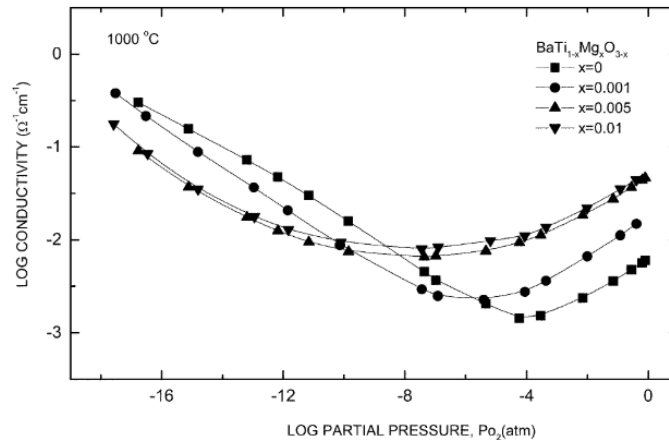


Figure 2.4 Equilibrium electrical conductivity of undoped BaTiO₃ and Ba(Ti_{1-x}Mg_x)O_{3-x} (*x* = 0, 0.001, 0.005, 0.01) at 1000 °C. Reproduced with permission from [55].

The high-temperature electrical conductivity of Al-doped BaTiO₃ was studied by Chan et al.[40] The ceramic specimens having a fixed 0.995 of Ba/(Ti+Al) were doped with 155 ppm (0.0155 mol%), 484 ppm (0.0484 mol%), and 1506 ppm (0.1506 mol%) of Al. In sample preparation, a small amount of TiO₂ was intentionally added to assist the sintering process (1420 °C for 2.5 h in air), and it was found that the presence of a small amount of Ti-rich secondary phase was detected in the triple-point of the grains,[56] which did not affect the electrical conductivity.[51]

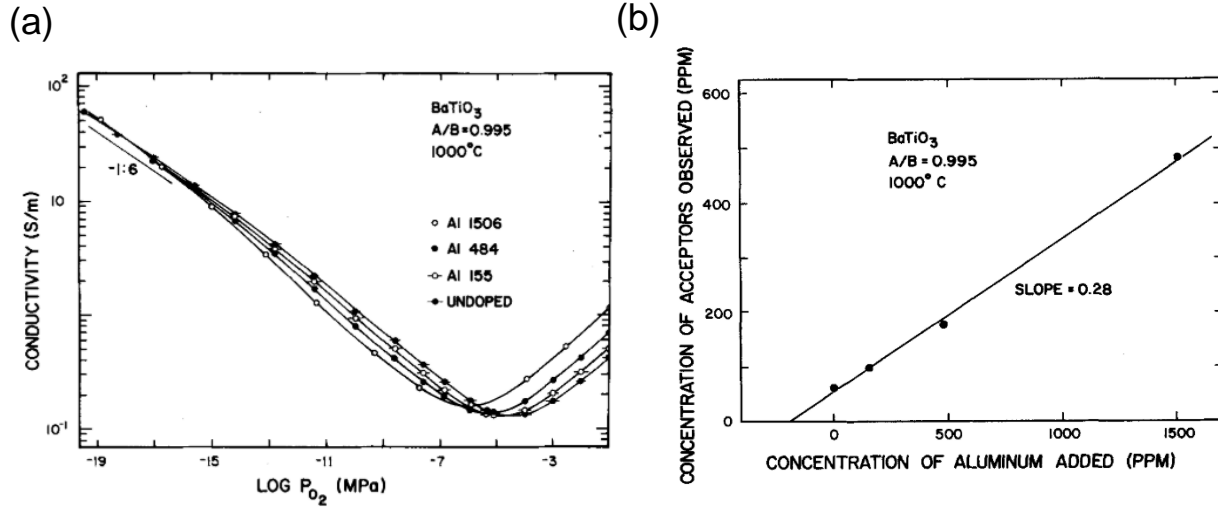


Figure 2.5 (a) Equilibrium electrical conductivity of undoped and Al-doped BaTiO₃ at 1000°C. (b) Apparent net acceptor concentration derived from conductivity data, compared with the amount of added Al. Reproduced with permission from [40].

In Figure 2.5(a), the magnitude of electrical conductivity minima increased slightly and shifted to lower pO_2 , which is consistent to the prior studies in Mg-doped BaTiO₃. [55] However, a pO_2 -independent electrical conductivity near the n - p transition region was not observed at this temperature, meaning that the contribution of ionic conductivity is small. In the very low pO_2 range ($< 10^{-17}$ MPa) where the reduction reaction is predominant, the pO_2 -dependent electrical conductivity is invariant with respect to the Al concentration, indicating that the intrinsic reduction reaction is not affected by impurity concentration. In Figure 2.5(b), regardless of the doping level, the back-calculated concentration of Al acceptor from the canonical defect models was only ~ 30%. The origin of the phenomenon was not clearly understood, however, the authors suggested the possible explanations, (1) inhomogeneous distribution of acceptors and segregation at grain boundary, (2) formation of defect complexes between oxygen vacancy and acceptor, (3) formation of a new structure similar to perovskite which consumes point defects, and (4) the incorporation of Al into BaTiO₃ as an interstitial or Ba substitution, compensating the acceptors.

Kim et al. compared the DC electrical conductivity of undoped and 1 mol% Mn-doped BaTiO₃ ceramics from 900 °C to 1200 °C in a pO_2 range of 1 atm – 10⁻¹⁵ atm.[43] The high-temperature electrical conductivity shows clear difference as a function of pO_2 as shown in Figure 2.6. The isothermal electrical conductivity varies from $\sigma \propto pO_2^{-1/6}$ to $\sigma \propto pO_2^{-1/4}$ to $\sigma \propto pO_2^{+1/4}$

in undoped BaTiO₃, while that of Mn-doped BaTiO₃ changed from $\sigma \propto pO_2^{-1/4}$ to $\sigma \propto pO_2^{-1/6}$ to $\sigma \propto pO_2^{+1/6}$ as increasing pO_2 , which is agreed to the study by Osawa et al.[57] The origin the pO_2 dependence is attributed to the ionization of Mn, i.e. the charge state of Mn on Ti site can be varied depending on pO_2 . This is the clear difference between single-valent acceptor such as Mg, Al, Ca and multivalent Mn.

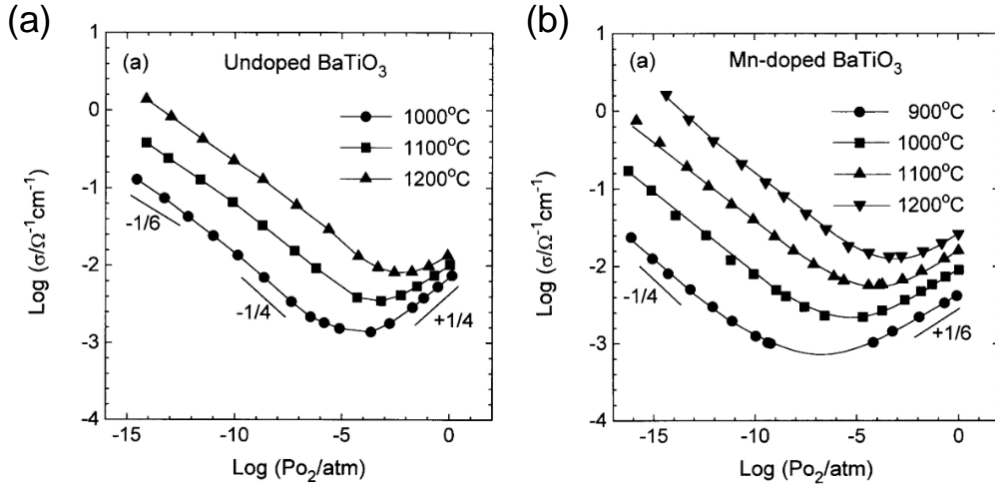


Figure 2.6 Electrical conductivity of (a) undoped BaTiO₃ and (b) Mn-doped BaTiO₃ vs. oxygen partial pressure at different temperatures. Reproduced with permission from [43].

High-temperature electrical conductivity of Ca-doped BaTiO₃ was analyzed over the oxygen partial pressure (pO_2) of 10^{-18} atm ~ 1 atm at a temperature range of 800 °C ~ 1000 °C by Han et al.[54] In this work, three different BaTiO₃ samples were fabricated: one was (Ba_{1-x}Ca_x)TiO₃, i.e. BaO was replaced by CaO, another is (BaTiO₃ + x CaO), i.e. CaO was added to stoichiometric BaTiO₃, and the other was Ba(Ti_{1-x}Ca_x)O_{3-x}, i.e. TiO₂ was replaced by CaO with $x = 0.005$ and 0.002 . As shown in Figure 2.7(a), there was a significant shift of the n - p transition point to lower pO_2 in (BaTiO₃ + x CaO) with the higher Ca concentration. In addition, the increased and flattened electrical conductivities were observed. These results were attributed to the incorporation of Ca into the Ti-site, leading to the increase in oxygen vacancies and the pO_2 -independent ionic conductivity. However, when Ca occupied on the Ba-site, the electrical conductivity was identical regardless of the Ca concentration. In Figure 2.7(b), the electrical conductivity of BaTiO₃ + 0.02CaO and Ba(Ti_{0.98}Ca_{0.02})O_{2.98} is also compared at 800 °C and 1000

°C. At the lower temperature 800 °C, a wider pO_2 -independence was shown in both samples due to the high ionic conductivity originated from the temperature-independent oxygen vacancy concentration introduced by Ca doping. The magnitude of the electrical conductivity was slightly higher in $Ba(Ti_{0.98}Ca_{0.02})O_{2.98}$, and this is attributed to the higher concentration of oxygen vacancies.

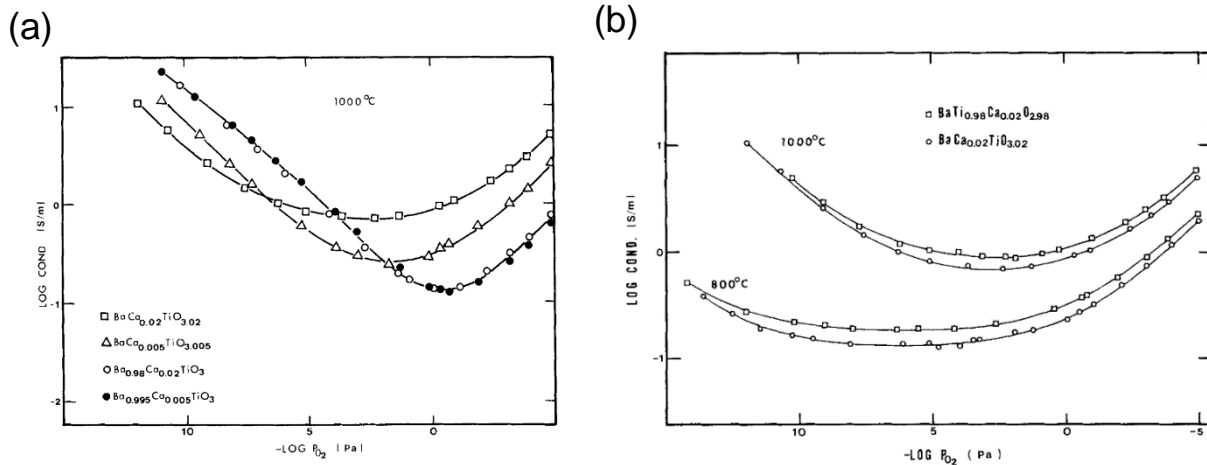


Figure 2.7 (a) Equilibrium electrical conductivity of $(Ba_{1-x}Ca_x)TiO_3$ and $(BaTiO_3 + xCaO)$ with $x = 0.5$ mol% and 2 mol% at 1000 °C. (b) Equilibrium electrical conductivities at 800 °C and 1000 °C of $(BaTiO_3 + xCaO)$ and $Ba(Ti_{1-x}Ca_x)O_3$ with $x = 2$ mol %. Reproduced with permission from [54].

Temperature-dependent DC and AC electrical conductivities of single-valent Mg or multivalent Mn-doped multilayer $BaTiO_3$ has been systemically investigated by Yoon et al.[48, 58–61] The authors investigated the bulk and grain boundary conductivities as a function of doping concentration, temperature, grain size, and sintering and re-oxidation annealing conditions. The room temperature electrical conductivity was explored as a function of Mg concentration from 0 to 0.5 mol% with varying pO_2 during sintering to find an optimized Mg concentration for a high resistance and a good degradation resistance.[60] The study revealed that the electrical conductivity of undoped $BaTiO_3$ sintered at a low pO_2 showed a high electrical conductivity, $\sim 50 \Omega \cdot cm$ at room temperature as shown in Figure 2.8. With increasing the acceptor concentration, the room temperature electrical conductivity increased rapidly and showed $\sim 10^{12} \Omega \cdot cm$ with 0.1 mol% Mg doping. It was also observed that the post re-oxidation process in 10^{-6} atm improved the resistance of the sample as indicated as the gold symbol in Figure 2.8. The calculated quenched

defect structure explains the observed high resistance of the specimens at room temperature, showing that while the concentration of electron and cation vacancies decrease, oxygen vacancies increase with increasing the acceptor concentration.

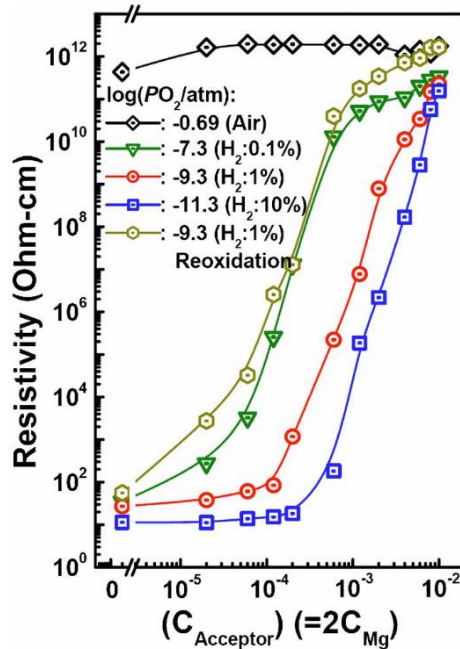


Figure 2.8 Mg concentration-dependent room temperature electrical resistivities of Mg-doped BaTiO₃ sintered in different oxygen partial pressures. Reproduced with permission from [60].

The authors obtained the bulk and grain boundary electrical conductivities as a function of Mg concentration by analyzing the AC impedance responses with the blocking Pt electrodes.[61] By analyzing Curie-Weiss law, it was concluded the high- and low-frequency arcs are originated from the bulk and grain-boundary responses, respectively. In addition, the major findings in the AC measurements are that (1) while the bulk electrical conductivity decreases with increasing Mg concentration, the grain boundary conductivity is almost independent on Mg concentration, (2) the grain boundary conductivity is lower than the bulk conductivity regardless of Mg doping at a given temperature in the coarse BaTiO₃ samples which were sintered in air, and (3) the low-frequency (~ 1mHz) Warburg impedance at 480 °C can be seen more clearly and the ionic transference number increased with increasing Mg concentration in BaTiO₃.

The effects of grain size on the bulk and grain boundary conductivities as a function of temperature,[59] showing that (1) the bulk conductivity increases as increasing Mg doping level

regardless of grain size, (2) the bulk conductivity is higher in the coarse grain samples, (3) the grain boundary conductivity is doping level-invariant in the coarse grain specimens, however, the conductivity shows the positive dependence on the Mg concentration in the fine grain specimens, and (4) the Warburg impedance is observed in both fine and coarse grain samples, and the impedance is higher in the coarse grain samples, meaning the portion of ionic conductivity is higher than that in fine grain specimens.

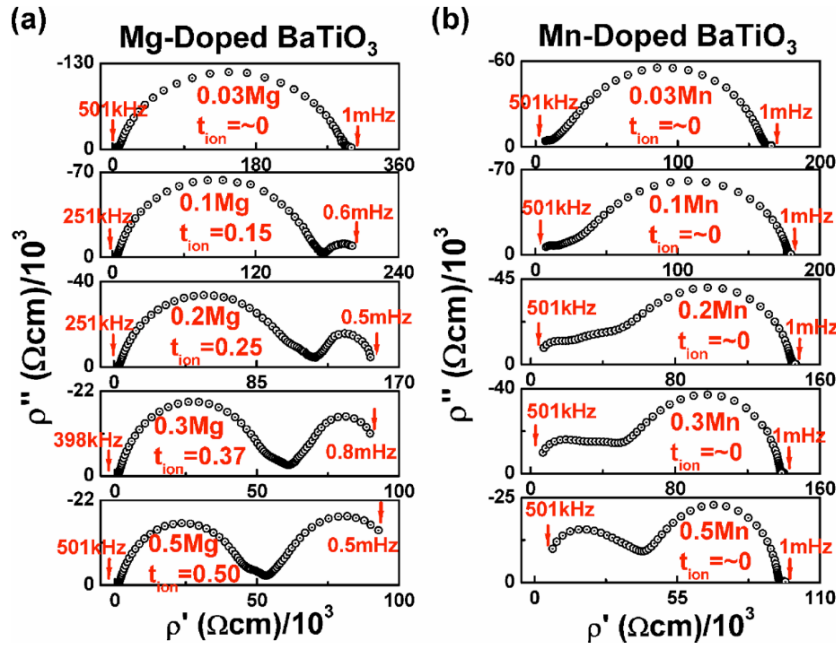


Figure 2.9 Doping concentration-dependent Cole-Cole plots of (a) Mg or (b) Mn-doped BaTiO₃ at 480 °C. Reproduced with permission from [48].

The AC impedance of Mg or Mn-doped BaTiO₃ ceramics was studied as a function of doping level of the acceptors.[48] In this work, the most different results in the AC impedance between Mg and Mn doping is that Mn-doped BaTiO₃ shows (1) the lower bulk conductivity with the higher Mn concentration and (2) no Warburg impedance at low-frequency in contrast to Mg-doped BaTiO₃ as shown in Figure 2.9. The negligible ionic transference number is attributed to the low ionic conductivity with the significantly low concentration of oxygen vacancy compared to Mg-doped BaTiO₃ with the same doping level. The predicted equilibrium and quenched defect structure as a function of pO_2 at high- and low-temperatures showed that the higher concentration of oxygen vacancies was obtained in Mg-doped BaTiO₃, explains the high ionic conductivity in Mg-doped BaTiO₃.

2.2.2. Co-doped BaTiO₃

Chan and Smyth investigated the equilibrium electrical conductivity versus pO_2 of Nb and Al co-doped BaTiO₃ ceramics.[62] As shown in Figure 2.10, the electrical conductivity becomes pO_2 independent and the overall magnitude increases with donor doping (solid triangle \rightarrow solid circle \rightarrow open circle), which is due to the increment of pO_2 -independent electron concentration compensating donors (Nb). Then, the donor-doped BaTiO₃ was back doped by acceptor, Al (open rectangular \rightarrow open triangle \rightarrow solid rectangular). In this work, two interesting phenomena were observed. One was that although the co-doped sample containing 632 ppm Al and 467 ppm Nb (open triangle) had more acceptors than donors, the electrical conductivity was close to the n -type conductivity. Similarly, the other was that the sample co-doped by 314 ppm Al and 467 ppm Nb (open triangle) exhibited a more donor-doped behavior than 151 Nb singly doped BaTiO₃ (solid circle). This is interesting because the net donor concentration of both samples was very close.

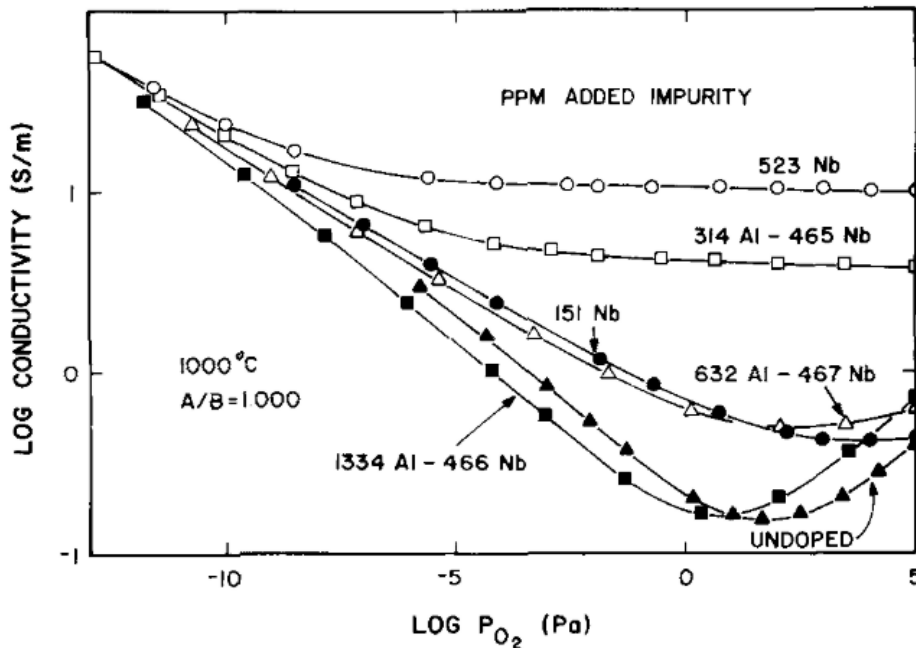


Figure 2.10 Equilibrium electrical conductivity at 1000 °C of BaTiO₃. Reproduced with permission from [62].

The high-temperature electrical conductivity of Mn and Y co-doped BaTiO₃ ceramics which is the most important compositions in this dissertation, was investigated by Lee et al.[63] and Yeoh

et al.[64] In Figure 2.11, the high-temperature electrical conductivity of co-doped BaTiO₃ was pO_2 -independent and lower than that of undoped BaTiO₃ in the high pO_2 range, when the doping ratio of Y and Mn ($[Y]/[Mn]$) is between 0.5 and 1.8. As the ratio was over 1.8, the magnitude of electrical conductivity increased and showed more n -type characteristics. The Fermi level as a function of pO_2 was calculated by linking the electron concentration obtained from the canonical defect chemistry to Boltzmann's statistics. It was revealed that the Fermi level is pinned over a wide range of pO_2 due to the mechanism of donor-acceptor mutual compensation, when Y/Mn is in between 1 and 2. However, their prediction reveals that the n -type electrical conductivity is expected at the high pO_2 range with $2.0 > [Y_{Ba}]/[Mn_{Ti}]_T > 1$. This does not agree to the experimental results.

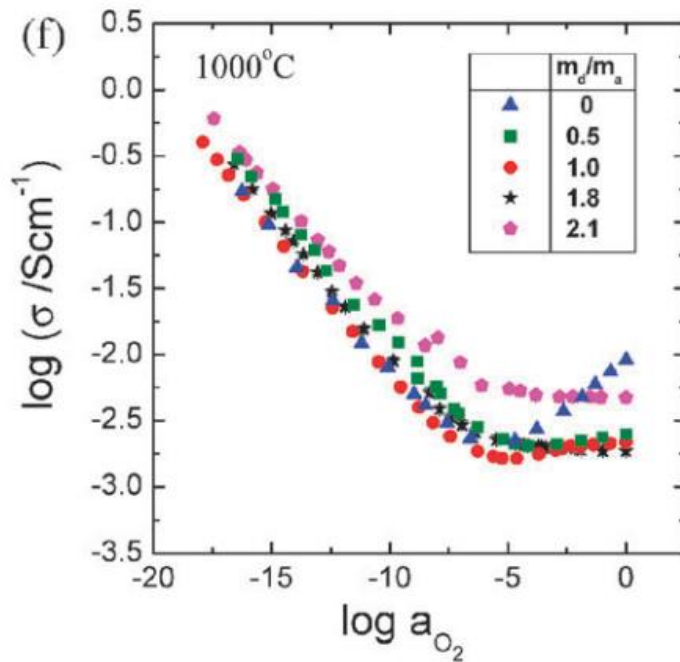


Figure 2.11 Electrical conductivity versus oxygen activity of BaTiO₃ co-doped by Mn and Y with different donor-to-acceptor ratios $m_d/m_a = 0.0$ (a), 0.5 (b), 1.0 (c), 1.8 (d), and 2.1 (e) at 1000 °C. Reproduced with permission from [64].

The high-temperature electrical conductivity of BaTiO₃ ceramics co-doped by either (Ho and Mn) or (Dy and Mn) were investigated by Han et al.[65, 66] When Ho and Mn are respectively doped on the A-site and B-site, the magnitude of electrical conductivity was lower than that of

singly doped BaTiO₃ at 1200 °C in Figure 2.12(a). In addition, the pO_2 -independent conductivity was observed in the high pO_2 range. The reduced pO_2 -independent electrical conductivity in the high pO_2 range is attributed to the reduced oxygen vacancy concentration with donor doping.

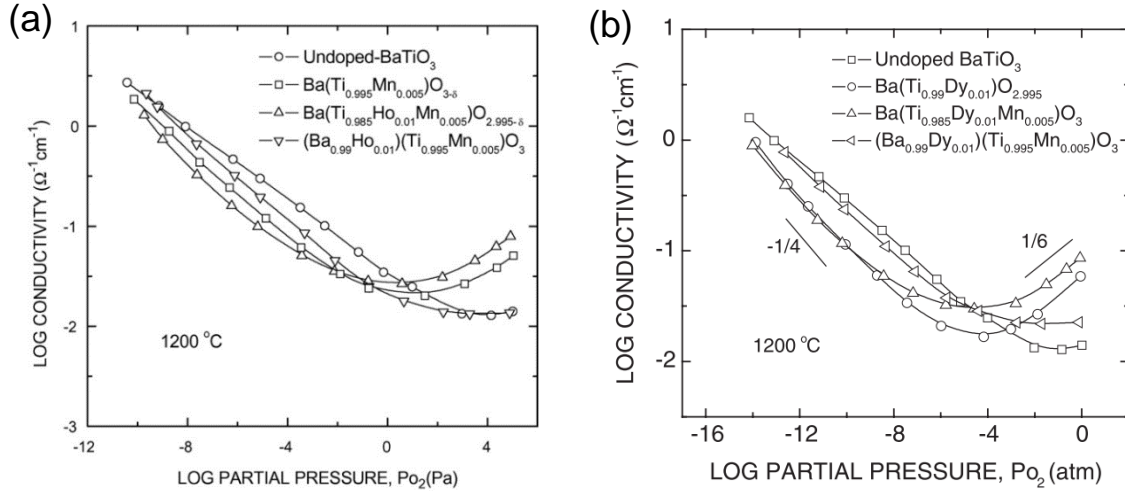


Figure 2.12 (a) Equilibrium electrical conductivities of BaTiO₃ co-doped with (a) Ho and Mn (b) Dy and Mn at 1200 °C. Reproduced with permission from [65,66].

The room temperature resistivities of BaTiO₃ co-doped by Mg and rare earth elements (La, Sm, Dy, Ho, Er, or Yb) were investigated by Kishi et al.[14] Figure 2.13 shows the room temperature electrical resistivity of (Ba_{1-2x}R_{2x})(Ti_{1-x}Mg_x)O₃ with $x = 0$ to 0.15 (R: La, Sm, Dy, Ho, Er, or Yb) ceramics. In the (Dy + Mg) and (Ho + Mg) co-doped samples, the abrupt increase in resistivity was observed with the increase of doping level. This abrupt change in the resistivity corresponds to the variation in the lattice parameters,[14] and is attributed to the amphoteric behavior of Dy and Ho, meaning that Dy and Ho can occupy both the A-site and B-site depending on the doping concentration.

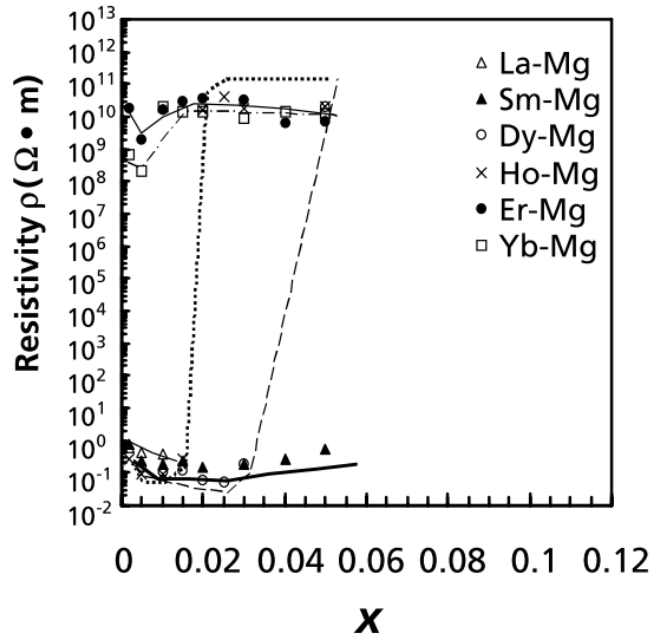


Figure 2.13 Room temperature resistivities of $(\text{Ba}_{1-2x}\text{R}_{2x})(\text{Ti}_{1-x}\text{Mg}_x)\text{O}_3$ sintered at 1380 °C in a reducing atmosphere as a function of x ($\text{R} = \text{La}, \text{Sm}, \text{Dy}, \text{Ho}, \text{Er}$ or Yb). Reproduced with permission from [14].

2.3. Doping Effects on Degradation Behavior in BaTiO_3

The degradation characteristics of Mg and Mn singly-doped multilayer BaTiO_3 specimens were studied by Yoon et al. The concentration of dopant was varied from 0 to 0.5 mol%, and the samples were made via MLCC process. In the study, Mg-doped specimens showed more severe resistance degradation and breakdown as increasing Mg concentration. This was attributed to the increased bulk grain conductivity and the portion of ionic conductivity with increasing Mg concentration. Compared to Mg-doping, Mn-doped BaTiO_3 exhibited better degradation behavior as Mn concentration increased.

The degradation behavior of Mn and Dy co-doped BaTiO_3 specimens was investigated by Yoon et al. The compositions were (1) 0.4 mol% Mn and 0.3 mol% Dy co-doped and (2) 0.4 mol% Mn and 0.9 mol% Dy co-doped BaTiO_3 . The time-dependent degradation characteristics of Dy and Mn co-doped BaTiO_3 MLCC were measured at 150 °C under the DC field up to 0.6 MV/cm ~ 0.8 MV/cm. It was revealed that the time-dependent degradation behavior was more stable in

the higher Dy concentration. In addition, the breakdown field was increased in the higher doping level of Dy. Similarly, the degradation characteristics were investigated in Mn and V co-doped BaTiO₃ by the same group. Three different BaTiO₃ MLCCs co-doped by (1) 0.2 mol% Mn and 0.1 mol% V, (2) 0.2 mol% Mn and 0.3 mol% V, and (3) 0.4 mol% Mn and 0.3 mol% V. The time-dependent resistance under various DC field showed that the magnitude of resistance was higher in the lower Mn and V compositions, such that (1) and (2) at the low DC fields. However, the time stability of resistance was better in the higher Mn and V composition. Moreover, the higher breakdown field was improved by the increase of Mn or V doping concentration.

Kishi et al. compared the lifetime of various X7R and Y5V MLCCs compositions by measuring the highly accelerated life test (HALT) under 0.35 MV/cm and 0.7 MV/cm DC electric field at 165 °C.[14] The X7R and Y5V MLCCs were doped by 1 at. % of La, Nd, Sm, Gd, Dy, Ho, or Er. Both X7R and Y5V MLCCs exhibited the improved lifetime, when they are doped by the rare earth amphoteric oxides such as Dy₂O₃, Ho₂O₃, Er₂O₃. Particularly, they are more effective when the thickness of dielectric layer was reduced from 10 μm to 5 μm.

Kaneda et al. studied the vanadium (V) effects on the lifetime of MLCCs.[67] The concentration of V varied from 0 to 0.15 mol% in the samples contain 0.5 mol% MgO, 0.1 mol% MnO, 0.75 mol% Ho₂O₃, and 1.5 mol% SiO₂. Sintering was carried out at 1280 °C for 2 h in 10⁻¹⁰ atm followed the re-oxidation process at 900 °C in 10⁻⁵ atm. The HALT experiments were conducted at 150 °C under the 0.2 MV/cm. The mean time to failure (MTTF) was improved by the addition of V up to 0.1 mol%. With further increased V concentration, the MTTF was slightly reduced. It was revealed that the AC impedance of dielectric-electrode interface, grain boundary, and grain, and found that the resistances of all components were deteriorated with increasing V concentration. Particularly, the interface resistance was significantly reduced. The decrease in the total resistance of specimens was attributed to the increase in the electron concentration by donor doping and the significant decrease in the interface resistance. The density functional theory (DFT) calculations and the thermally stimulated depolarization current (TSDC) analysis showed that the formation of oxygen vacancy was restricted by adding V in BaTiO₃ and thus the improved reliability of MLCCs was attributed to the decrease in concentration of oxygen vacancy.

Natsui et al. investigated the V effects on the time-dependent resistance in BaTiO₃ MLCCs.[68] The specimens were doped by 2 mol% MnO, 0.2 mol% Mn₃O₄, 1 mol% Y₂O₃, 0.5mol % SiO₂, and 0.06 mol%, 0.2 mol% or 0.3 mol% V₂O₅. The specimens were made via the

MLCC process with sintering at 1200 °C for 2 h in the reducing pO_2 of 10^{-12} atm followed by the re-oxidation at 1100 °C in a pO_2 of 10^{-6} atm. The HALT measurements were carried out at 200 °C under 0.35 MV/cm DC field, and the AC impedance was analyzed during HALT. The authors basically used the equivalent circuit having four series of parallel combination of resistance and capacitance for all specimens. The four RC components are assumed to be the core, shell, grain-boundary, and BaTiO₃/Ni electrode interface. The HALT measurement revealed that the interface resistance showed the significant degradation behavior during HALT. In addition, the degree of degradation of the interface resistance was dependent on the V concentration, showing the higher V concentration induced the better time-dependent resistance. The authors used scanning transmission electron microscopy–electron energy loss spectroscopy (STEM–EELS) to identify the distribution of V and found that a small but noticeable EELS signal of V at the ceramic/electrode interface. Thus, it was thought that V substitution at the interface between BaTiO₃ ceramic and Ni electrode seemed to improve the reliability of MLCCs.

2.4. Thermally stimulated depolarization current (TSDC) in BaTiO₃

TSDC is a technique to study the physical phenomena related to dipole moment. As shown in Figure 2.14, an electric field (E_p) is applied to a sample with a certain time (t_p) at a polarizing temperature (T_p). Then, the sample is cooled to room temperature under the bias. Under short-circuit conditions, the sample is heated with controlled heating rate ($3\text{ °C/min} - 5\text{ °C/min}$), and a current is monitored as a function of time simultaneously.

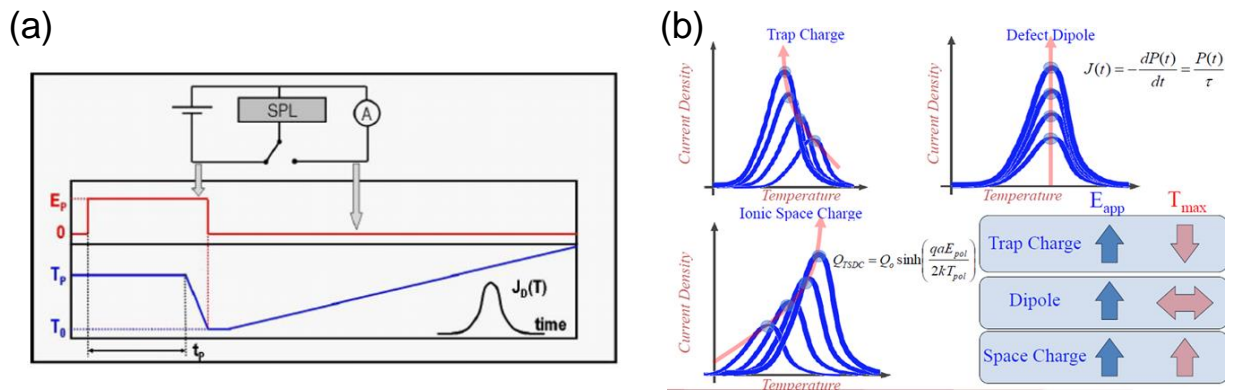


Figure 2.14 Schematic of (a) experimental procedure of TSDC and (b) analysis of TSDC with various polarization mechanisms. Courtesy of Dr. Clive Randall at Penn State University.

This technique provides useful information about point defects with their concentrations, activation energies and relaxation times associated with the polarization mechanisms as shown in Figure 2.14(b), which enables a better understanding on defect-related properties such as electrical conductivity in oxides. A good example of TSDC of undoped BaTiO₃[69] is shown in Figure 2.15. Sharp depolarization current peaks appear at the polymorphic phase transition temperatures in BaTiO₃ and they are thought to be related to the abrupt depolarization of remanent dipoles during the phase transition.

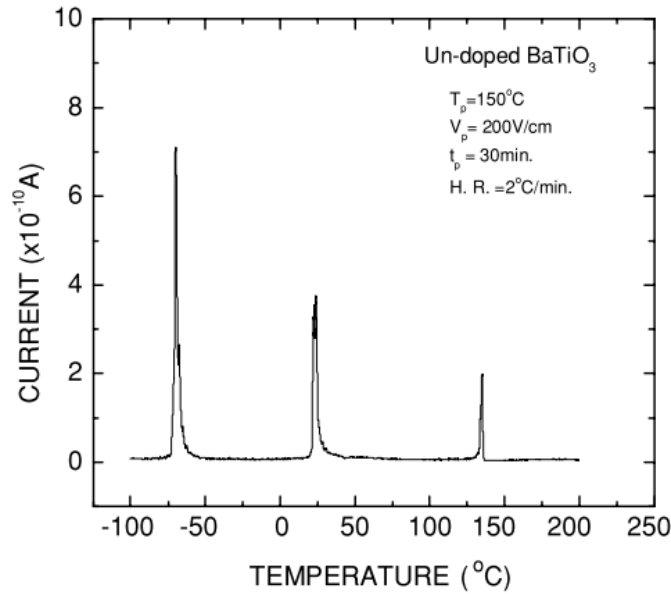


Figure 2.15 TSDC spectrum of undoped BaTiO₃. Reproduced with permission from [69].

Doping of either single- or multi-valent acceptor makes a significant change in TSDC and the phenomenon is highly dependent on doping concentration. Yoon et al. changed the single valent Mg concentration from 0.003 mol% to 0.1 mol% to investigate the Mg concentration dependent TSDC in BaTiO₃ ceramics.[70] In Figure 2.16, the relaxation temperature (T_m), the temperature where the maximum current density is observed, and the current density increased continuously as arising poling temperature (T_p). The increase in T_m with stronger polarization condition was attributed to the space charge.[71]

It was also found that T_m , T_p and the relaxation time (τ) decreased systemically with increasing Mg concentration under the condition in which the same magnitude of TSDC is generated. However, the activation energies in the relaxation process were close to ~ 0.9 eV regardless of Mg concentration, and these values are agreed to the activation energy of oxygen

migration in titanate-based oxides. Therefore, the authors believed that the higher doping concentration caused the higher oxygen vacancy concentration whose motion becomes faster (low τ) and more sensitive to temperature (low T_m) to achieve the same amount of TSDC.

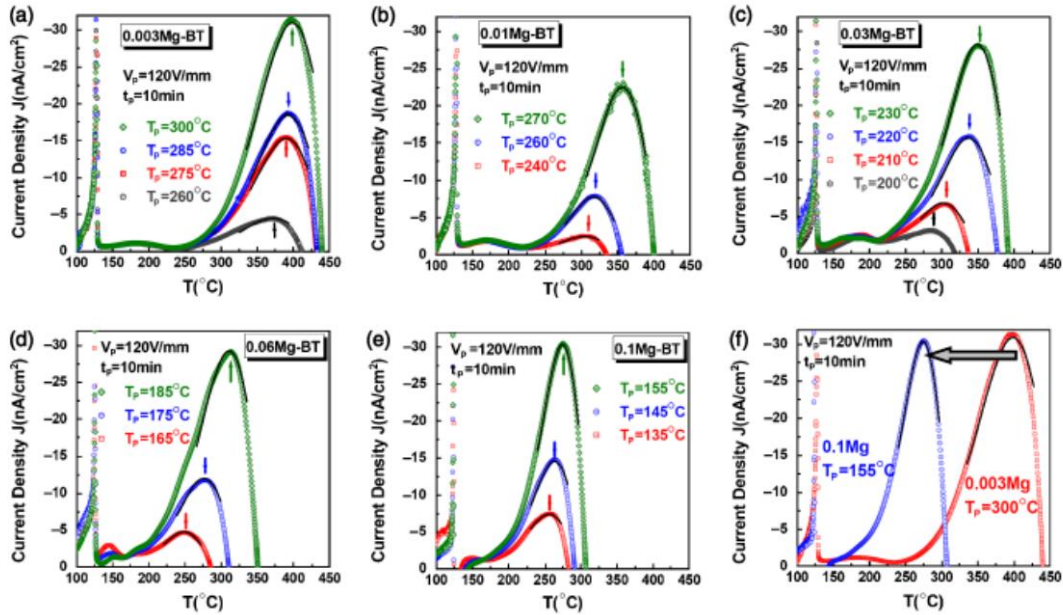


Figure 2.16 TSDC plots in Mg-doped BaTiO₃ ceramics with Mg concentration of (a) 0.003 mol%, (b) 0.01 mol% (c) 0.03 mol% (d) 0.06 mol% (e) 0.1 mol%. (f) Comparison of same magnitude of TSDC peaks of lowest (0.003 mol%) and highest Mg concentration (0.1 mol%) of Mg-doped BaTiO₃ ceramics. Reproduced with permission from [70].

Jeong et al. investigated the TSDC in multi-valent Mn-doped BaTiO₃ with the Mn concentrations of 0.5 mol% and 1 mol%. [72] Their study showed that a peak at the phase transition between the cubic and tetragonal phases decreased from 130 °C to 122 °C, when the Mn concentration varied from 0.5 mol% to 1 mol%. This was regarded as the deformation of unit cell by the higher number of oxygen vacancies, which resulted in the reduction of local tetragonality and curie temperature.

Higher temperature TSDC in Mn-doped BaTiO₃ was investigated by Yoon et al., The high-temperature TSDC above 300 °C is attributed to the relaxation process of trapped space charges. [73] The intensity of the broad peak at 300 °C raised as increasing Mn concentration, and the intensity of the peak and the corresponding relaxation temperature (T_m) increased with increasing the polarization DC field. Such behavior was attributed to the charge injection and

trapping at the trap site generated by Mn, and the further high DC fields reduced the T_m and the peak intensity by the de-trapping of charge with Poole-Frenkel mechanism which becomes dominant under the higher DC fields. The calculated activation energies for the relaxation process at all compositions were around 1.8 ~ 1.9 eV which are close to the energy level of the ionization of Mn^{3+}/Mn^{2+} measured from the top of the valence band.[46]

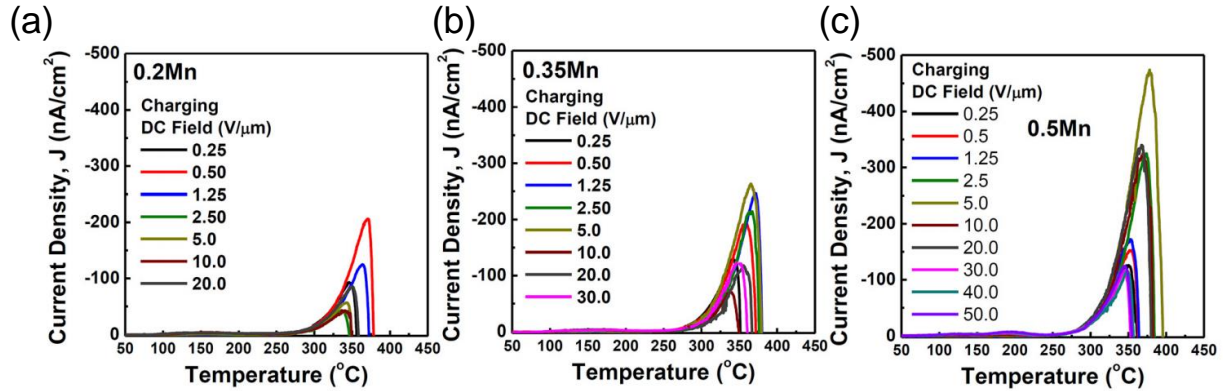


Figure 2.17 TSDC plots for Mn-doped BaTiO₃ MLCC with (a) 0.2 mol% Mn, (b) 0.35 mol% Mn and (c) 0.5 mol% Mn. Reproduced with permission from [72].

In Figure 2.17, there are very weak TSDC peaks at 100 – 200 °C, and the peaks were more closely discussed in Mn and V co-doped BaTiO₃ MLCC as shown in Figure 2.18.[74] The compositions were (1) 0.2 mol% Mn and 0.1 mol% V (0.2Mn0.1V), (2) 0.2 mol% Mn and 0.3 mol% V (0.2Mn0.3V), and (3) 0.4 mol% Mn and 0.3 mol% V (0.4Mn0.3V). In 0.2Mn0.1V and 0.2Mn0.3V, the intensity of the TSDC peak at around 150 – 160 °C increased systematically as the poling field (E_p) increased and then it saturated when the DC field is higher than 0.1 – 0.2 MV/cm. The peak position was fixed regardless of the magnitude of the field. This behavior was considered to the typical characteristics in the polarization process of dipoles.[71]

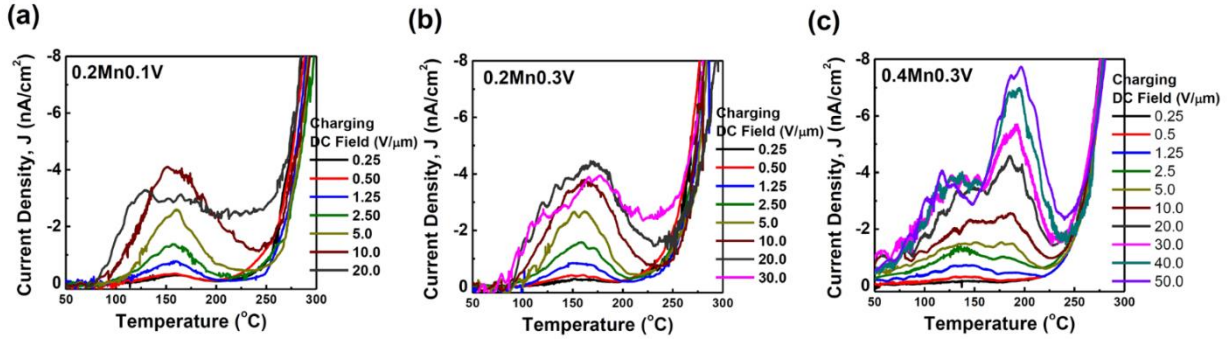


Figure 2.18 TSDC plots for Mn and V co-doped BaTiO₃ MLCC with (a) 0.2 mol% Mn and 0.1 mol% V, (b) 0.2 mol% Mn and 0.3 mol% V, and (c) 0.4 mol% and 0.3 mol% V. Reproduced with permission from [73].

Another TSDC peak appeared at around 200 °C in 0.4Mn0.3V with a high E_p such as 0.2 MV/cm in Figure 2.18(c). The intensity of the second peak saturated beyond E_p of 0.40 MV/cm and the peak position was also fixed, and thus the second peak was also suggested to be associated with dipole relaxation. By fitting the relaxation curve, the activation energies were confirmed to 0.61 eV – 0.7 eV and 0.51 eV – 0.65 eV in 0.2Mn0.1V and 0.2Mn0.3V, respectively. The activation energy for the second peak in 0.4Mn0.3V was 0.71 – 0.84 eV. It was argued that the origin of the first peak near 150 °C was not clear. It was suggested that the activation process is related to the charge trapping process associated to the second ionization of oxygen vacancies or the ionization of B-site ion (Ti⁴⁺) in perovskite materials. The second peak was believed to originate from the defect dipole of Mn and oxygen vacancies.

The similar TSDC peaks at this temperature range were also observed in Dy and Mn co-doped BaTiO₃ MLCC.[75] The compositions were 0.4 mol% Mn + 0.3 mol% Dy (0.3RE) 0.4 mol% + 0.9 mol% Dy (0.9RE). The peaks positions at 125 °C and 200 °C did not change as a function of poling field but their intensities increased as the increase of the DC field and then saturated, which is regarded as a typical characteristics of dipolar polarization process.

The activation energies of the relaxation process at 125°C and 200°C are respectively ~ 0.5 eV and ~ 0.73 eV, and the first peak activation energy was attributed to the spontaneous polarization of BaTiO₃, i.e. the phase transition from cubic phase to tetragonal phase. On the other hand, the activation energy with the second peak was attributed to the defect dipole. It was concluded that Dy acted as a donor to compensate Mn acceptor and thus the oxygen vacancies were reduced by the higher Dy concentration and therefore the number of defect dipole decreased.

2.5. Defect chemistry and electrical conductivity of β -Ga₂O₃

The temperature-dependent electrical conductivity in β -Ga₂O₃ single and polycrystalline was investigated by Fleischer and Meixner.[76] Arrhenius behavior of electrical conductivity of the single crystal showed the activation energy of 3.3 eV from 800 °C to 1000 °C in air. The Hall measurements revealed that as temperature changed from 800 °C to 1000 °C in air, the electron concentration increased from 10^{14} /cm³ to 10^{16} /cm³ with the thermal activation energy of 2.7 eV, and Hall mobility increased from 5 cm²/Vs to 15 cm²/Vs with the activation energy of 0.6 eV.

The conductivity of polycrystalline ceramics exhibited the same activation energy of 2.1 eV from 800 °C to 1000 °C in air. Hall measurements showed that the electron concentration is three orders of magnitude lower than the single crystal, i.e. 10^{13} /cm³ at 1000 °C. The activation energies for the carrier concentration and mobility are 1.5 eV and 0.65 eV, respectively.

Sasaki and Hijikata investigated the high-temperature equilibrium conductivity as a function of oxygen partial pressure in β -Ga₂O₃ ceramics.[21] In Figure 2.20, the isothermal electrical conductivity showed the relation, $\sigma \propto pO_2^{-1/4}$ from 800 °C to 950 °C in the pO_2 range of 1 atm to 10^{-3} atm. The pO_2 dependence was discussed with the two possible intrinsic defect reactions. One is the singly charged oxygen vacancies, and the other is doubly ionized gallium interstitials. In both models, the $\sigma \propto pO_2^{-1/4}$ relation can be obtained under the assumption that the electron is the predominant conducting species. The temperature-dependent electrical conductivity exhibited an Arrhenius behavior from 700°C ~ 950 °C in the same pO_2 range with the activation energy of 1.85(1) eV.

Similar pO_2 -dependence of electrical conductivity was reported by Cojocaru and Alecu.[23] In the work, the electrical conductivity of β -Ga₂O₃ ceramics was measured from 127 °C to 727 °C in the pO_2 range of 1 atm ~ 10^{-3} atm. Interestingly, even at 127 °C, the electrical conductivity was a function of $-1/4.55$ power of pO_2 , and became less pO_2 -dependence with increasing temperature. At 727 °C, the $\sigma \propto pO_2^{-1/3.73}$ relation was obtained. The pO_2 -dependence at various temperatures was attributed to the triply charged gallium interstitial model, however, the $-1/5.3$ power of pO_2 is expected rather than $-1/4.55$ in the model.

Defect chemistry of β -Ga₂O₃ thin films were investigated by Fleischer et al as shown in Figure 2.21.[24] The electrical conductivity versus pO_2 was measured from 850 °C to 1000 °C in the pO_2 range of 1 atm to 10^{-15} atm. The electrical conductivity at these conditions was a function

of pO_2 , $\sigma \propto pO_2^{-1/4}$ and the activation energy was 2.1 eV, and the pO_2 dependence was attributed to the oxygen vacancies. It is important to note that the electrical conductivity dropped significantly while the pO_2 changed from of 10^{-14} atm to 10^{-15} atm at 1000 °C. This phenomenon happened at these pO_2 range from 750 °C to 1000 °C. The electrical conductivity did not recover to its initial value after the measurement, and this phenomenon happened only above 750 °C. The phase transition in the Ga_2O_3 films were discussed as the possibility of the behavior, however, clear evidence was not suggested.

Chapter 3

Materials and Experimental Procedure

3.1. Synthesis of BaTiO₃ ceramics

A conventional solid-state reaction method was used to make various BaTiO₃ compositions. To minimize the unintentional background impurity, the experimental procedure was designed to allow for as little contamination from the environment as possible. High purity commercial powders of BaTiO₃ (99.995%, Sigma Aldrich), TiO₂ (99.998%, CERAC TM Incorporated, USA), MgO (99.99%, Sigma Aldrich), MnO₂ (99.99%, Sigma Aldrich) and Y₂O₃ (99.99%, Sigma Aldrich) were weighed in a chemical hood according to the molar ratio of compositions. The mixture was wet-milled for 2 h with Yttrium Stabilized Zirconia (YSZ) balls in anhydrous ethanol. It is important to note that the weight change of YSZ balls before and after the ball milling process is ~0.0009 g. This value can be converted to 7×10^{-6} and 2.3×10^{-4} molar fractions for Y₂O₃ and ZrO₂, respectively, in 1 mol of BaTiO₃. After ball-milling, the powders were dried at 80 °C for at least 12 h, and then calcined at 950 °C for 10 h in air. Pellets 20 mm in diameter and ~3 mm in thickness were compacted by uniaxial pressing at 45 MPa. At this point, no binder was used to avoid any contamination. Sintering was carried out at 1350 °C for 5 h in air, and during this process the sample was positioned on a Pt foil. The relative density measured by the Archimedes method was around 91 ~ 94% in all compositions. After the samples were polished using SiC papers from 800 grid to 1200 grit and diamond paste (down to 1 μm). Then, the polished specimens were thermally etched at 1200 °C for 30 min to observe the grain size. The grain size was obtained by an optical microscope (Olympus) with x20 ~ x50 magnitudes. X-ray diffraction patterns were measured using a Smart Lab (Rigaku, Japan) x-ray diffractometer with a Cu-Kα source. The sintered pellets exhibited a single perovskite structure with a tetragonal symmetry at room temperature.

3.2. (010) Fe-doped β -Ga₂O₃ single crystal

(010) Fe-doped β -Ga₂O₃ single crystals were grown via an edge-defined film-fed growth (EFG) method from Novel Crystal Technology, Inc. (Tamura Corporation). The unintentionally doped Si impurity is $1 \times 10^{17} / \text{cm}^3$ and the intentionally doped Fe concentration is $8 \times 10^{17} / \text{cm}^3$. [77] The single crystal shows the electrically semi-insulating properties, $\sim 10^{10} \Omega \cdot \text{cm}$ at room temperature. The dimension of the received crystal was 20 mm (length) \times 5 mm (width) \times 0.5 mm (thickness), and the top and bottom were chemically and mechanically polished by the vendor.

3.3. Four-point-probe DC method

In this dissertation, DC electrical measurements are based on the four-point-probe method, which is very useful to obtain a precise resistance of specimen, when a contact resistance is high. A current is applied through two outer contacts near the sample edges and a potential drop is measured across inner contacts. Thus, the interfacial resistance between sample and electrodes is eliminated. A comparison between four-point and two-point-probe methods is shown in Figure 3.1. The test material is Fe-doped (010) β -Ga₂O₃ single crystal with sputtered Pt electrodes. The contact resistance of Pt on Fe-doped (010) β -Ga₂O₃ single crystal is very high as shown in Figure

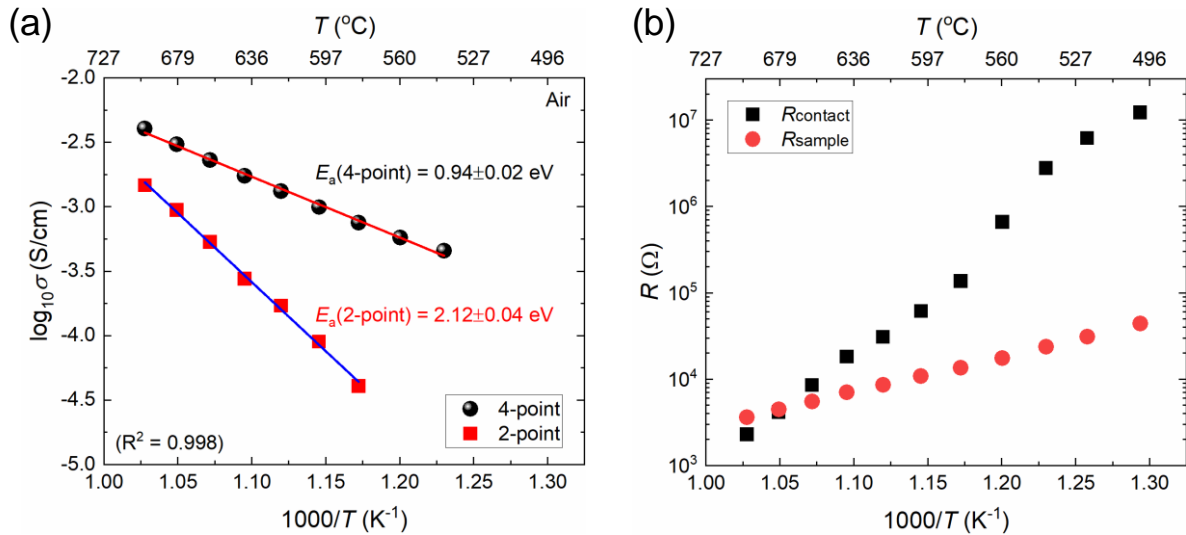


Figure 3.1 Comparison of (a) four-point and two-point-probe DC conductivities and (b) contact and sample resistances in Fe-doped β -Ga₂O₃ single crystal at different temperature in air.

3.1(b) and thus the total electrical conductivity of the sample is predominantly limited by the contact resistance in two-point-probe measurement.

Rectangular bar type BaTiO_3 ceramics and Ga_2O_3 single crystals were wrapped by 3M tapes spaced by 2 ~ 3 mm in width as shown in Figure 3.2(a). Dense four linear Pt electrodes (~ 500 nm) were deposited on sample surfaces (bottom, top, and two sides) using a DC sputtering system, and the samples were subsequently annealed at 850 °C in air for 30 min to achieve a better electrical contact. Then, the sample was wrapped with 0.25 mm Pt wires and the fixture was physically connected to a long sample holder.

Oxygen partial pressure ($p\text{O}_2$) was controlled from 0.21 atm (air) to 10^{-4} atm (Ar atmosphere) by varying the flow rate of Ar and O_2 gas. The actual $p\text{O}_2$ was measured with a zirconia oxygen sensor (Ceramic Oxide Fabricators, Australia). It should be noted that the $p\text{O}_2$ in pure Ar can be varied between $\sim 10^{-5}$ atm and $\sim 10^{-4}$ atm depending on the gas purity and the degree of leak in the measurement system. As soon as the $p\text{O}_2$ was changed at a given temperature, a small current between 700 μA to 10 μA was applied to the sample and the time-dependent four-wire resistance was continuously monitored with a multimeter (Keithley 2000, Agilent) as shown Figure 7(b). Once the resistance was stable as a function of time, the sample was assumed to be thermally and chemically equilibrated.

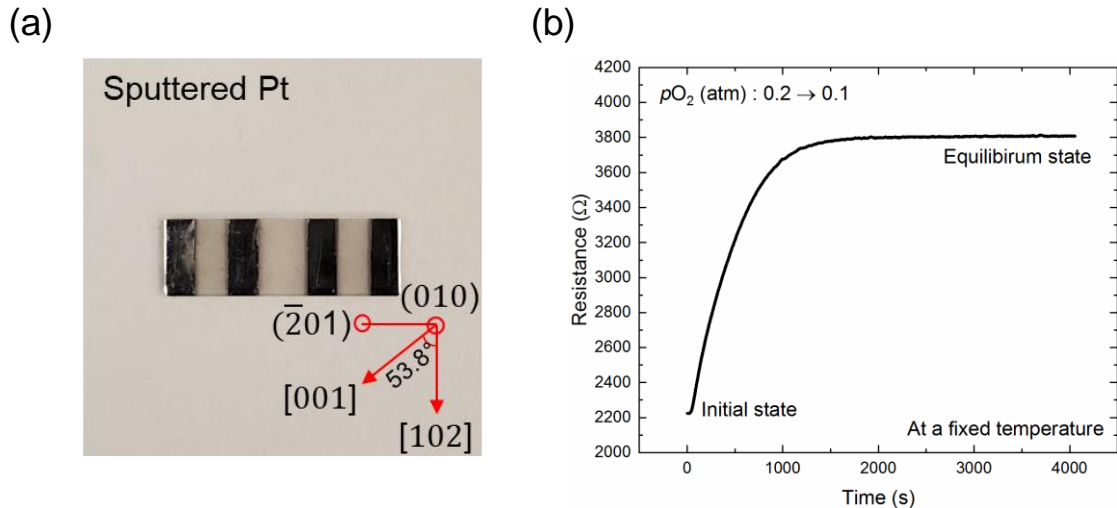


Figure 3.2 (a) Top view of Fe-doped (010) $\beta\text{-Ga}_2\text{O}_3$ single crystal and sputtered Pt electrodes the black arrow indicates the measurement direction (b) time-dependent four-wire resistance with a change in $p\text{O}_2$ at a given temperature.

3.4. AC impedance

HP 4192A impedance analyzer was used to study the AC impedance characteristics of both BaTiO₃ and β -Ga₂O₃ samples. For BaTiO₃, the top and bottom of thin samples were deposited by a few hundreds of Pt, i.e. two-point AC technique. Then, the samples were pasted with thick (0.3 ~ 0.4 mm) Pt wires using Pt paste. The fixtures were physically screwed with thick Pt leads on the sample holder. In the case of Fe-doped (010) β -Ga₂O₃ single crystal, the sample and electrode geometry were the same as the one for the DC measurement (Figure 3.2(a)), i.e. four-wire measurement. The measurement range of temperature were between 150 ~ 800°C in air. The real temperature of furnace was monitored by *s*-type thermocouples. At a given temperature, the samples were chemically and thermally equilibrated, meaning the resistance of samples do not change as a function of time.

A small AC signal of 0.5 V ~ 1.0 V was applied on the samples with a frequency range of 5 MHz ~ 5 Hz to obtain AC data, which are the real and imaginary parts of admittance (Y' and Y''). The collected admittance was converted to all other AC formalisms, modulus, impedance, permittivity, and capacitance using the relations:

$$Y^* = Y' + iY'' \quad (3.1)$$

$$Y^* = \frac{1}{Z^*} \quad (3.2)$$

$$M^* = i\omega C_0 Z^* \quad (3.3)$$

$$\epsilon^* = \frac{1}{M^*} \quad (3.4)$$

where Y^* is the complex admittance, Z^* is the complex impedance, M^* is the complex modulus, i is the imaginary number, ω is the angular frequency, C_0 is the capacitance of open cell. The real (Z') and imaginary (Z'') parts of impedance were used to construct Cole-Cole plots for analyzing a resistance of sample. Cole-Cole plots are then fitted by multiple equivalent circuits with EIS Spectrum Analyser.

3.5. Prediction of defect structure

Defect structures of BaTiO₃ are explored by solving the charge neutrality equations (Eq. 2.13) in Chapter 2 using Matlab codes. The codes in the dissertation are a modified version of codes which were developed for the TiO₂ system.[78] At this point, a concentration of each point defect (particles/cm³) is produced as a function of oxygen partial pressure (atm) at a given temperature. The code can calculate both full equilibrium defect concentrations at an equilibrium temperature (T_E) and quenched defect structures at a low-temperature (T_Q). In the case of the low-temperature partial defect equilibria, the structure can be built under the assumptions that the concentration of cation vacancy is fixed from a high-temperature condition, generally sintering conditions but that of the electronic carriers (n and p) and oxygen vacancy are allowed to be fully equilibrated at T_Q , which is a temperature for any electrical measurements.

```
%%%%%%%%%%%%%%%%%%%%%%%%%%%%%%%%%%%%%%%%%%%%%%%%%%%%%%%%%%%%%%%%%%%%%%%% Section A %%%%%%%%%%%%%%%%%%%%%%%%%%%%%%%%%%%%%%%%%%%%%%%%%%%%%%%%%%%%%%%%%%%%%%%%%
k = 8.61733e-5; % boltzmann constant in eV/oK
e = 1.6E-19; % elementary charge C
TE = 1150+273; % equilibrium temp in Kelvin
TQ = 900+273;% quenched temp in Kelvin
a = logspace(-20,5,50); % oxygen partial pressure range in atm (lowest, highest, interval)
M = length(a); % defining vectors to fill in with values later
CV02 = ones(1,M);
CV02_1 = ones(1,M);
CV02q = ones(1,M);
CV02q_1 = ones(1,M);
CVTi4 = ones(1,M);
CVTi4_1 = ones(1,M);
n = ones(1,M);
nq = ones(1,M);
p = ones(1,M);
pq = ones(1,M);

%%%%%%%%%%%%%%%%%%%%%%%%%%%%%%%%%%%%%%%%%%%%%%%%%%%%%%%%%%%%%%%%%%%%%%%% Section B %%%%%%%%%%%%%%%%%%%%%%%%%%%%%%%%%%%%%%%%%%%%%%%%%%%%%%%%%%%%%%%%%%%%%%%%%
% set doping level

CMg = 1E20; % single-valent Mg concentration
CY = 1E20; % single-valent Y concentration

%%%%%%%%%%%%%%%%%%%%%%%%%%%%%%%%%%%%%%%%%%%%%%%%%%%%%%%%%%%%%%%%%%%%%%%% Section C %%%%%%%%%%%%%%%%%%%%%%%%%%%%%%%%%%%%%%%%%%%%%%%%%%%%%%%%%%%%%%%%%%%%%%%%%

% Below is for obtaining a full equilibrium defect structure at TE

KR=1.06E71*exp(-5.69/(k*TE)); % K for the reduction reaction in cm^9atm^1/2 by J. Nowotny and
```

```

M. Rekas, Ceram. Int. 20, 257 (1994).
Ki=8.55E44*exp(-2.91/(k*TE)); % K for the intrinsic equilibrium in cm-6 by J. Nowotny and
M. Rekas, Ceram. Int. 20, 257 (1994).
KS=3.4E105*exp(-2.795/(k*TE)); % K for the Schottky reaction in cm-15 by J. Nowotny and
M. Rekas, Ceram. Int. 20, 257 (1994).

for i = 1:M
% y = a(1,i); % y is an oxygen partial pressure in atm. (Denoting pO2 value for each iteration)
y = 0.21; % if you want to fix the cation vacancy in air condition, then let y = 0.21 but
deactivate y = a(1,i) above.
x = sym('x'); % a number of electron, n, which is defined as a variable, x
CV02_1 = KR/(x^2)*(y^(-1/2)); % a converted form for oxygen vacancy concentration
CVTi4_1= (KS/(KR^3))^(1/2)*(x^3)*(y^(3/4)); % a converted form for cation vacancy concentration
eqn1 = x + 2*CMg + 6*CVTi4_1 == (Ki/x) + 2*CV02_1 + CY; % the total charge neutrality equation
sol1 = vpsolve(eqn1,x,[1e0 1e25]); % finding solution for the equation with the boundary
condition in the bracket(range of solution)
n(1,i) = sol1; % a concentration of electron
CVTi4(1,i) = (KS/(KR^3))^(1/2)*n(1,i)^3*(y^(3/4)); % a concentration of cation vacancies
(Schottky reaction)
end

%%%%%%%%%%%%%%%%%%%%%%%%%%%%%%%%%%%%%%%%%%%%%%%%%%%%%%%%%%%%%%%%%%%%%%%% Section D %%%%%%%%%%%%%%%%%%%%%%%%%%%%%%%%%%%%%%%%%%%%%%%%%%%%%%%%%%%%%%%%%%%%%%%%%

% Below is for obtaining a quenched defect structure at TQ.
% To obtain full defect equilibria at TE, you should set TE=TQ and activate y=a(1,i) in the above
section.

KRq=1.06E71*exp(-5.69/(k*TQ));
Kiq=8.55E44*exp(-2.91/(k*TQ));

for i = 1:M
y = a(1,i);
z = sym('z');
CV02q_1 = KRq/(z^2)*(y^(-1/2));
CVTi4q_1(1,i) = CVTi4(1,i); % Cation vacancies are frozen-in at TE
eqn2 = z + 2*CMg + 6*CVTi4q_1(1,i) == (Kiq/z) + 2*CV02q_1 + CY;
sol2 = vpsolve(eqn2,z,[1e0 1e25]);
nq(1,i) = sol2;
pq(1,i) = Kiq/nq(1,i);
CV02q(1,i) = KRq/(nq(1,i)^2)*(y^(-1/2));
CMgt(1,i) = CMg;
Cyt(1,i) = CY;
end

%%%%%%%%%%%%%%%%%%%%%%%%%%%%%%%%%%%%%%%%%%%%%%%%%%%%%%%%%%%%%%%%%%%%%%%% Section E %%%%%%%%%%%%%%%%%%%%%%%%%%%%%%%%%%%%%%%%%%%%%%%%%%%%%%%%%%%%%%%%%%%%%%%%%

figure;
plot(log10(a),log10(nq),'-s','color',[255/255 0/255 0/255],'MarkerSize',9, 'linewidth', 1.5);
hold on
plot(log10(a),log10(pq),'-o', 'color',[0/255 0/255 255/255],'MarkerSize',9, 'linewidth', 1.5);
plot(log10(a),log10(CV02q),'-d', 'color',[0/255 255/255 0/255], 'MarkerSize',9, 'linewidth', 1.5);
plot(log10(a),log10(CVTi4),'->', 'color',[0/255 0/255 128/255],'MarkerSize',9, 'linewidth', 1.5);
plot(log10(a),log10(CMgt),'-<', 'color',[200/255 200/255 10/255],'MarkerSize',9, 'linewidth',

```

```

1.5);
plot(log10(a),log10(Cyt),'-p', 'Color',[0/255 0/255 0/255],'MarkerSize',9, 'linewidth', 1.5);
hold off

xlabel('log10 itp\rm0.2 (atm)');
ylabel('log10 [ ] (cmΛ-Λ3)');
set(gca,'FontSize',14);
set(gcf, 'Position', [200, 200, 800, 700]);
legend('n','p','V0Λ+', 'VT-iΛ+(=VB-aΛ2Λ+) ', 'MgT-iΛ2Λ- ', 'YB-aΛ1Λ+', 'Location',
'southwest');
axis([-20 5 14 22]);
t1=text(-20.0, 22.3, ['TE = ' num2str(TE-273) ' ΛoC' ' ' 'TQ = ' num2str(TQ-273) ' ΛoC']);
t1.FontSize = 14;
print cropcircledemo.png -dpng -r600 -painters

```

Chapter 4

Electrical Conductivity of Mg or Mn Singly doped BaTiO₃

4.1. Introduction

The effects of single doping of acceptor on the electrical conductivity have been widely investigated to understand the defect chemistry of BaTiO₃, [43, 46, 54, 55, 57, 79–81] However, most of the literatures were focused on the high-temperature equilibrium electrical conductivity, and systematic investigations were not explored with reducing temperature where defect compensating mechanism can be affected by other factors such as grain-boundary. Moreover, capacitors are operated under two-points DC bias at low-temperature where the contact resistance also plays a significant role. Thus, it is motivated to explore the electrical conductivity over a wide range of temperature with both four-point and two-point DC/AC electrical measurements.

In MLCCs, single-valent Mg and multivalent Mn are widely used as acceptors. [14, 67] Yoon et al., systematically investigated the doping effects of Mg and Mn on electrical conductivity and degradation. [48, 58–61] Their studies revealed that the Mg has negative impacts on both bulk conductivity and degradation resistance regardless of grain size. On the other hand, Mn is regarded as an effective acceptor for improving degradation of BaTiO₃ due to the multivalent characteristic of Mn. Although their studies show the systematic and clear trend in electrical conductivity and degradation behavior of Mg-doped BaTiO₃, only ionic transference number and degradation characteristics were discussed in Mn-doped BaTiO₃. Thus, the effects of Mn are not very clear in terms of the bulk and grain-boundary conductivity at changing temperature.

In this chapter, the comprehensive DC and AC electrical conductivities of BaTiO₃ ceramics doped by either 0.5 mol% of single-valent Mg or 0.5 mol% of multivalent Mn were compared in a wide range of temperature and oxygen partial pressure to better understand the role each dopant depending on temperature. In addition, this chapter is proposed to help readers to digest the following co-doping effects of donor and acceptor in BaTiO₃ (Chapter 5). The samples were made

via a solid-state reaction method and the details can be found in Chapter 5. Four-points probe DC measurements were made at both high (900°C) and low (500°C) temperature to explore electrical conductivity versus oxygen partial pressure to understand defect chemistry with each dopant. In addition, two-point AC impedance measurements were conducted to figure out the origin of frequency-dependent responses with changing temperature. Details in the relative permittivity with Curie-Weiss law are discussed to identify the high- and low-frequency responses. Fitting of Cole-Cole plots with AC formalisms are shown, and the selection of proper equivalent circuit is discussed. Finally, the bulk and grain-boundary conductivities were compared to the DC electrical conductivity.

4.2. Results and Discussion

Figure 4.1 shows the high-temperature DC electrical conductivity as a function of time in a high oxygen partial pressure (pO_2) range of 0.21 atm (air) $\sim 10^{-4}$ atm at 900 °C in Mg or Mn-doped BaTiO₃. The electrical conductivity of both Mg and Mn samples were equilibrated within 2 hours after a reduction in pO_2 of one decade between 0.21 atm and 10^{-3} atm, suggesting that both samples are partially equilibrated in a given condition where the cations are assumed to be frozen-in, while the oxygen vacancies are fully equilibrated.[82–84] In 10^{-4} atm of pO_2 , it is seen that the electrical conductivity stabilized in ~ 14 hours and ~ 5 hours with Mg-doping and Mn-doping, respectively. At lower temperature 500 °C, the relaxation time increased up to ~ 10 hours during

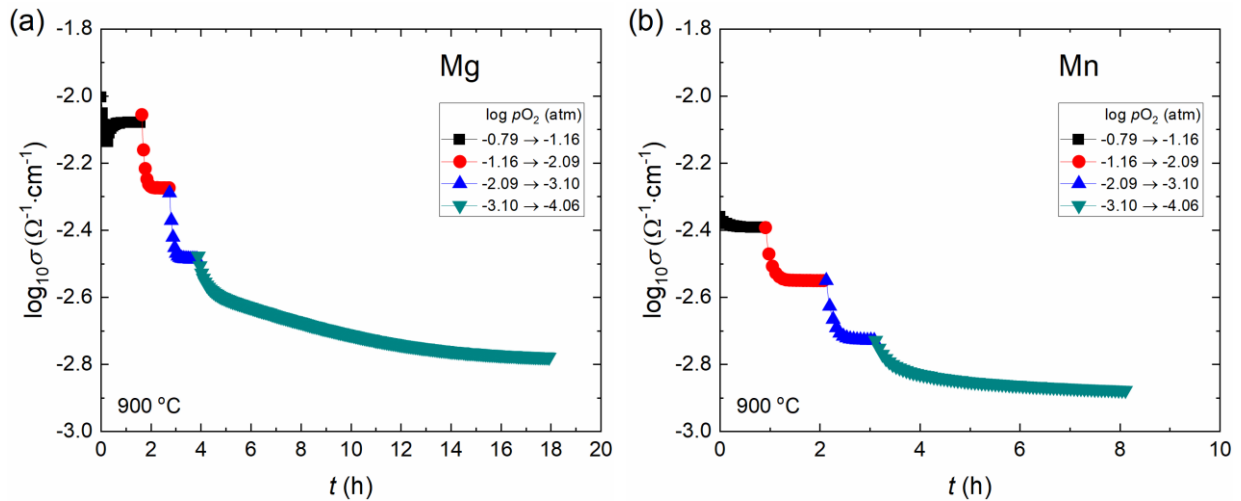


Figure 4.1 Time-dependent DC electrical conductivity at various oxygen partial pressure in (a) Mg-doped BaTiO₃ and (b) Mn-doped BaTiO₃ at 900 °C.

the four-point-probe DC measurements with a decrease in pO_2 of one decade, which is probably due to the slow process of oxygen exchange.

A summary of DC electrical conductivity of Mg or Mn doped BaTiO₃ as a function of pO_2 from air to 10⁻⁴ atm at 900 °C and 500 °C is shown in Figure 4.2. At both temperatures, Mg or Mn-doped BaTiO₃ were consistent with p -type electronic conduction exhibiting either a 1/4 or 1/6 slope in $\log_{10}\sigma$ versus $\log_{10}pO_2$, which is generally expected for acceptor-doped BaTiO₃ processed in these pO_2 range.[43, 55, 57, 80]

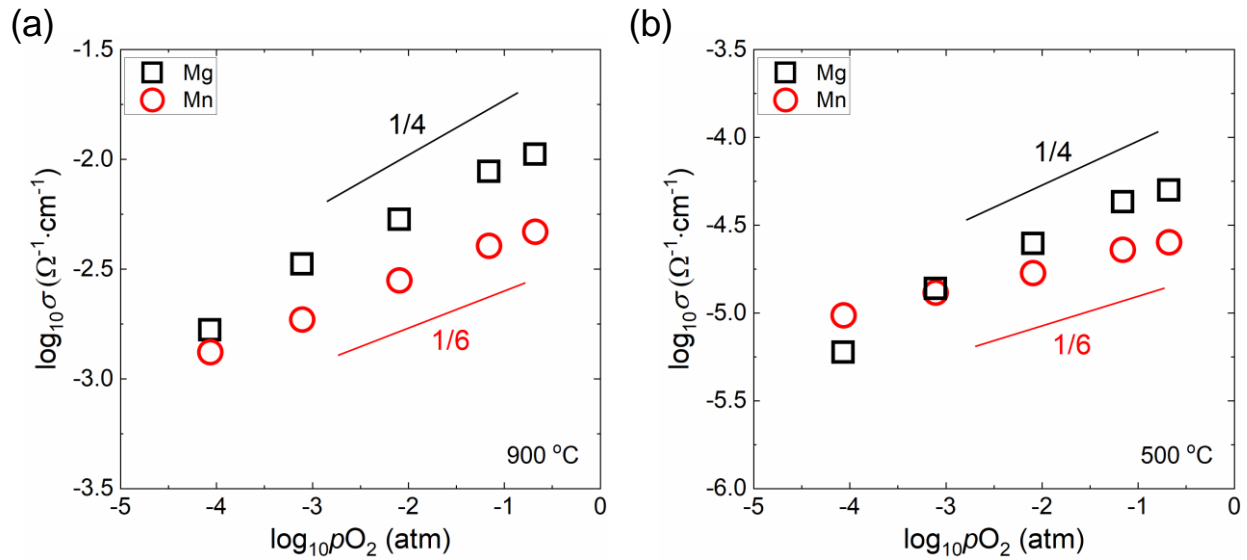
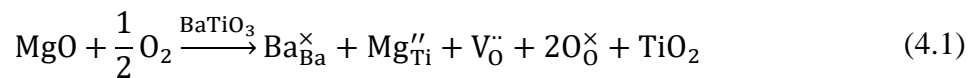


Figure 4.2 DC electrical conductivity as a function of oxygen partial pressure in Mg or Mn-doped BaTiO₃ at (a) 900 °C and (b) 500 °C.

In Mg-doped BaTiO₃, the oxidation reaction could be the origin of the p -type conduction which can be expressed as Kröger-Vink notation.[55, 80] When MgO is incorporated into BaTiO₃, the ionic compensation occurs by the oxygen vacancies:



In a high pO_2 range, the oxidation reaction can be written as:



whose equilibrium constant, K_O is

$$K_O = \frac{p^2}{P_{O_2}^{1/2} [V_{O}^{\bullet\bullet}]} = K'_O \exp\left(-\frac{\Delta H_O}{k_B T}\right) \quad (4.3)$$

where p is a hole concentration, P_{O_2} is an oxygen partial pressure, $[V_{O}^{\bullet\bullet}]$ is a number of oxygen vacancy, K'_O is a pre-exponential factor, ΔH_O is an enthalpy for the oxidation reaction, k_B is the Boltzmann constant and T is an equilibrium temperature. At a given temperature, K_O is a constant and $[V_{O}^{\bullet\bullet}]$ is extrinsically fixed by Mg doping, i.e. $[V_{O}^{\bullet\bullet}] \approx [Mg_{Ti}^{\prime\prime}]$, and thus the total electrical conductivity (σ_T) is proportional to p by assuming that the electron and ionic conductivities are negligible and the hole mobility (μ_h) is constant at these pO_2 regime. Therefore, the total conductivity is expressed as:

$$\sigma \approx pe\mu_h \approx (K_O [Mg_{Ti}^{\prime\prime}])^{1/2} P_{O_2}^{1/4} \quad (4.4)$$

where e is the elementary charge.

In case of Mn-doped BaTiO₃, defect chemistry models involving the reduction reaction, ionization of Mn and the internal equilibrium explains the p -type conduction mechanism.[43, 57] The equilibrium reduction reaction and its equilibrium constant (K_R) are expressed as:



$$K_R = [V_O^{\bullet\bullet}] P_{O_2}^{1/2} n^2 = K'_R \exp\left(-\frac{\Delta H_R}{k_B T}\right) \quad (4.6)$$

where n is a concentration of electron, K'_R is a pre-exponential factor, and ΔH_R is an enthalpy of reduction reaction. The two ionization reactions of Mn in equilibrium and corresponding equilibrium constants (K_{Mn1} , and K_{Mn2}) can be written as:[46]



$$K_{Mn1} = \frac{[Mn^{\times}_{Ti}]n}{[Mn'_{Ti}]} = 2N_C \exp\left(-\frac{E_g - E_{Mn1}}{k_B T}\right) \quad (4.9)$$

$$K_{\text{Mn2}} = \frac{[\text{Mn}'_{\text{Ti}}]n}{[\text{Mn}''_{\text{Ti}}]} = 1/2 N_{\text{C}} \exp\left(-\frac{E_{\text{g}} - E_{\text{Mn2}}}{k_{\text{B}}T}\right) \quad (4.10)$$

where N_{C} is the effective density of states of the conduction band, E_{g} is the band gap of BaTiO_3 , and E_{Mn1} and E_{Mn2} is the first and secondary ionization energies of Mn measured from the top of the valence band. The total amount of Mn ($[\text{Mn}_{\text{Ti}}]_{\text{T}}$) is the summation of the concentration of multi-valent Mn.

$$[\text{Mn}_{\text{Ti}}]_{\text{T}} = [\text{Mn}^{\times}_{\text{Ti}}] + [\text{Mn}'_{\text{Ti}}] + [\text{Mn}''_{\text{Ti}}] \quad (4.11)$$

where $[\text{Mn}^{\times}_{\text{Ti}}]$, $[\text{Mn}'_{\text{Ti}}]$, and $[\text{Mn}''_{\text{Ti}}]$ are the concentration of neutral, first ionized and secondary ionized Mn, respectively. The internal electronic equilibrium and its equilibrium constant can be expressed as,

$$\text{null} = e' + h' \quad (4.12)$$

$$K_{\text{i}} = np = K'_{\text{i}} \exp\left(-\frac{E_{\text{g}}}{k_{\text{B}}T}\right) \quad (4.13)$$

From Eq. 4-6 and 4-13, the hole concentration is expressed as:

$$p = K_{\text{i}} K_{\text{R}}^{-1/2} [\text{V}_{\text{O}}^{\cdot\cdot}]^{1/2} P_{\text{O}_2}^{1/4} \quad (4.14)$$

At a high $p\text{O}_2$ regime, Eq. 4-14 can be rearranged using Eq. 4-9, Eq. 4-10, and Eq. 4-13 with $2[\text{V}_{\text{O}}^{\cdot\cdot}] \approx [\text{Mn}'_{\text{Ti}}]$ and $[\text{Mn}_{\text{Ti}}]_{\text{T}} \approx [\text{Mn}^{\times}_{\text{Ti}}]$ [43] with the assumption that the total conductivity is predominantly limited by the hole concentration,

$$\sigma \approx pe\mu_h \approx e\mu_h K_{\text{i}} \left(\frac{[\text{Mn}_{\text{Ti}}]_{\text{T}}}{2K_{\text{R}}K_{\text{Mn1}}}\right)^{1/3} P_{\text{O}_2}^{1/6} \quad (4.15)$$

Therefore, the $p\text{O}_2$ -dependent electrical conductivity is observed in Mn-doped BaTiO_3 with a 1/6 slope in $\log_{10}\sigma$ versus $\log_{10}P_{\text{O}_2}$.

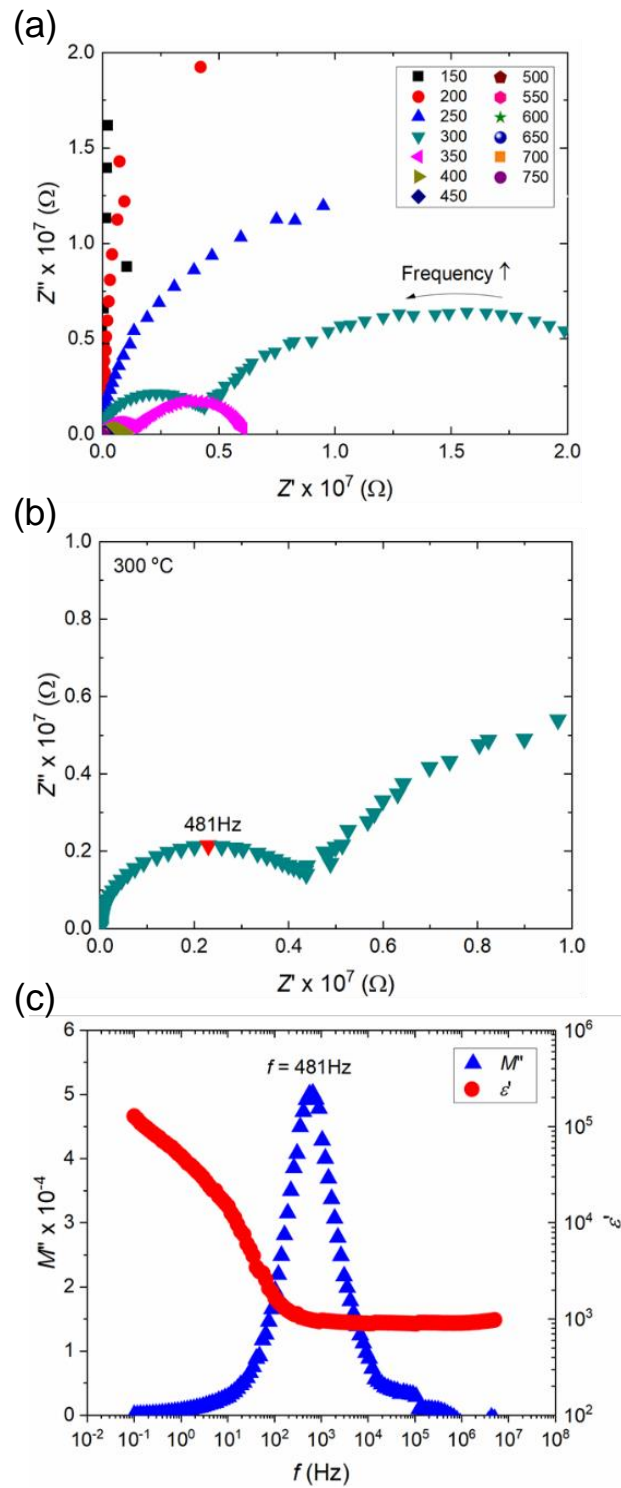


Figure 4.3 (a) Cole-Cole plot of Mn-doped BaTiO₃ as a function of temperature. (b) High-frequency arc and (c) corresponding imaginary part of modulus and real part of relative permittivity at 300 °C.

Temperature-dependent electrical conductivity was analyzed by measuring AC impedance in air condition. The real and imaginary parts of the impedance called Cole-Cole plots in Mn-doped BaTiO₃ are exhibited in Figure 4.3(a). At low-temperature, the resistance of sample was too high, and thus only partial semi-circle is seen in Cole-Cole plot. At 300°C, two clear semi-circles were observed, and the total impedance was mainly limited by the low-frequency arc. With increasing temperature, the impedance of low-frequency arcs decreased significantly compared to that of the high-frequency arc. To figure out the origin of two different frequency responses, the imaginary part of modulus (M'') and the real (ϵ') and imaginary part (ϵ'') of relative permittivity were more closely investigated. The high-frequency arc in Cole-Cole plot at 300 °C in Figure 4.3(b) corresponds to the peak of the M'' and the frequency plateau of ϵ' in Figure 4.3(c). The low-frequency large semi-circle seems to correspond to the slope in the real part of relative permittivity whose value is $\sim 10^5$ at a frequency range of 10^{-1} Hz to 10^0 Hz in Figure 4.3(c).

The relative permittivity is then extracted from the high-frequency plateau at various temperature as shown in Figure 4.4(b). The obtained high-frequency relative permittivity were around 1500 ~ 2500 at a temperature range of 150 °C ~ 250 °C, which is reasonable values for BaTiO₃.^[85] The permittivity is then analyzed with respect to Curie-Weiss law:

$$\epsilon = \frac{C_0}{(T - T_0)} \quad (5.16)$$

where ϵ is the relative permittivity, C_0 is the Curie constant, T is the temperature, and T_0 is the Curie temperature. As shown in Figure 5.4(d), the high-frequency relative permittivity follows Curie-Weiss law up to 250 °C. The obtained Curie temperature and Curie constant in Mn-doped BaTiO₃ were respectively 114.0 ± 0.9 (°C) and 167209 ± 1766 (°C), and those of Mg-doped BaTiO₃ analyzed in the same manner as Mn-doped BaTiO₃ were 96.8 ± 0.2 (°C) and 114007 ± 1861 (°C), which are the reasonable values for BaTiO₃.^[70] Therefore, the high-frequency arc in Cole-Cole plots of Mn-doped and Mg-doped BaTiO₃ seems to be originated from the bulk response. On the other hand, the low-frequency plateau of relative permittivity is almost temperature-independent, and the capacitances corresponding to the low-frequency arcs are on the order of 10^{-9} F at these temperature range in both cases, highly suggesting that the low-frequency arcs are attributed to the grain-boundary responses.^[61, 85, 86]

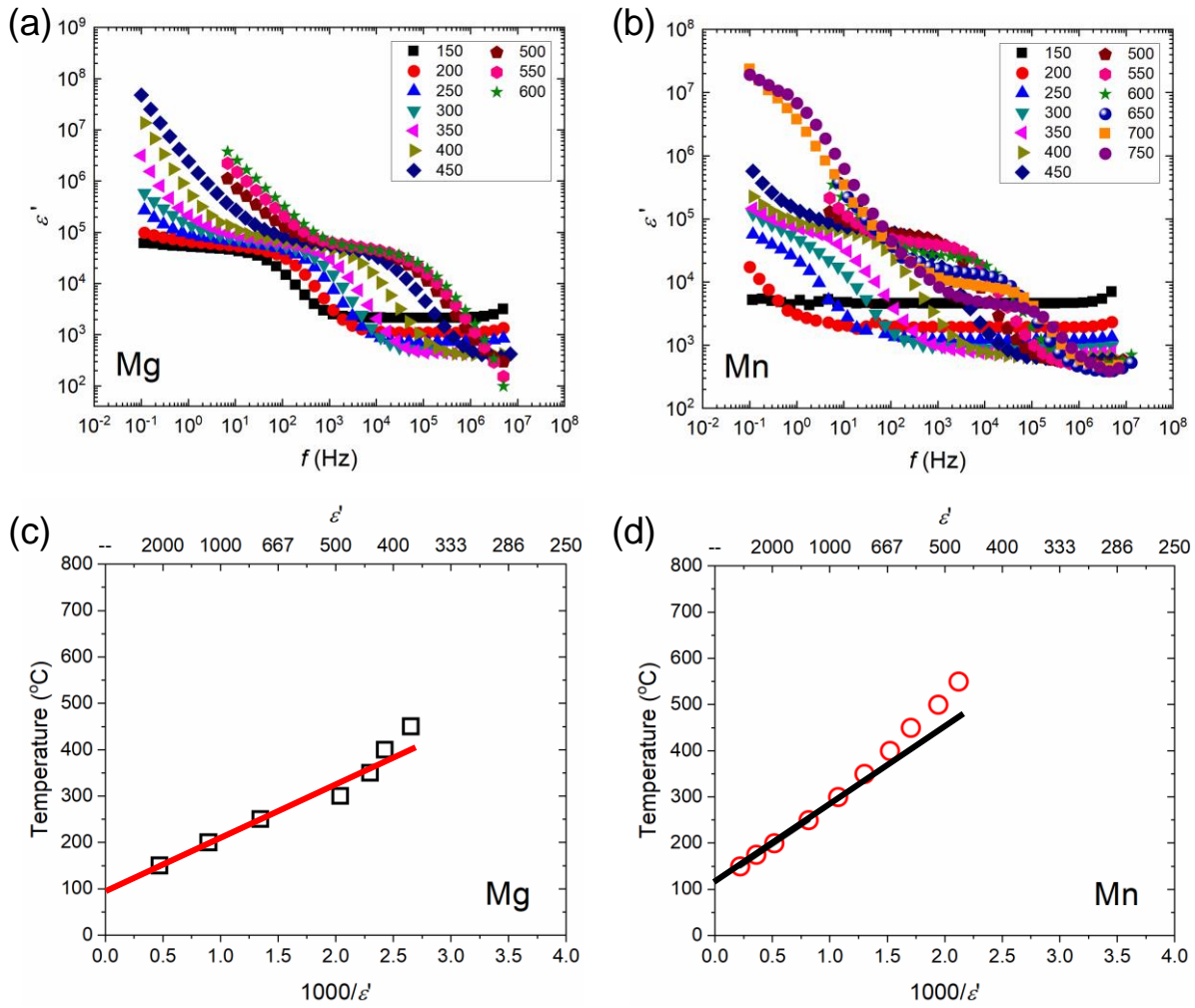


Figure 4.4 Real part of relative permittivity at various temperature in (a) Mg-doped and (b) Mn-doped BaTiO₃. Curie-Weiss fitting in (c) Mg-doping and (d) Mn-doping.

Based on the AC impedance analyses, Cole-Cole plots were fitted using equivalent circuits consisting of either one parallel resistor (R)-constant phase element (CPE) for low-temperature where one large arc was observed or two parallel R-CPE in series for higher range of temperature where the two arcs were obtained in Cole-Cole plots. Good examples of AC fitting at 500 °C in the Mg and Mn samples are shown in Figure 4.5. It is worth noting that the low-frequency arc in Mg-doped BaTiO₃ at 500 °C has an additional third response in Figure 4.5(a), which seems to be attributed to the interfacial effects between sample and electrode.[87] This third element in Mg-doped sample was not included during fitting of Cole-Cole plots.

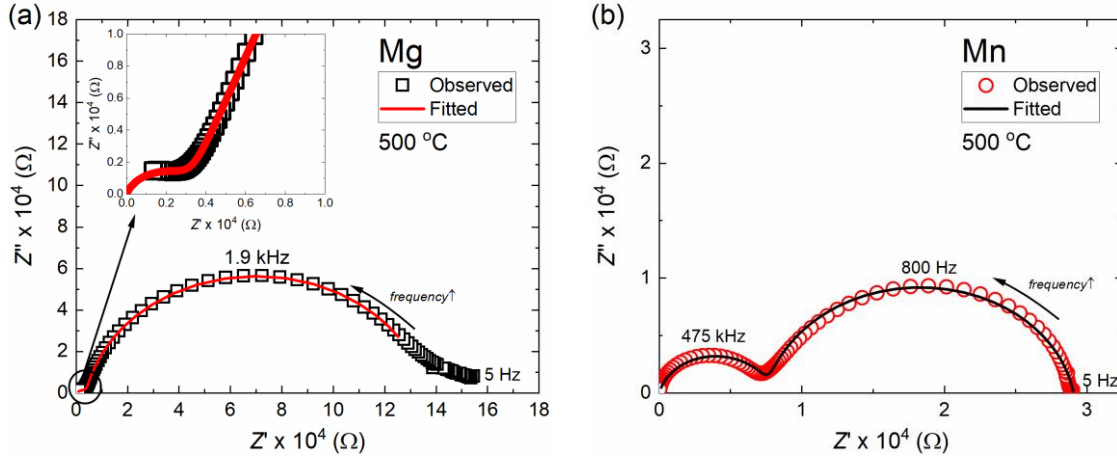


Figure 4.5 Observed and fitted Cole-Cole plots of (a) Mg-doped BaTiO₃ and (b) Mn-doped BaTiO₃ at 500 °C.

Overall, Cole-Cole plots were well fitted with the two R-CPE equivalent circuits in both specimens, however, there seems to be an additional frequency-dependent component between two main arcs in Mn-doped BaTiO₃ at 500 °C as shown in Figure 4.5(b). In Figure 4.6, the observed frequency-dependent AC formalisms were compared to the simulated AC formalisms which were back calculated from the fitted Cole-Cole plots. While the AC formalisms of Mg-doped BaTiO₃ are well matched to the simulated formalisms, there is discrepancies between the observed and simulated AC formalisms in Mn-doped BaTiO₃, especially, at the intermediate frequency range of 10⁴ Hz ~ 10⁵ Hz. The third element at the intermediate frequency range seems to appear at a specific temperature range of 350 °C ~ 600 °C. At higher temperature, Cole-Cole plots are fitted better with the two R-CPE equivalent circuits. The origin of the third element in Mn-doped BaTiO₃ is not clear yet, however, a possibility is an additional contribution of oxygen vacancy at this temperature range. At low-temperature below 350 °C, oxygen vacancies may be frozen-in, while they are mobile with increasing temperature, and contribute to the AC impedance. This is probably why the high-temperature relative permittivity values do not follow Curie-Weiss law as shown in Figure 4.4(d), meaning that the motion of oxygen vacancy may increase the relative permittivity in bulk.

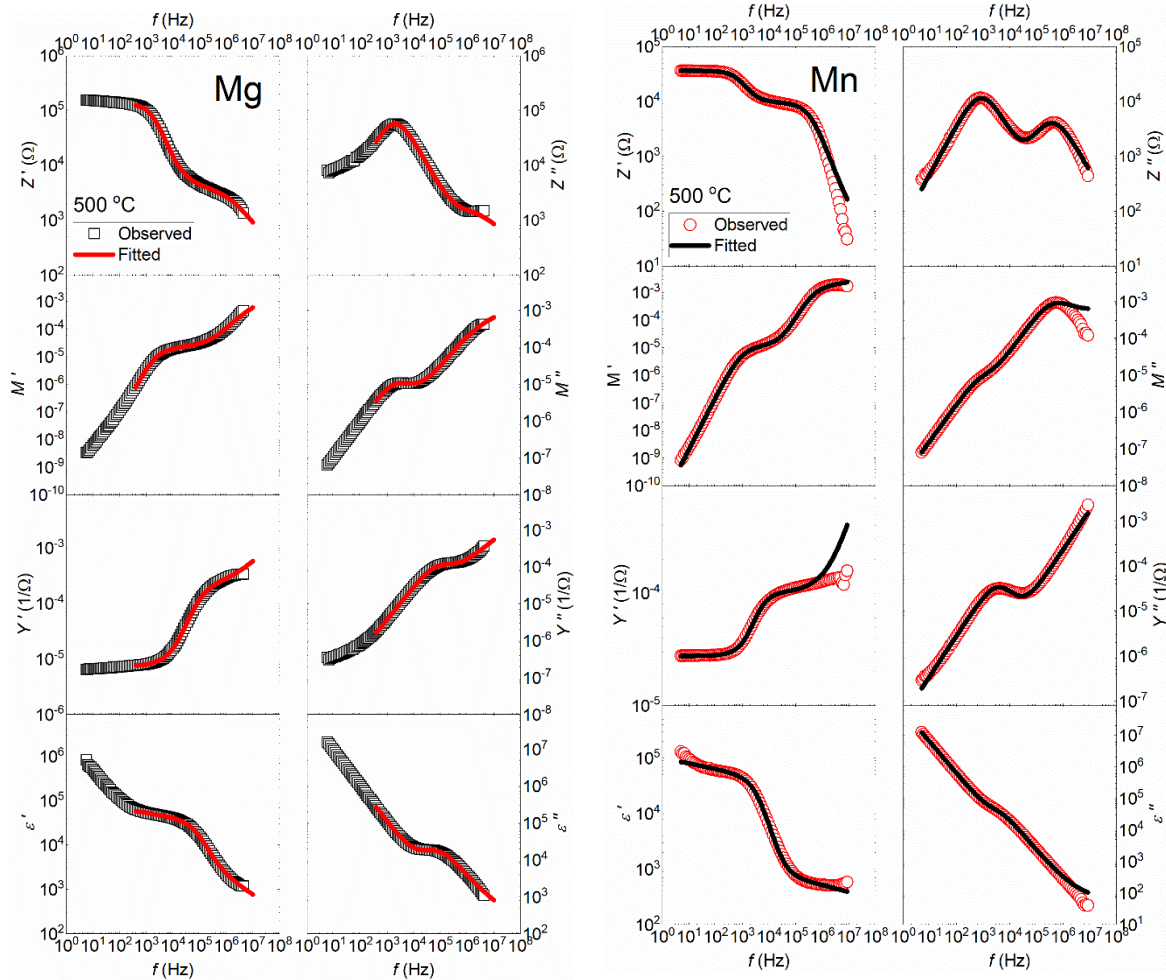


Figure 4.6 Observed and simulated AC formalisms of (a) Mg-doped BaTiO₃ and (b) Mn-doped BaTiO₃ at 500 °C.

From the AC impedance fitting, electrical conductivity of bulk and grain-boundary were obtained as a function of temperature, and they are compared to DC electrical conductivity as shown in Figure 4.7. In Mg-doped BaTiO₃, the magnitude of grain-boundary conductivity is higher than that of the grain conductivity, and the total AC conductivity is mostly controlled by grain-boundary conductivity over a wide range of temperature. On the other hand, the total AC conductivity of Mn-doped BaTiO₃ is determined by 73% of grain-boundary conductivity and 27% of grain conductivity at 500 °C, and with increasing temperature, the AC total conductivity becomes to be predominantly limited by the bulk conductivity. The magnitude of bulk conductivity of Mn-doped BaTiO₃ is almost one order lower than that of Mg-doped BaTiO₃ at 500 °C. With increasing temperature, the grain boundary conductivity increased significantly compared to the bulk conductivity, and the total AC conductivity at 900 °C is governed by the bulk conductivity in both compositions. This indicates that the high-temperature (900 °C) and low-temperature (500 °C) four-point-probe DC conductivities versus pO_2 are mainly limited by the bulk conductivity and the grain-boundary conductivity, respectively with Mg or Mn doping.

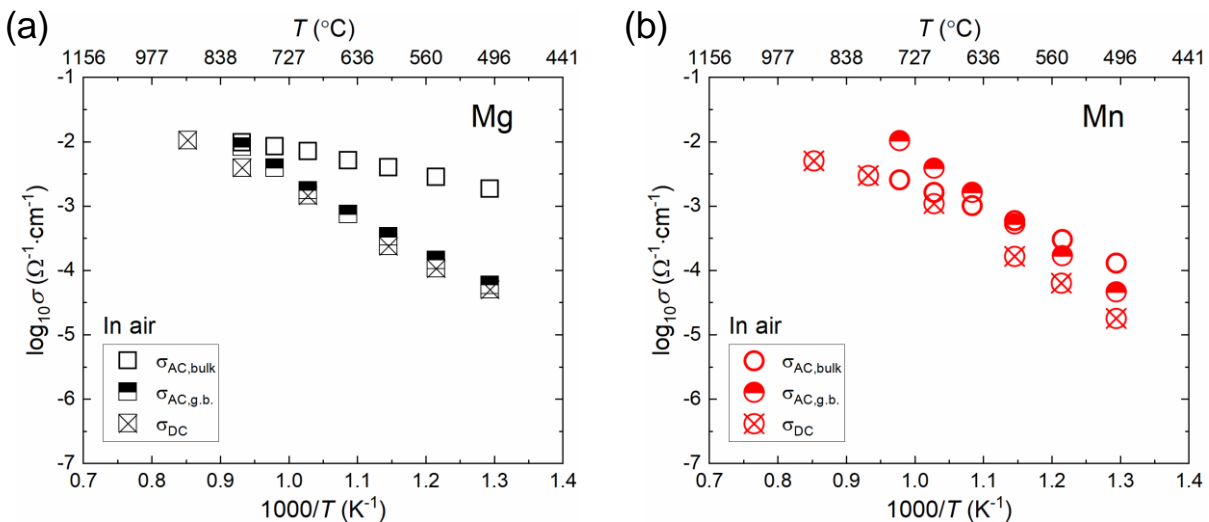


Figure 4.7 Temperature-dependent DC and AC electrical conductivities of (a) Mg-doped BaTiO₃ and (b) Mn-doped BaTiO₃ in air.

Activation energy of DC, bulk, and grain-boundary conductivity is summarized in Table 4.1. The activation energy of bulk conductivity in Mg-doped BaTiO₃ is relatively low, 0.40(3) eV, compared to Mn-doped BaTiO₃, 0.84(2) eV. The 0.40 eV of activation energy is agreed to that of 1 mol% Mg-doped BaTiO₃ at low-temperature range of 143 °C ~ 315 °C.[87] It is worth noting

that the activation energy of bulk conductivity in acceptor-doped BaTiO₃ changes depending on temperature range, and this will be further discussed in Chapter 7. Activation energy of grain-boundary conductivity is 1.18(3) eV, and again well agreed to the prior work.[87] In Mn-doped BaTiO₃, activation energies of bulk and grain-boundary are respectively 0.84(2) eV and 1.47(1) eV agreed to the prior work.[88]

Table 4.1. Activation energy of electrical conduction in Mg or Mn-doped BaTiO₃.

	Activation energy (eV)	
	Mg-doped BaTiO ₃	Mn-doped BaTiO ₃
DC conductivity	1.08±0.03	0.76±0.08 (500 °C ~ 650 °C)
		1.33±0.02 (650 °C ~ 750 °C)
Bulk conductivity	0.40±0.03	0.84±0.02
Grain-boundary conductivity	1.18±0.03	1.47±0.01

The low activation energy of bulk and grain-boundary electrical conductivity of Mg-doped BaTiO₃ is probably due to the low ionization energy of Mg. On the other hand, the ionization level of Mn in BaTiO₃ is expected to be deeper than that of Mg. In addition, the multivalent nature of Mn may enable to capture more electronic charge carriers by changing the charge state of Mn from tetravalent, trivalent, and divalent. Thus, multivalent Mn may behave as a more effective acceptor to trap electronic charge carriers than Mg.

It is also worth noting that the magnitude of activation energies of grain-boundary and grain conductivity show a significant difference in both compositions. At low-temperatures, the grain-boundary with the higher activation energy plays a more significant role than the bulk conductivity in the total electrical conductivity. The phenomena are probably related to segregation or depletion of dopants at the grain-boundary, which can change local defect chemistry.

4.3. Conclusions

In this chapter, the comprehensive DC and AC measurements were made as a function of oxygen partial pressure and temperature to figure out the role of 0.5 mol% Mg and 0.5 mol% Mn on the electrical conductivity of BaTiO₃ ceramics synthesized via a solid-state reaction method. The high (900 °C) and low (500 °C) temperature DC electrical conductivities versus pO_2 revealed that both compositions exhibit *p*-type electrical conductivity in high pO_2 regime. The origin of *p*-type conduction in Mg-doped BaTiO₃ is attributed to the oxidation reaction, while the combined defect reactions involving the ionization of Mn, reduction reaction, and internal equilibrium explained *p*-type behavior in Mn-doped BaTiO₃. It was confirmed from the AC impedance analyses that the high-frequency and low-frequency arcs in Cole-Cole plots are attributed to the bulk and grain-boundary responses, respectively, in both compositions. In addition, the DC electrical conductivity is mainly dominated by the grain-boundary conductivity at 500 °C but by the bulk conductivity at 900 °C. The magnitude of bulk conductivity in Mg-doped BaTiO₃ is higher than that of Mn-doped BaTiO₃, which is due to the low activation energy with Mg-doping.

Chapter 5

Co-doping Strategies for Controlling Electrical Conductivity of BaTiO₃

(Submitted in Journal of the American Ceramic Society. Modifications were made to incorporate it into the dissertation as a whole.)

5.1. Abstract

We explore the synergistic effects of co-doping BaTiO₃ with a judicious combination of acceptors and donors to control the point defect chemistry and electrical properties, with the goal of simultaneously limiting the electronic and ionic conductivities over broad temperature and oxygen partial pressure (pO_2) ranges. Specifically, we compare the temperature- and pO_2 -dependent electrical properties of BaTiO₃ ceramics acceptor-doped with either Mn or Mg and co-doped with Y, which serves as a donor. This paper, which is the first of a two-part series, presents the electrical properties as a function of pO_2 , temperature, and time. The DC and AC electrical conductivity measurements reveal that co-doping with Mn and Y can result in (1) improved electrical resistivity over a broad temperature range, (2) pO_2 -independent electrical conductivity in oxidizing conditions, and (3) improved dielectric degradation resistance as a function of time. The predicted defect concentration with the canonical defect models explains the pO_2 -independent electrical conductivity with the nature of multivalent characteristics of Mn, and the enhanced degradation resistance is attributed to the reduced oxygen vacancy concentration.

5.1. Introduction

Understanding the fundamentals of defect chemistry in oxide materials is vital to rational design of dielectric material properties. The coupled intrinsic and extrinsic lattice and electronic defects not only determine the initial electrical conduction properties, but they ultimately control the time-dependent resistance degradation.[18–20, 89] The design and control of defect chemistry becomes even more critical as capacitors must operate at higher electric fields and temperatures. Thus, refining our fundamental understanding of defect chemistry in important dielectric materials such as BaTiO₃ remains an outstanding challenge to the community.

Several works have studied the role of single-valent Mg and multivalent Mn acceptors on the degradation resistance of ceramic BaTiO₃. [48, 59] Mn was shown to mitigate resistance degradation more effectively than Mg by leading to a greater reduction in the concentration of free oxygen vacancies at the same acceptor concentration. In addition, Mn is thought to trap more electronic charge carriers than Mg by virtue of its multivalent character.[48] Although the Mn doping strategies seem to improve the degradation resistance by limiting both electronic and ionic conductivities, the concentration of free oxygen vacancies is still large enough to make time-dependent degradation in Mn singly doped BaTiO₃ as observed in our present study.

Compositional design approaches have been widely investigated in BaTiO₃ with co-doping of rare-earth elements and acceptors to improve the time-dependent degradation resistance further.[14, 75, 90] This is particularly important for improving the reliability of multi-layer ceramic capacitors (MLCCs), which have been chemically engineered with amphoteric dopants such as Ho, Dy, Er dopants that can occupy both cation sites in X7R and Y5V types BaTiO₃ MLCCs.[14] Han et al. studied the effects of co-doping BaTiO₃ with Mn and Dy or Ho on the time-dependent degradation properties. The co-doped compositions exhibited the stable and low leakage current densities as a function of time compared to the singly doped specimens at 150 °C under 0.5 MV/cm electric field.[90] Improved degradation characteristics in Dy and Mn co-doped BaTiO₃ were also reported by Yoon et al. who showed the better degradation resistance versus time and the higher breakdown voltage with more Dy.[75]

Although co-doping strategies have been experimentally shown to enhance the degradation resistance, the origin of the improvement is not well understood in terms of defect chemistry. In addition, there are only a few works investigating the equilibrium defect chemistry of co-doped

compositions.[62–64] In the prior work of Yeoh et al., the high-temperature electrical conductivity of Mn and Y co-doped BaTiO₃ was shown to be invariant as a function of oxygen partial pressure, pO_2 , with a lower magnitude of conductivity in the high pO_2 range than the singly acceptor-doped compositions.[64]. This behavior was explained by pinning the Fermi level via donor-acceptor mutual compensation, which is a strategy widely used in semi-conducting materials such as GaAs,[1] but arguably much more difficult to implement in most oxide ceramics because of the pervasive background impurities in most commercial-grade materials and the multitude of intrinsic defects, all of which contribute to the charge balance.[32]

To further explore co-doping strategies, in this work we compare the electrical conductivity properties of BaTiO₃ doped with a single-valent (Mg) or multivalent (Mn) cation and with Y as a co-dopant. In this chapter, we measure the temperature-dependent properties of this series of compositions and explore the effects of the Ba:Ti ratio. Both high- and low- temperature DC conductivity measurements are made as a function of pO_2 , and bulk conductivities extracted from AC impedance measurements are compared over a wide range of temperatures in air. In addition, we measure the time-dependent leakage current to understand the effects of the doping chemistries on the degradation kinetics. Canonical defect models are utilized to predict the defect chemistries of Mn and Y co-doped composition to explain the improved electrical resistivity and degradation resistance.

5.2. Experimental setup

A conventional solid-state reaction method was used to make the compositions listed in Table 6.1 using commercial powders of BaTiO₃ (99.995%, Sigma Aldrich), TiO₂ (99.998%, CERAC TM Incorporated), MgO (99.99%, Sigma Aldrich), MnO₂ (99.99%, Sigma Aldrich) and Y₂O₃ (99.99%, Sigma Aldrich). Considering the amphoteric behavior of Y, a small amount of TiO₂ (0.1 mol%) was added to produce A-site vacancies, and thus increased a probability that Y occupies the A-site.[91] For the co-doped compositions, 1.0 mol% Ti-rich compositions were additionally prepared to examine the effects of cation nonstoichiometry on high temperature electrical conductivity.

Table 5.1 Doping levels and molar ratio of BaTiO₃.

Dopant (mol%)			Ti-excess (mol%)	Molar ratio	Abbreviation
Mg	Mn	Y			
0.5	-	-	0.1	BaTiO ₃ :TiO ₂ :MgO=1:0.001:0.005	Mg
-	0.5	-	0.1	BaTiO ₃ :TiO ₂ :MnO ₂ =1:0.001:0.005	Mn
0.5	-	1.0	0.1	BaTiO ₃ :TiO ₂ :MgO:YO _{1.5} =1:0.001:0.005:0.010	Mg+Y
0.5	-	1.0	1.0	BaTiO ₃ :TiO ₂ :MgO:YO _{1.5} =1:0.010:0.005:0.010	
-	0.5	0.5	0.1	BaTiO ₃ :TiO ₂ :MnO ₂ :YO _{1.5} =1:0.001:0.005:0.005	Mn+Y
-	0.5	0.5	1.0	BaTiO ₃ :TiO ₂ :MnO ₂ :YO _{1.5} =1:0.010:0.005:0.005	

The raw powders were wet-milled for 2 h with YSZ balls in anhydrous ethanol. After ball-milling, the powders were calcined at 950 °C for 10 h in air. Pellets 20 mm in diameter and ~3 mm in thickness were compacted by uniaxial pressing at 45 MPa. Sintering was carried out at 1350 °C for 5 h in air, and during this process the sample was positioned on a Pt foil to prevent any contamination. The sintered pellets exhibited a single perovskite phase in all samples. The relative density measured by Archimedes method were 91 ~ 94% and their grain size was around 13 μm, 22 μm, 7 μm, and 16 μm in 0.5 mol% Mg-doped, 0.5 mol% Mn-doped, 0.5 mol% Mg and 1 mol% Y co-doped and 0.5 mol% Mn and 0.5 mol% Y co-doped BaTiO₃, respectively. The sintered pellets were cut and polished to form a rectangular bar shape having 0.02–0.04 cm² in area and 1.5 cm in length for four-point-probe DC measurements. In addition, thin rectangular shape having 0.1–0.26 cm² in area and 0.06–0.1 cm in thickness for AC impedance measurements. Dense Pt electrodes were deposited on sample surfaces using a DC sputtering system. The electrode samples were subsequently annealed at 850 °C in air for 30 min to achieve a better electrical contact.

The electrical conductivity as a function of oxygen partial pressure (pO_2) was measured at 900 °C and then 500 °C using a four-point-probe method. The pO_2 was controlled from 0.21 atm (air) to 10⁻⁴ atm (Ar atmosphere) by varying the flow rate of Ar and O₂ gas and the actual pO_2 was measured with a zirconia oxygen sensor (Ceramic Oxide Fabricators, Australia). As soon as the pO_2 was changed at a given temperature, a small current between 700 μA to 10 μA was applied to the sample and the time-dependent 4-wire resistance was continuously monitored with a multimeter (Keithley 2000, Agilent). Once the resistance was stable as a function of time, the sample was assumed to be thermally and chemically equilibrated. Temperature-dependent electrical properties in air were characterized by analyzing the frequency-dependent AC impedance. Impedance measurements were conducted from 500 °C to 900 °C with a 0.5 V

oscillation level using a HP4192A (Agilent) impedance analyzer over a frequency range from 5 Hz - 5 MHz.

5.3. Results

Figure 5.1(a) shows the DC electrical conductivity of doped BaTiO₃ as a function of pO_2 from air to 10^{-4} atm at 900 °C. In high pO_2 range between 0.21 atm (air) and 10^{-3} atm, the electrical conductivities of all samples reached equilibrium in approximately 1 ~ 2 hours after a decrease in pO_2 of one decade. Thus, the samples were assumed to be in partial equilibrium where defects on the cation sublattices were frozen-in,[82–84] while the oxygen vacancies fully equilibrated at each pO_2 . At the lowest pO_2 , 10^{-4} atm, all compositions showed increased equilibration time, i.e. ~14 hours with Mg or (Mg+Y) co-doping, and ~5 hours in Mn or (Mn+Y) co-doping. It is important to note that after the equilibration at 10^{-4} atm of pO_2 , the samples were subsequently re-equilibrated in air, and the electrical conductivities returned to their initial values within 0.15%, giving confidence that the samples are chemically recovered to the initial state.

As shown in Figure 5.1(a), the high-temperature electrical conductivities of Mg-doped and Mn-doped BaTiO₃ exhibit either a 1/4 or 1/6 slope in $\log_{10}\sigma$ versus $\log_{10}pO_2$. This behavior is consistent with p -type electronic conduction expected from acceptor-doped compositions in high pO_2 ranges.[40, 43, 55, 57] As well described in the prior work, the origin of the p -type conduction is attributed to the oxidation reaction in Mg-doped BaTiO₃,[55] on the other hand, the ionization reaction between tetravalent and trivalent Mn explains the p -type phenomenon in multi-valent Mn-doped BaTiO₃. [43, 46, 57]

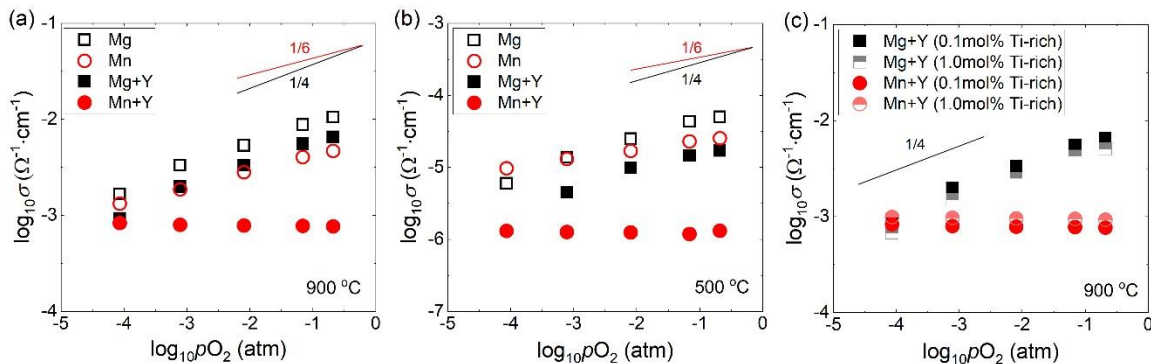


Figure 5.1 DC electrical conductivity as a function of oxygen partial pressure in doped BaTiO₃ with 0.1 mol% Ti-rich at (a) 900 °C and (b) 500 °C. (c) The comparison of high-temperature DC electrical conductivity with respect to the amount of Ti-excess.

Similar to Mg-doped BaTiO₃, (Mg+Y) co-doped samples exhibit *p*-type conduction but with a lower magnitude of electrical conductivity, as seen in Figure 5.1(a). In principle, adding donor dopants should compensate for the acceptors and lower the overall electronic conductivity, which agrees with the trends in the experimental results. In the oxidation reaction, the hole concentration is a function of oxygen partial pressure with a 1/4 exponent and a magnitude of hole concentration is proportional to the concentration of oxygen vacancies.[80]. In Mg singly doped BaTiO₃, the concentration of oxygen vacancy is fixed by a concentration of Mg in high and intermediate *p*O₂ regime at a given temperature. When Mg is co-doped with Y, Y and the oxygen vacancy are both electrically positive species that compensate Mg. Therefore, the system prefers to have less oxygen vacancies energetically than Mg-single doping. Assuming the equilibrium constant for the oxidation reaction is the same in both Mg and (Mg+Y) doping at 900 °C, the magnitude of *p*O₂-dependent electrical conductivity is decreased by the lowered oxygen vacancies in (Mg+Y) co-doped BaTiO₃ in a given same *p*O₂ range.

In stark contrast to (Mg+Y) co-doped BaTiO₃, the electrical conductivity of (Mn+Y) co-doped BaTiO₃ is significantly lower and nearly independent of *p*O₂, which agrees well with the prior work[63, 64] and is attributed to the multivalent nature of the Mn cation.[64] The magnitude of electrical conductivity shows only a 1.15% difference over the measured *p*O₂ range.

At a lower temperature of 500 °C, as shown in Figure 5.1(b), the Mg-doped, (Mg+Y) co-doped, and Mn-doped samples continue to exhibit *p*-type conductivity, as evidence by the positive *p*O₂-dependent DC conductivity. In these samples, the equilibration time was ~ 10 hours during the four-point-probe DC electrical measurements with a decrease in *p*O₂ of one decade. The slow kinetics at a lower temperature is due to the slow process of oxygen exchange in the oxidation reaction. In case of (Mn+Y) co-doping, the DC electrical conductivity is lowest over the entire *p*O₂ range at this temperature. Most interestingly, the electrical conductivity of the (Mn+Y) co-doped samples did not change within the measurement precision as a function of time and *p*O₂ for up to 2 hours.

The effect of cation nonstoichiometry on the high-temperature DC electrical conductivity was examined as a function of *p*O₂ in (Mg+Y) and (Mn+Y) co-doped BaTiO₃ as shown in Figure 5.1(c). Although there is a 3 ~ 5% difference in the magnitude of log₁₀σ in all *p*O₂, the overall behavior of electrical conductivity versus *p*O₂ is almost the same in both co-doped BaTiO₃

regardless of Ti-excess. The relaxation processes in the 1 mol% Ti-rich compositions are as fast as that in the 0.1 mol% Ti-rich compositions.

We further explored the temperature-dependent AC impedance characteristics of the samples at a pO_2 of 0.21 atm (air) to understand the electrical conduction mechanisms. Figure 5.2 shows the frequency-dependent imaginary versus real part of the impedance, or Cole-Cole plots, of each sample at 500 °C. Mainly, two semi-circles are observed in all compositions. A third element at very low-frequency is seen in Mg-doped and (Mg+Y) co-doped BaTiO₃ that is seemingly related to interface effects. With increasing temperature (data not shown), the resistances of the low-frequency range elements decrease significantly with Mg or Mn single doping and (Mg+Y) co-doping, while the contribution of the high-frequency response to the total impedance becomes greater with increasing temperature. Compared to other compositions, the

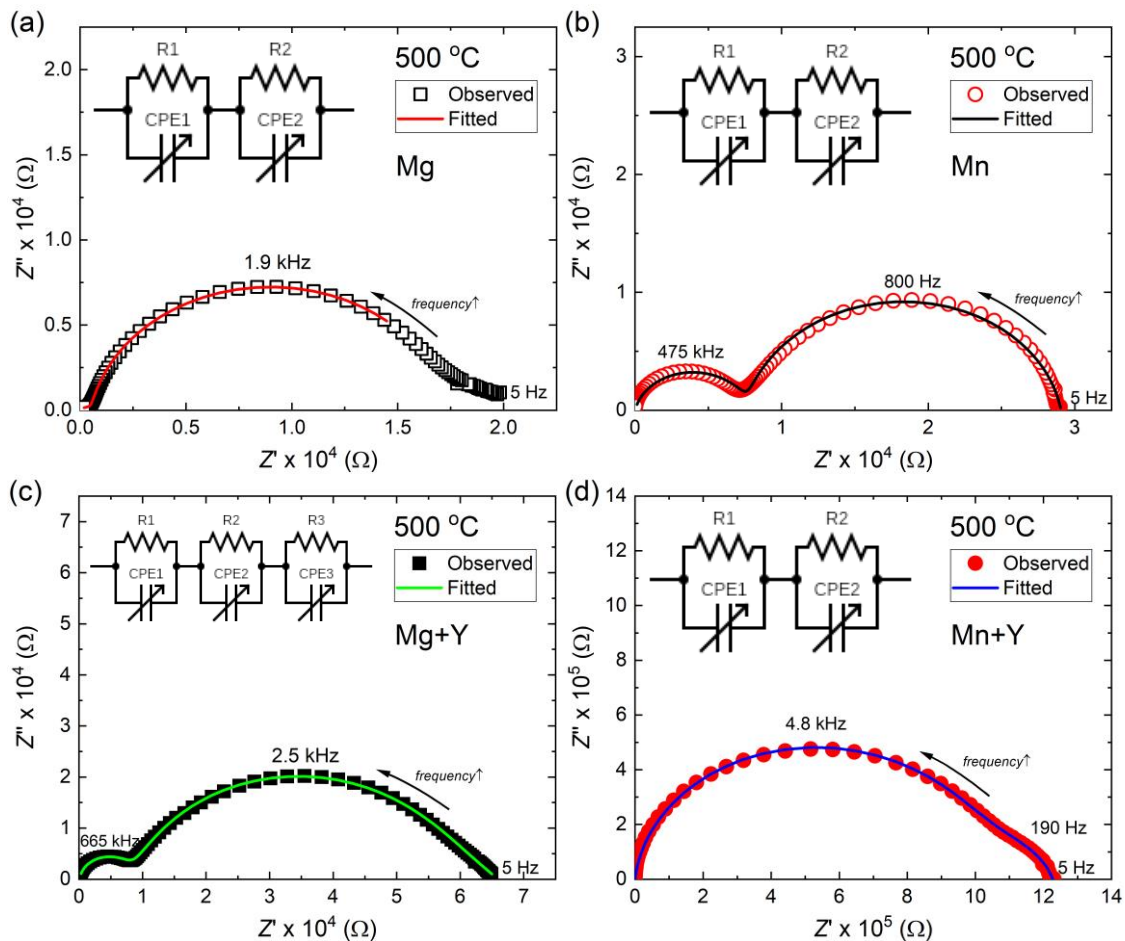


Figure 5.2 Observed and fitted Cole-Cole plots of (a) Mg-doped (b) Mn-doped (c) (Mg+Y) co-doped and (d) (Mn+Y) co-doped BaTiO₃ at 500 °C in air. Note that the real and imaginary parts of impedance were scaled by the sample geometry for the direct comparison of impedance magnitudes.

total impedance of (Mn+Y) co-doped BaTiO₃ is dominated by the high-frequency element over the entire temperature range, from 500 °C – 800 °C.

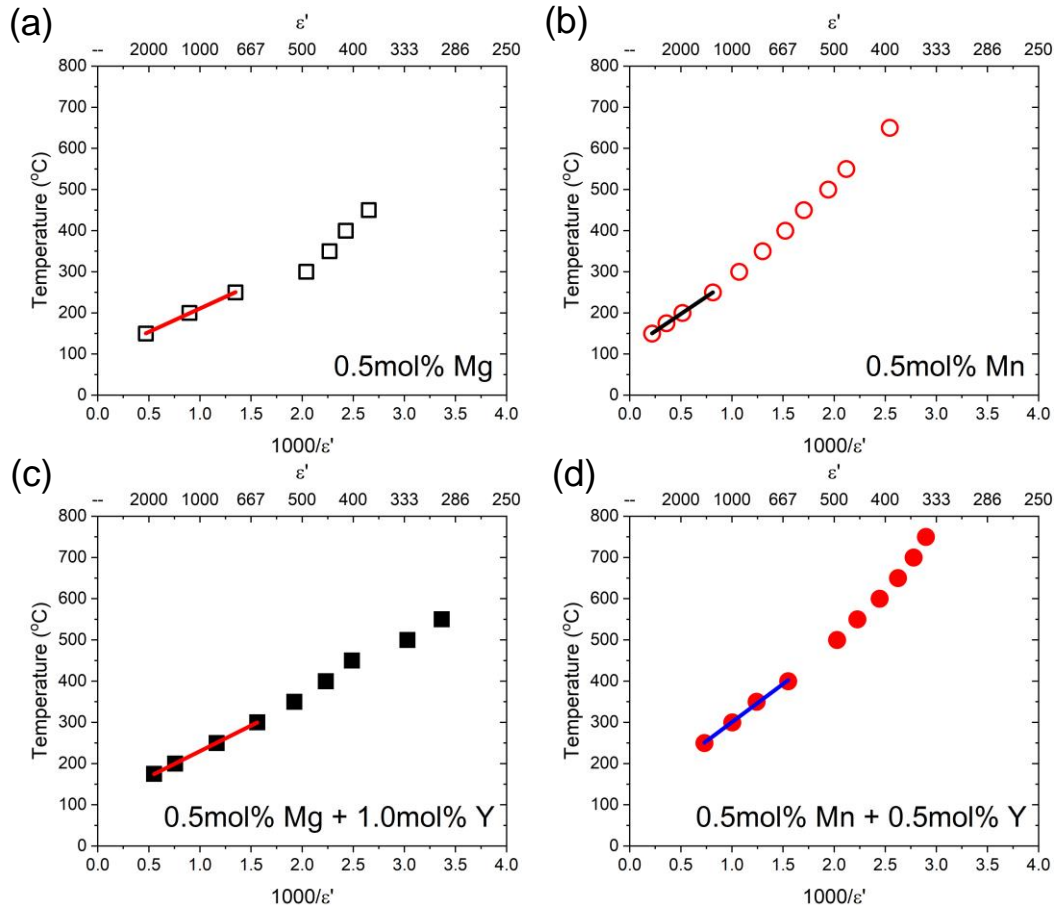


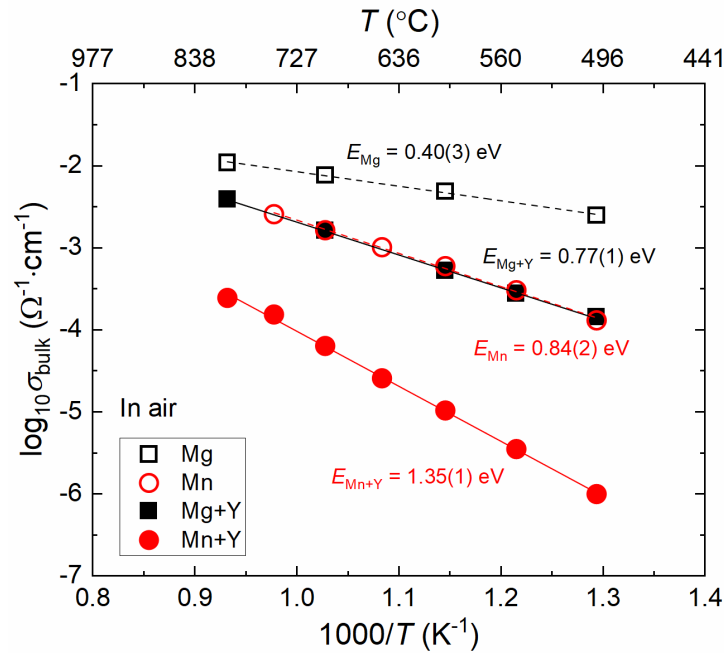
Figure 5.3 Curie-Weiss law fitting in (a) Mg-doped (b) Mn-doped (c) (Mg+Y) co-doped and (d) (Mn+Y) co-doped BaTiO₃.

The frequency-dependent capacitances were more closely investigated to clarify the origins of the high and low-frequency responses. In all samples, the high-frequency capacitance plateau is on the order of 10^{-11} F, which translates into relative permittivity values of 400 ~ 600 depending on the composition. These are reasonable values for BaTiO₃ at this temperature,[86] and strongly suggests that the high-frequency arc is associated with the bulk grain response. In addition, the temperature-dependent permittivity was analyzed with respect to Curie-Weiss behavior. A transition temperature around 97 °C ~ 115 °C and a Curie constant of 110000 °C ~ 180000 °C are confirmed in all compositions in Table 5.2, which are, again, all reasonable values for bulk BaTiO₃. [61]

Table 5.2 Curie temperature and constant in doped BaTiO₃.

Composition	Curie temperature (°C)	Curie constant (°C)
Mg	96.8±0.2	114007±1861
Mn	114.0±0.9	167209±1766
Mg+Y	106.3±0.8	123901±728
Mn+Y	115±7	185078±6459

On the other hand, the capacitances corresponding to the low-frequency semi-circle are on the order of 10⁻⁹ F, and they are nearly temperature independent. Based on these observations, we attribute the high-frequency and low-frequency elements to the grain and grain boundary responses, respectively.[61, 85, 86] Each impedance spectrum is fitted to an equivalent circuit-element model to obtain the temperature-dependent bulk electrical conductivity and the selected equivalent circuits are shown as insets in Figure 5.2.

**Figure 5.4** Temperature-dependent bulk conductivities, extracted from impedance spectra, and activation energies in air.

While the grain boundary behavior is certainly important to the overall conductivity,[86] the present analysis focuses on the bulk defect chemistry and conductivity behavior. Arrhenius plots of the high-frequency bulk electrical conductivities are summarized in Figure 5.4. Mg-doped

BaTiO₃ is most conductive among the compositions and its activation energy is lowest (0.40 ± 0.03 eV) at this temperature range in air. The bulk conductivity of Mn-doped BaTiO₃ is almost one order of magnitude lower than that of Mg-doped BaTiO₃ and a higher activation energy (0.84 ± 0.02 eV) is observed. As expected, Y co-doping in Mg-doped BaTiO₃ reduces the magnitude of bulk electrical conductivity due to the donor and acceptor mutual compensation. The effectiveness of co-doping is most pronounced in the (Mn+Y) co-doped BaTiO₃, however with decreasing temperature, the bulk conductivity reduces significantly and is accompanied by a high activation energy of 1.35 ± 0.01 eV. As a consequence, the bulk conductivity of the (Mn+Y) sample is almost two orders of magnitude lower than (Mg+Y) co-doping at the lowest measurement temperature of 500 °C.

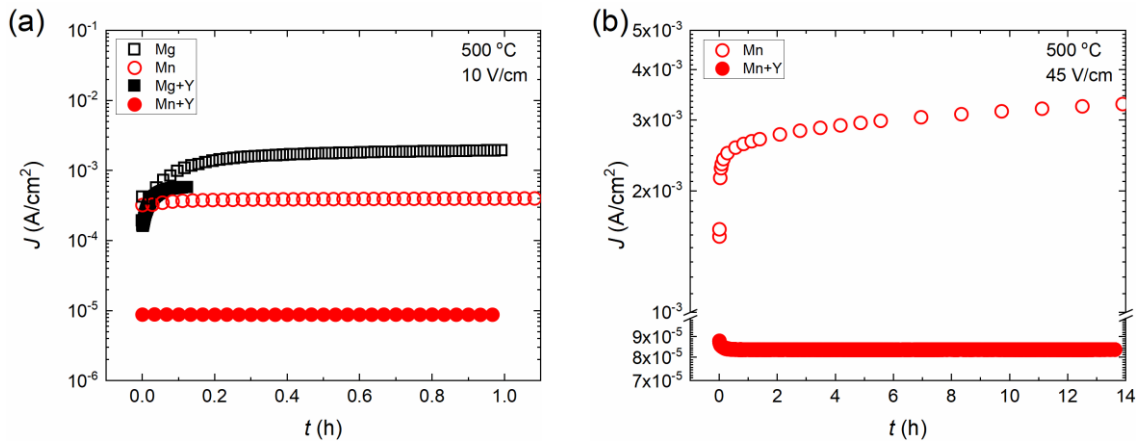


Figure 5.5 Time-dependent current density at 500 °C under (a) 10 V/cm and (b) 45 V/cm DC electric field.

While the co-doping effects are very effective in reducing the electronic conductivity of the samples, equally important is the effect of doping on the oxygen vacancy concentrations, because mobile oxygen vacancies, even in predominantly electronic conductors, can lead to the time-dependent dielectric degradation in many perovskite materials.[15] Figure 5.5 shows the current density versus time at 500 °C under a 10 V/cm DC electric field. As a function of time, the current density of Mg-doped sample increases significantly, almost 5 times higher than the initial value and it stabilizes within 2 hours at a given condition. The degradation process in Mn-doped BaTiO₃ is relatively slow, which is in agreement with the prior result,[48] and the current density continuously changes even after 10^4 s. (Mg+Y) co-doping improves the degradation resistance

relative to the single Mg-doping. The current density saturates faster and is less than Mg-doping, however, the behavior is still time-dependent. Interestingly, co-doping of Y and Mn improves the degradation resistance significantly. The current density is low and constant with time. With a higher DC biasing field of 45 V/cm, as shown in Figure 5.5(b), the degradation of the singly doped Mn sample is accelerated. On the other hand, the current density of the (Mn+Y) co-doped BaTiO₃ is very stable and never increases up to 14 hours in these highly accelerated conditions. This suggests that the oxygen vacancy concentration in (Mn+Y) co-doped is significantly lower than other compositions.

5.4. Discussion

Obviously, co-doping with Y and Mn profoundly improved the semi-insulating electrical properties and time-dependent degradation of BaTiO₃ ceramics over a wide range of pO_2 , temperature and time. To understand the origin of this remarkable improvement in resistance degradation, we evaluate the equilibrium and partially equilibrated quenched defect chemistry based on established canonical defect chemistry models. The possible defect reactions in this system are summarized in Table 5.3 with their mass action law and equilibrium constants (K) expressed as a Kröger-Vink notation. The equilibrium defect concentrations as a function of pO_2 at an equilibrium temperature (T_E) were obtained by solving the charge neutrality condition,

$$[M_{Ti}] + [A'_C] + 4[V_{Ti}'''] + 2[V_{Ba}'''] + n = p + 2[V_O^\bullet] + [Y_{Ba}^\bullet] \quad (5.1)$$

where $[M_{Ti}]$ is $2[Mg_{Ti}'']$ in (Mg + Y) co-doped BaTiO₃ or $2[Mn_{Ti}''] + [Mn'_{Ti}]$ in (Mn + Y) co-doped BaTiO₃. The low-temperature (T_Q) quenched defect structure was calculated through the Eq. 6.1 under the assumptions that (1) the concentration of cation vacancies are fixed from the high-temperature equilibration ($T_E = 1150$ °C)[52] but those of the electronic carriers and oxygen vacancy are allowed to be fully equilibrated at T_Q , (2) a concentration of background impurity (A'_C) acting as an acceptor was assumed to be $\sim 10^{17}/\text{cm}^3$ (~ 6 ppm) based on the starting BaTiO₃ (99.995%) powders and additional impurities of Y₂O₃ ($1.09 \times 10^{17}/\text{cm}^3$) from the ball milling process were taken into account as a donor, (3) Mg and Mn are assumed to occupy the Ti site exclusively and act as acceptors, while Y is assumed to occupy Ba site and behaves as a donor,

and (4) while all Mg and Y ions are fully ionized at T_q , the Mn ions are allowed to change their charge from neutral to the thermodynamically favorable states.

Table 5.3. Defect reactions and equilibrium constant.

Defect reactions	Mass action law	Equilibrium constant (K)	Ref.
Reduction reaction	$K_{Re} = [V_O^{\bullet}]n^2P_{O_2}^{1/2}$	$1.06 \times 10^{71} \exp\left(-\frac{5.69}{k_B T}\right)$	[49]
Electronic equilibrium	$K_i = np$	$6.8 \times 10^{44} \exp\left(-\frac{2.90}{k_B T}\right)$	
Full Schottky reaction	$K_S = [V_{Ba}^{\prime\prime}][V_{Ti}^{\prime\prime\prime}][V_O^{\bullet}]^3$	$3.4 \times 10^{105} \exp\left(-\frac{2.795}{k_B T}\right)$	
Ionization of Mn	$K_{Mn1} = \frac{[Mn_{Ti}^{\times}]n}{[Mn_{Ti}^{\prime}]}$ $= 2N_C \exp\left(-\frac{E_C - E_{Mn1}}{k_B T}\right)$	$3.2 \times 10^{22} \exp\left(-\frac{1.72}{k_B T}\right)$	[46]
	$K_{Mn2} = \frac{[Mn_{Ti}^{\prime}]n}{[Mn_{Ti}^{\prime\prime}]}$ $= 1/2N_C \exp\left(-\frac{E_C - E_{Mn2}}{k_B T}\right)$	$0.8 \times 10^{22} \exp\left(-\frac{1.12}{k_B T}\right)$	

Figure 5.6 shows the partial equilibrium defect structure of Mg-doped BaTiO₃ with various number of Y at 900 °C. As shown in Figure 5.6(a), the oxygen vacancy concentration in Mg singly doped BaTiO₃ is extrinsically fixed to $\sim 10^{20}/\text{cm}^3$ by the acceptors in a wide range of pO_2 except for a high pO_2 range ($pO_2 > 10^0$ atm). With increasing Y-doping, the oxygen vacancies reduce, because the acceptors are compensated by both oxygen vacancies and donors. When the donor and acceptor mutual compensation is achieved ($[Y_{Ba}^{\bullet}]/[Mg_{Ti}^{\prime\prime}] = 2$), the amount of oxygen vacancy decreased by one order of magnitude of the number.

In Figure 5.6(b), the concentration of cation vacancy is explored as a function of doping level. In Mg-singly doped BaTiO₃, the amount of cation vacancy is $\sim 10^{18}/\text{cm}^3$ in the entire pO_2 range, which is less than that in undoped BaTiO₃ ($\sim 10^{19.1}/\text{cm}^3$). As the doping level of Y increases, there is the systemic increase in the cation vacancy concentration to compensate the positively charged

Y_{Ba} extrinsic defects. In the composition with $[Y_{Ba}]/[Mg_{Ti}^{''}] = 2$, the concentration of cation vacancy shows $\sim 10^{19.1} / \text{cm}^3$ which is the same as the one in undoped BaTiO_3 .

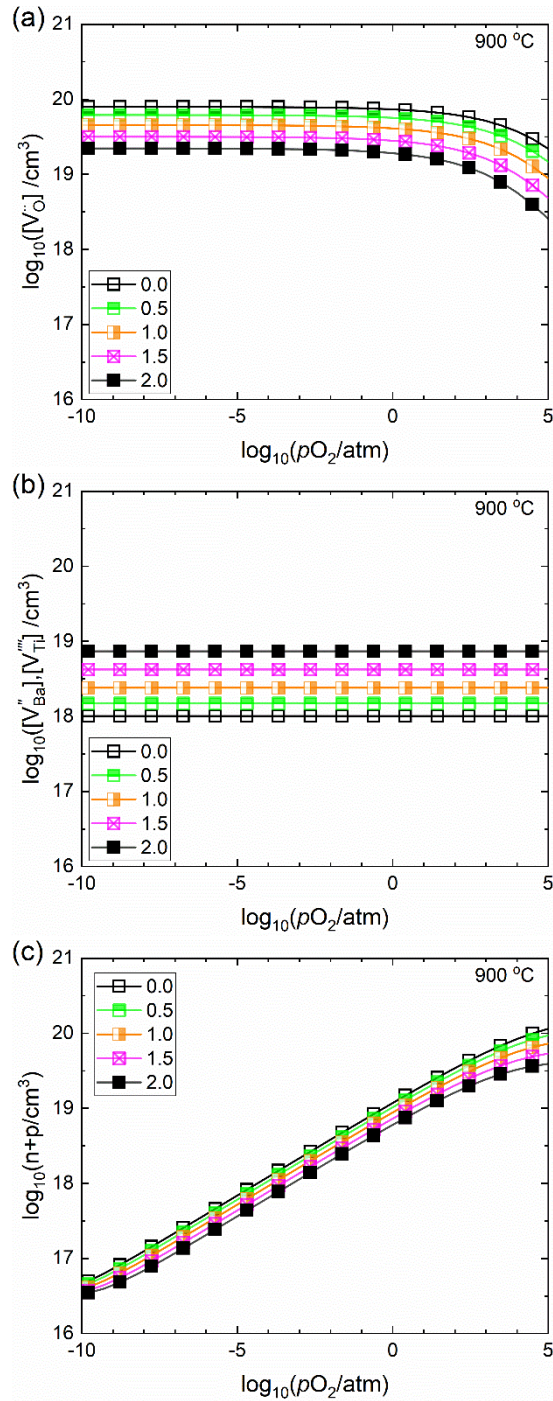


Figure 5.6 Predicted concentration of (a) oxygen vacancy, (b) cation vacancy, and (c) electronic charge carrier at 900 °C in (Mg+Y) co-doped BaTiO_3 with $[Y_{Ba}]/[Mg_{Ti}^{''}] = 0, 0.5, 1.0, 1.5,$ and 2.0 .

The predicted electronic carrier concentration expressed as the summation of n and p is observed in Figure 5.6(c). Mg singly doped BaTiO₃ ($[Y_{Ba}]/[Mg_{Ti}^{''}] = 0$) shows the positive pO_2 dependence of electronic charge carrier in high pO_2 range, which is agreed to the observed electrical conductivity. With donor doping, there is a systematic shift of n - p transition point to higher pO_2 , again well agreed to the experimental results. When the acceptors are mutually compensated by the donors ($[Y_{Ba}]/[Mg_{Ti}^{''}] = 2$), the concentration of electronic charge carriers is the same as the concentration in undoped BaTiO₃.

The predicted partial equilibrium defect structure in (Mn + Y) co-doped BaTiO₃ is different to (Mg + Y) co-doped BaTiO₃ as shown in Figure 5.7. First of all, the oxygen vacancy concentration in 0.5 mol% Mn singly doped BaTiO₃ is lower than that of 0.5 mol% Mg singly doped BaTiO₃. This is because the number of negatively charged net acceptors is lower in Mn-doped BaTiO₃ than that of Mg-doped BaTiO₃, i.e. $[Mn_{Ti}'] + [Mn_{Ti}^{''}] < [Mg_{Ti}^{''}]$ even though the doping level is both 0.5 mol%. Secondly, there is a variation in the relative concentration of neutral, trivalent, and divalent Mn with respect to the donor doping and the pO_2 change. In Figure 5.7(b), the charge state of Mn is mostly neutral, i.e. $[Mn_{Ti}]_T = [Mn_{Ti}^{\times}] + [Mn_{Ti}'] + [Mn_{Ti}^{''}] \approx [Mn_{Ti}^{\times}]$ in Mn singly doped BaTiO₃. With donor doping, the concentration of trivalent and divalent Mn increases, and is pinned at high- pO_2 range, suggesting that the electron trapping occurs by the Mn center, which leads to the ionization of Mn. This results in the pinning of electron concentration in the high- pO_2 range, which is observed as the pO_2 -independent electrical conductivity.

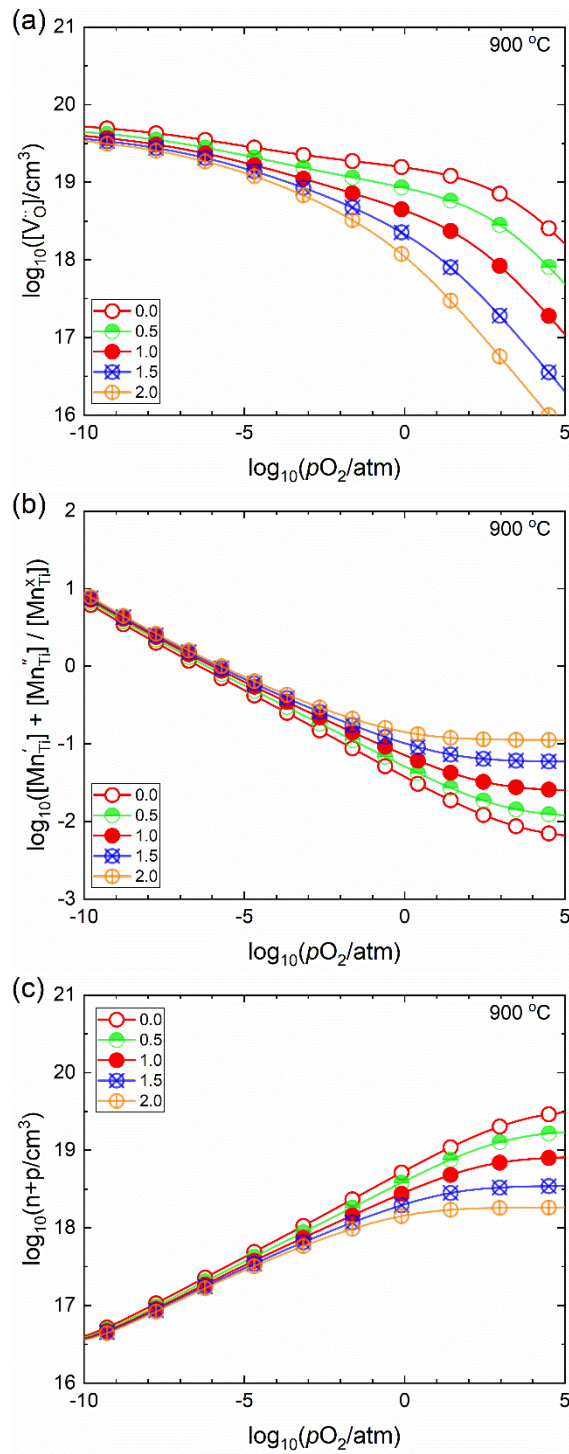


Figure 5.7 Predicted defect concentration of (a) oxygen vacancy, (b) neutral and ionized Mn, and (c) electron and hole in (Mn+Y) co-doped BaTiO₃ with $[Y_{Ba}]/[Mn_{Ti}]_T = 0, 0.5, 1.0, 1.5,$ and 2.0 at $900\text{ }^\circ\text{C}$.

The defect concentrations versus pO_2 in (Mn+Y) co-doped BaTiO₃ at the low-temperature (500 °C) was further examined to understand the pO_2 independence of electrical conductivity and the enhanced degradation resistance as shown in Figure 5.8. In Figure 5.8(a), the oxygen vacancies in (Mn+Y) co-doped BaTiO₃ show a significant decrease as increasing Y concentration at 500 °C, which explains the improved degradation characteristics. Figure 5.8(b) shows the electronic carrier concentration as a function of oxygen partial pressure at 500 °C temperatures. The concentration shows a remarkable decrease and a wide range of pO_2 independence with Mn and Y co-doping. This prediction is well agreed to our experimental results, and the small number of charge carrier seems to be an origin of semi-insulating properties in (Mn+Y) co-doped BaTiO₃.

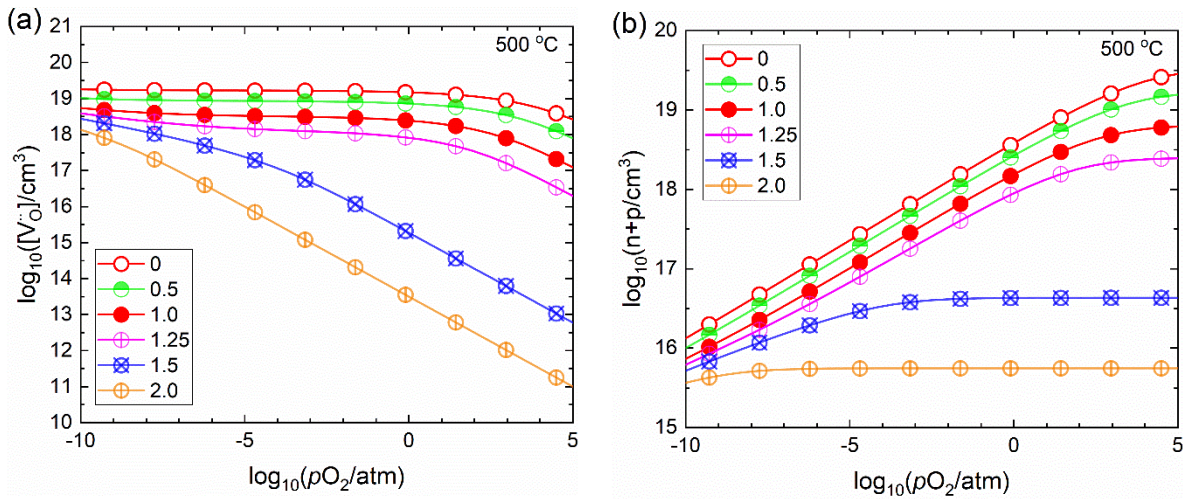


Figure 5.8 Predicted defect concentration of (a) oxygen vacancy and (b) electron and hole in (Mn+Y) co-doped BaTiO₃ with $[Y_{Ba}]/[Mn_{Ti}]_T = 0, 0.5, 1.0, 1.5,$ and 2.0 at $500\text{ }^\circ\text{C}$.

It is worth noting that although the canonical defect models explain the bulk electrical conductivity of BaTiO₃, there are still challenges for developing comprehensive canonical defect models including all doping systems. Particularly, in this works, we found difficulties for predicting defect structures in co-doped BaTiO₃. The partial defect equilibria of (Mg+Y) co-doped BaTiO₃ with higher Y concentration ($[Y]/[Mg] > 2$) where a *n*-type electrical conductivity is expected, showed the very similar defect structure as acceptor-doped BaTiO₃. In addition, in (Mn+Y) co-doped BaTiO₃, the critical composition (Y/Mn) for predicting the wide pO_2 -independent electrical conductivity can be varied significantly by either the equilibrium constants of reduction reaction or electronic equilibrium. The discrepancy between the predictions by the

canonical defect models and the observed electrical conductivity is probably due to the following issues: (1) defect complexes are not considered, and (2) cation dopants substitute either on the A or B cation sublattices, and (3) an under- or overestimated background impurity concentration in the canonical defect chemistry. These issues were realized to be the critical factors determining the electrical conductivity and can be circumvented by density-functional theory (DFT) calculations with grand canonical defect models.[32, 33] In recent DFT simulations by Bowes et al.,[52] the observed electrical conductivity as a function of pO_2 and temperature is well explained with the grand canonical defect models in all $BaTiO_3$ compositions in this dissertation. The Fermi level pinning mechanism in (Mn+Y) co-doped $BaTiO_3$ is attributed to the multivalent nature of Mn, and the improved electrical resistivity and time-dependent degradation characteristics is originated by the reduced oxygen vacancy concentration. In addition, the analyses also emphasize the importance of cation vacancies and the assumed freeze-in temperature of defects on the cation sublattices.

5.5. Conclusions

The impact of donor and acceptor co-doping on the electrical properties of $BaTiO_3$ ceramics was investigated as a function of temperature, oxygen partial pressure and time. The high-temperature (900 °C) four-point-probe DC conductivity in the high pO_2 range revealed that while the Mg or Mn acceptor singly doped and (Mg+Y) co-doped compositions exhibited typical p -type electrical conductivity, co-doping with (Mn+Y) led to pO_2 -independent and significantly lower electrical conductivity. These (Mn+Y) co-doped samples exhibited a relatively high activation energy for bulk electrical conduction of 1.35 eV between 500 °C – 900 °C in air. Moreover, the (Mn+Y) co-doped $BaTiO_3$ specimens exhibit no significant time-dependent electrical degradation at 500 °C and 45 V/cm. The predicted defect concentration with the developed canonical defect model showed that the co-doping of (Mn+Y) in $BaTiO_3$ can pin the concentration of electronic carrier by the ionization of multivalent Mn in the high pO_2 range, explaining the observed pO_2 -independent electrical conductivity.

Chapter 6

Origin of Electrically Semi-Insulating Properties of Fe-doped β -Ga₂O₃

(In preparation, Modifications were made to incorporate it into the dissertation as a whole.)

6.1. Abstract

In this work, we measure the DC and AC conductivity and Hall voltage to determine the origin of electrical insulating properties of Fe-doped β -Ga₂O₃ single crystals perpendicular to the ($\bar{2}01$) crystallographic planes. We find that the electrical conduction is predominantly controlled by free electrons in the temperature range of 230 °C to 800 °C, with the compensation of the impurity donor (Si) and acceptor dopant (Fe) explaining the low concentration of free electron and Fermi level pinning over a wide range of temperature. Moreover, the electrical conductivity is largely oxygen partial pressure (pO_2)-independent from air to 10^{-4} atm at 600 °C but becomes slightly dependent on pO_2 at 800 °C, as intrinsic non-stoichiometric point defects begin to influence the charge balance.

6.2. Introduction

Early studies on the equilibrium electrical conductivity of undoped polycrystalline β -Ga₂O₃ exhibited a strong pO_2 -dependence as shown in Figure 6.1, which is typical for electronically conducting metal oxides. Sasaki[21] and Fleischer[24] showed that the high-temperature electrical conductivity (σ) of unintentionally doped β -Ga₂O₃ ceramics and thin films have oxygen partial

pressure (pO_2) dependence of $\sigma \propto pO_2^{-1/4}$ with an activation energy of 1.85 eV \sim 2.1 eV from 800 °C to 1000 °C. The pO_2 -dependent electrical conductivity was attributed to the singly charged oxygen vacancies and/or doubly ionized gallium interstitials. Also studying unintentionally doped polycrystalline β - Ga_2O_3 , Cojocaru[23] observed that the electrical conductivity was a function of $-1/4.55$ power of pO_2 at 127 °C and became less pO_2 -dependent with increasing temperature. At 727 °C, the $\sigma \propto pO_2^{-1/3.73}$ relation was obtained. The pO_2 -dependence at various temperatures was attributed to the triply charged gallium interstitials.

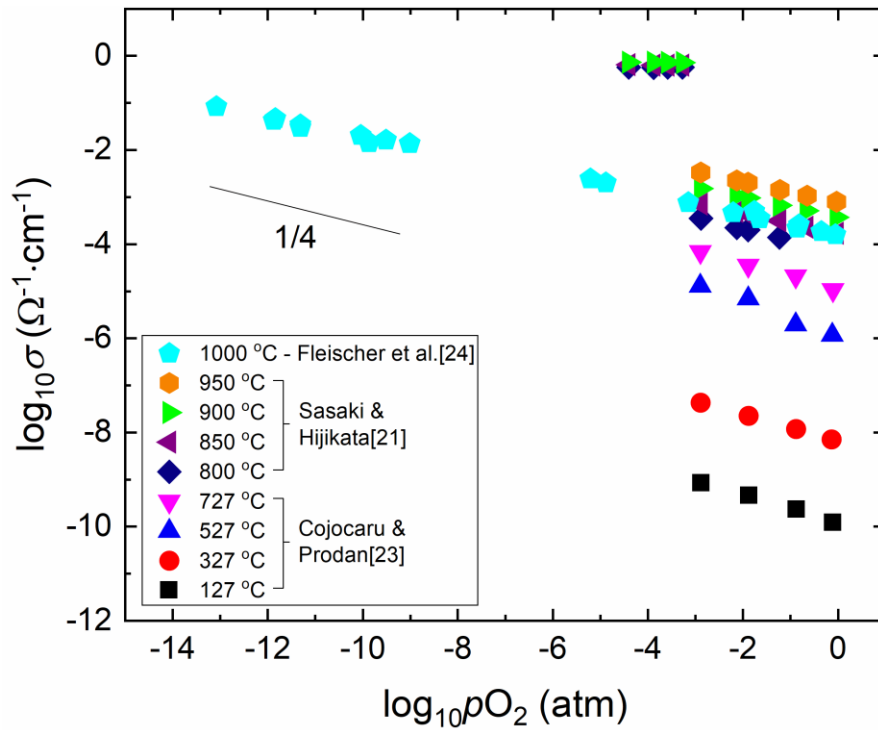


Figure 6.1 Electrical conductivity versus oxygen partial pressure in unintentionally doped β - Ga_2O_3 polycrystalline.

While the early studies in the high-temperature equilibrium conductivity argued that the n -type conductivity of β - Ga_2O_3 could be explained by simplified defect models with the ionized gallium interstitials or the ionized oxygen vacancies, density functional theory (DFT) calculation by Varley et al. maintained that the oxygen vacancies are deep donors and the origin of n -type is attributed to the background impurities such as Si or Sn acting as shallow donors in Ga_2O_3 . [28] Another DFT calculation [5] in undoped β - Ga_2O_3 predicted that the electrical conductivity is pO_2 dependent with a $1/6$ exponent, i.e. $\sigma \propto pO_2^{-1/6}$ due to the doubly ionized oxygen vacancy. In

addition, even a small amount of background donors (10 ppm, or 10^{18} cm^{-3}) can give rise to n -type conductivity and the relation $\sigma \propto p\text{O}_2^{-1/4}$ can be driven by the complex defect compensation mechanism.

While these aforementioned experimental[10, 26, 27] and theoretical[5, 28, 29] studies have explored the electrical conduction mechanism of unintentionally doped and donor doped n -type β - Ga_2O_3 systems, a clear understanding of the electrical conduction mechanism in semi-insulating β - Ga_2O_3 has not been established. Moreover, many challenges for fabricating p -type β - Ga_2O_3 have been addressed by the community,[6, 92] motivating a fundamental study of the β - Ga_2O_3 defect chemistry. In addition, the lattice defect chemistry is also important to understand the potential for electrical degradation phenomenon associated with charged ionic defect migration, which may happen under a high electric field during device operation as often observed in perovskite oxide dielectrics.[18–20, 89]

In this work, we have investigated the origin of the semi-insulating electrical properties of Fe-doped β - Ga_2O_3 single crystals. Four-point-probe DC and AC electrical conductivities were measured over a wide range of temperatures in air. Hall characteristics were obtained to determine the type of carrier, its concentration, and mobility as function of temperature. In addition, the DC electrical conductivity as a function of $p\text{O}_2$ was measured at high-temperatures and discussed in terms of defect chemistry.

6.3. Experimental Procedure

(010) Fe-doped β - Ga_2O_3 single crystals prepared by the edge-defined film-fed growth method (EFG) were purchased from Tamura Corporation (Japan). Prior glow discharge mass spectrometry (GDMS) analysis revealed the unintentional background impurity concentration of Si to be $1 \times 10^{17} \text{ cm}^{-3}$ and the intentionally doped Fe concentration to be $8 \times 10^{17} \text{ cm}^{-3}$. [77] To characterize AC and DC electrical properties along the in-plane crystallographic direction perpendicular to $(\bar{2}01)$, four-linear platinum (Pt) contacts (500 nm in thickness) spaced by 2 mm – 3 mm in length were deposited on the top, bottom and two sides of a specimen having 20 mm (length) \times 10 mm (width) \times 0.5 mm (thickness) using a DC sputtering system. DC electrical conductivity was measured using the linear four-point-probe method. The four-terminal AC impedance technique was used to characterize the frequency dependent electrical properties using

a HP4192A (Agilent) with a frequency range of 5 Hz – 5 MHz and a 0.1 V oscillation level. Oxygen partial pressure (pO_2) was controlled from 1 to 10^{-4} atm by changing the gas flow of O_2 and Ar, and the actual pO_2 was monitored by a zirconia oxygen sensor (Ceramic Oxide Fabricators, Australia). Hall measurements were carried out from 225 °C to 500 °C in N_2 atmosphere using the van der Pauw method with ~200nm Ti electrodes.

6.4. Results and Discussion

Figure 6.2(a) presents the real part (Z') versus imaginary part (Z'') of AC impedance, or Cole-Cole plot, of a Fe-doped β - Ga_2O_3 single crystal as a function of temperature in air measured by four-point-probe method. One slightly dispersed semi-circle was obtained from 500 °C to 700 °C, and a partial semi-circle was observed below 500 °C to 300 °C. At a given temperature, we observed a capacitance plateau with a single response in the imaginary part of modulus as a function of frequency as shown in the inset in Figure 6.2(a). These observations and ohmic behavior in the current-voltage response strongly suggest that the electrical conductivity with the four-point-probe AC method is predominantly governed by bulk conductivity. Cole-Cole plots were fitted by a simple equivalent circuit model having a resistance (R) with a constant phase element (CPE) in parallel. Although the frequency response originates from the homogenous single crystal, a constant phase element (CPE) was used rather than a perfect capacitance (C) due to the instrumental artifacts during the four terminal AC measurement.[93] The electrical conductivity obtained from the Cole-Cole plots shows a positive temperature dependence with 0.85(1) eV activation energy in air as shown in Figure 6.2(b). The temperature-dependent electrical conductivity from the AC fitting is directly compared to the four-point-probe DC electrical conductivity in Figure 6.2(b). The magnitude of electrical conductivity and the activation energies agreed between the different techniques. The activation energies are consistent to the values reported at lower temperatures.[94]

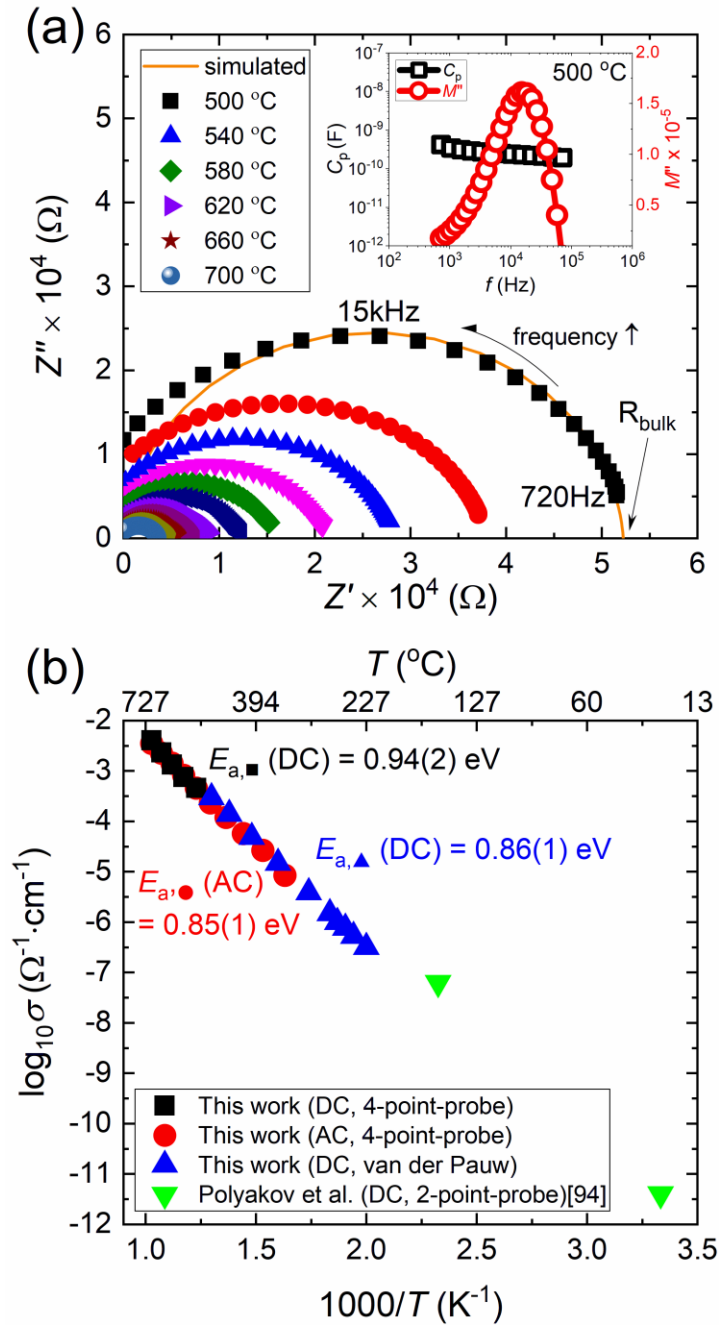


Figure 6.2 (a) Cole-Cole plots versus temperature in air and capacitance and imaginary part of modulus as a function of frequency at 500 °C in inset Figure. (b) Temperature-dependent electrical conductivities obtained from the different techniques.

Low-temperature electrical characteristics were further analyzed by van der Pauw Hall measurements. As shown in Figure 6.3(a), a carrier concentration of $\sim 6 \times 10^{10} / \text{cm}^3$ at 230 °C following an Arrhenius behavior with activation energy of 0.93(1) eV with a negative Hall coefficient was observed, agreeing with prior work.[77] In addition, the Hall mobility shows a negative temperature dependence with a $\sim 1.4(1)$ slope in the $\log_{10}\mu$ versus $\log_{10}T$ plot in Figure 6.3(b), which is the expected behavior for electron-acoustic phonon scattering.[95]

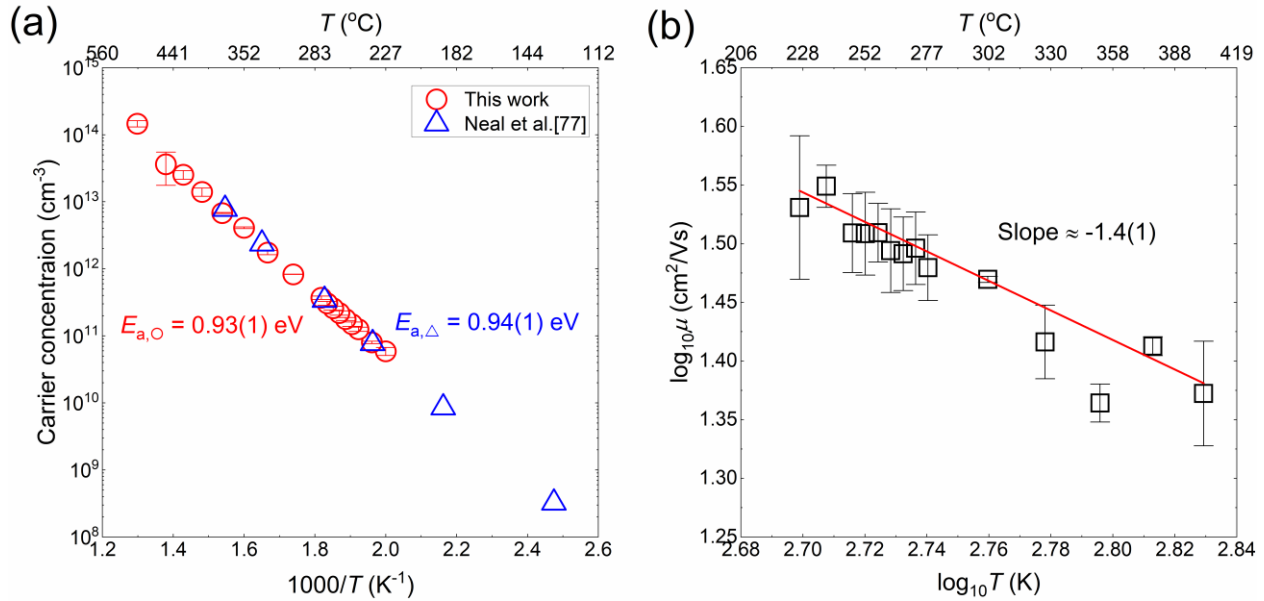


Figure 6.3 Temperature dependent (a) carrier concentration and (b) mobility.

The low-temperature electrical conductivity obtained by the resistivity measurement with van der Pauw geometry is compared to the high temperature DC and AC measurements as shown in Figure 6.2(b). The electrical conductivities are well matched, and they increase exponentially with increasing temperature from 230 °C to 700 °C, indicating that the electrical conductivity Fe-doped Ga_2O_3 is governed by one electrical conduction mechanism over this temperature range. In addition, the carrier type was confirmed to be free electrons in the conduction band.

To further understand the temperature-dependent carrier concentration, a charge neutrality equation (Eq. 6.1) was utilized to predict the concentrations of ionized defects and electronic carriers using the thermodynamic parameters listed in Table 6.1.

$$n + N_A^- = p + N_D^+ \quad (6.1)$$

where n , p , N_A^- , and N_D^+ are the concentration of electron, hole, ionized acceptor, and ionized donor which can be defined as:

$$n = N_C \exp\left(-\frac{E_C - E_F}{kT}\right) \quad (6.2)$$

$$p = N_V \exp\left(-\frac{E_F - E_V}{kT}\right) \quad (6.3)$$

$$N_A^- = \frac{N_A}{1 + 2\exp[(E_A - E_F)/kT]} \quad (6.4)$$

$$N_D^+ = \frac{N_D}{1 + 4\exp[(E_D - E_F)/kT]} \quad (6.5)$$

where N_C and N_V are the effective density of states in conduction band and valence bands, respectively. E_C and E_V are the bottom of the conduction band and the top of the valence band, respectively. E_F is the Fermi level, and k and T are respectively the Boltzmann constant and temperature. E_A and E_D are the ionization level for trivalent Fe to divalent Fe (0/-1) and for trivalent Si to tetravalent Si (0/+1), respectively. N_A and N_A^- are the total and ionized concentration of Fe. N_D and N_D^+ are the total and ionized concentration of Si.

It was assumed in this model that the net positive charge species are the singly ionized Si and holes and the net negative charge species are the singly ionized Fe and electrons. The compensation mechanism is predominantly due to the charge trapping and de-trapping at the Fe center whose transition level is predicted to be 0.78 eV from the CBM.[96] As shown in Figure 6.4(a), this model is in agreement with the observed temperature-dependent carrier concentration Hall measurements. In addition, the Fermi level is pinned to 0.84 ~ 0.87 eV over a wide range of temperatures as shown in Figure 6.4(b), explaining the observed linear relationship in $\log_{10}\sigma$ versus $1/T$. We also calculated the carrier concentration versus temperature using the Fe ionization level of 0.86 eV with N_A/N_D of 1.65 which were obtained by fitting the observed carrier concentration with a charge neutrality equation in the prior work by Neal et al.[77] The calculated activation energy was 0.93 eV which is close to the observed activation energy, however there was a slight discrepancy in magnitude between the observed and calculated carrier concentration; the calculated value is two times higher than the observed carrier concentration.

Table 6.1. Thermodynamic parameters for solving a charge neutrality equation.

Parameter	Symbol	Value	Reference
Density of state in conduction band	N_C (/cm ³)	$7.15 \times 10^{14} \times T^{1.5}$	Calculated using the effective mass of electron
Density of state in valence band	N_V (/cm ³)	$7.15 \times 10^{14} \times T^{1.5}$	
Band gap	E_g (eV)	4.85	[97]
Ionization level of Fe	$E_g - E_{acc}$ (eV)	0.78	[96]
Ionization level of Si	$E_g - E_{dn}$ (eV)	0.03	[77]
Fe concentration	N_A (/cm ³)	8×10^{17}	
Si concentration	N_D (/cm ³)	1×10^{17}	

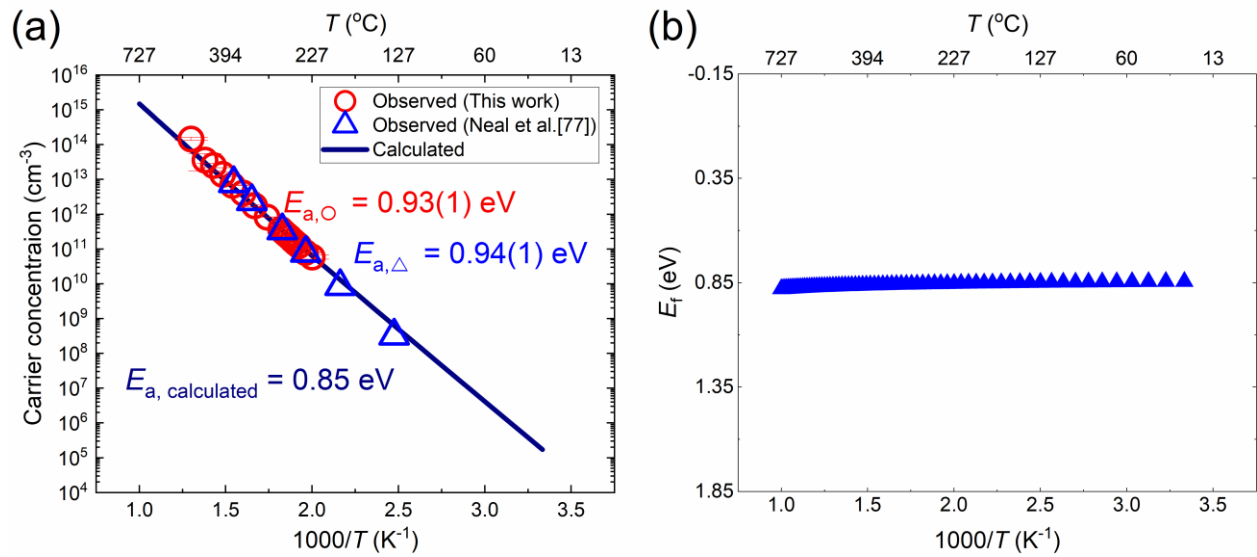


Figure 6.4. (a) Observed and calculated carrier concentrations versus temperature and (b) predicted Fermi level.

Although the prediction indicates that the charge compensation mechanism can be explained by only considering the donor (Si) and acceptor (Fe) mutual compensation, we further examined the electrical conductivity as a function of oxygen partial pressure to study a possibility of contribution of intrinsic point defects to the overall charge balance. Considering the phase stability of β -Ga₂O₃, [98] four-point-probe DC conductivity was measured from 600 °C to 820 °C in a pO_2 range of 0.21 atm (air) to 10⁻⁴ atm. As shown in Figure 6.5(a), the electrical conductivity shows pO_2 -independent behavior at 600 °C over the measurement range. With increasing temperature, the conductivity increases slightly with decreasing pO_2 , however, the dependence is weak in comparison to other multivalent acceptor doped oxide dielectrics at this pO_2 range. [43] As shown in Figure 6.5(b), an Arrhenius behavior of electrical conductivity is observed at each

pO_2 condition, and the activation energy changes gradually from 0.92 eV to 1.04 eV with decreasing pO_2 .

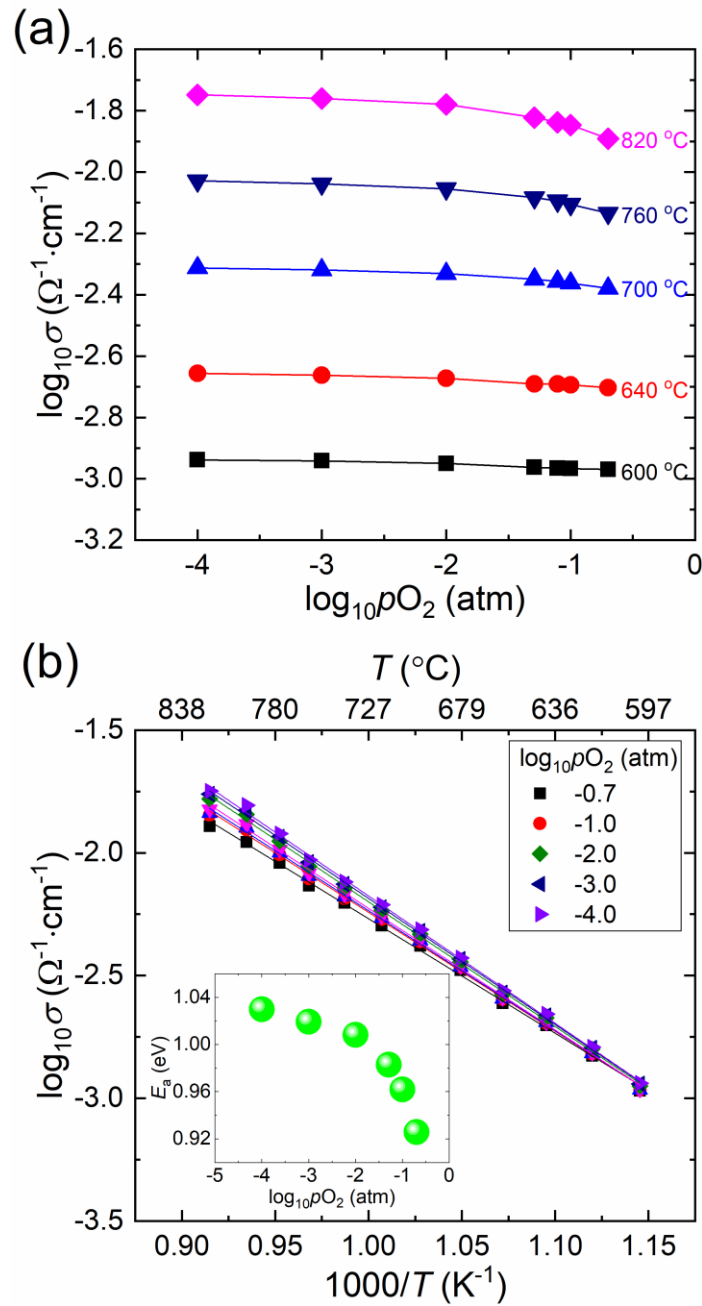


Figure 6.5. (a) Oxygen partial pressure dependent DC electrical conductivity at various temperature. (b) DC electrical conductivity versus temperature with change in activation energy (inset Figure) at each pO_2 condition.

A pO_2 -independent electrical conductivity can be explained by several defect compensating mechanisms. One mechanism is attributed to the generation of intrinsic point defects such as oxygen vacancies for ionically compensating dopants. This mechanism is generally observed in acceptor-doped oxides and their defect chemistry has been well established.[54, 99, 100] When ionic compensation dominates such that the conductivity is dominated by the ionic species, a broad pO_2 -independent electrical conductivity can be observed. In some cases, judicious choices of multivalent acceptors and donors can override the ionic compensation and pin the Fermi level over broad pO_2 ranges as shown for $BaTiO_3$ in Chapter 6 and the early studies.[63, 64] In the Fe-doped β - Ga_2O_3 studied here, the pO_2 -independent electrical conductivity is attributed to the pinned Fermi level due to the dominating impurity donor (Si) compensating the acceptor (Fe), and a total electrical conductivity is predominantly governed by electron conductivity over a broad range of pO_2 . According to DFT calculations,[5, 28] in reducing conditions the oxygen vacancy formation energy is the lowest among the native point defects, except for triply ionized gallium interstitials at very low Fermi energies, which are believed to act as a deep donors. This suggests the low concentration of intrinsic point defects in β - Ga_2O_3 single crystals. Moreover, the Hall measurement and the charge neutrality equation reveal that Si donor and the Fe acceptor mutual compensation can explain the electronic conductivity over a wide range of temperature. Therefore, the semi-insulating pO_2 -independent electrical conductivity of Fe-doped β - Ga_2O_3 is attributed to the donor and multivalent acceptor co-doping mechanism with the low concentration of intrinsic point defects.

It is important to note that with increasing temperature we observed a slight increase in the electrical conductivity along with a transition to a slightly higher activation energy as the sample equilibrates with a reduced pO_2 . This is probably due to a minor additional contribution of electrons generated by intrinsic deeper donors such as oxygen vacancies. The influence of non-stoichiometric lattice defects is not very significant at these measurement conditions since the Fermi level is pinned by the Si and Fe; however, the results suggest that there is a possibility of generating nonstoichiometric point defects with further increasing temperature or reducing pO_2 .

6.5. Conclusions

The semi-insulating properties of Fe-doped β -Ga₂O₃ single crystals grown via the edge-defined film-fed method were investigated as a function of temperature and oxygen partial pressure. It was revealed from the DC and AC conductivities and Hall measurements that the in-plane electrical conductivity perpendicular to the ($\bar{2}01$) crystallographic planes follows an Arrhenius behavior from 230 °C to 800 °C with an activation energy of 0.84 ~ 0.94 eV. The Hall measurements showed that the crystal is *n*-type. While the carrier concentration showed a positive temperature dependence, the mobility exhibited a negative temperature dependence, characteristic of phonon scattering. The electrically semi-insulating conductivity was explained by a low electron concentration, which is achieved by donor (Si) and acceptor (Fe) mutual compensation, leading to Fermi level pinning over a wide range of temperature. The DC electrical conductivity versus pO_2 was examined from 600 °C to 800 °C from air to 10^{-4} atm and showed that the conductivity is pO_2 -independent at 600 °C, suggesting a low intrinsic point defect concentration. At higher temperatures, the electrical conductivity increased moderately with reducing pO_2 , which is probably due to the generation of electron compensating intrinsic point defects such as oxygen vacancies.

Chapter 7

Conclusions and Future works

7.1. Conclusions

The works in this dissertation are desired for the fundamental understanding of electrical conductivity and defect chemistry of two different oxides, Fe-doped β -Ga₂O₃ single crystal and doped BaTiO₃ ceramics. Chapter 4 and 5 investigate the DC and AC electrical conductivities and resistance degradation behavior of Mg or Mn singly doped and (Mg+Y) or (Mn+Y) co-doped BaTiO₃ ceramics. The DC measurements reveal that the high-temperature (900 °C) *p*-type bulk electrical conductivity in high *p*O₂ range (air – 10⁻⁴ atm) can be achieved by Mg or Mn single doping or (Mg+Y) co-doping. On the other hand, the electrical conductivity of BaTiO₃ can be pinned (i.e. the *p*O₂-independent electrical conductivity) by co-doping of (Mn+Y) in these measurement range. In addition, the AC impedance analyses show that (Mn+Y) co-doped BaTiO₃ exhibits the lowest bulk conductivity over a wide range of temperature. Moreover, (Mn+Y) co-doping can significantly enhance the degradation resistance of BaTiO₃ at 500 °C under the electric field of 45 V/cm. The calculated canonical defect chemistry explains that the improved resistance of electrical conduction and degradation is attributed to (1) the pinning of electronic charge carrier as a function of *p*O₂ at both 900 °C and 500 °C and (2) the significantly reduced oxygen vacancy concentration by the mutual compensation of donor (Y) and multivalent acceptor (Mn).

In Chapter 6, the origin of semi-insulating electrical conductivity of Fe-doped (010) β -Ga₂O₃ single crystal is investigated in terms of defect chemistry. Similar to Mn and Y co-doped BaTiO₃, the *p*O₂-independent electrical conductivity is seen over a wide range of oxygen partial pressure (air – 10⁻⁴ atm) at various high-temperatures (600 °C – 800 °C). Hall measurement reveals that Fe-doped β -Ga₂O₃ single crystal exhibits the electronic conductivity is mainly limited by the concentration of electron at these measurement conditions. The charge neutrality equation shows that the background Si impurities act as donors and the intentionally doped Fe ions act as acceptor.

Therefore, the donor (Si) and acceptor (Fe) mutual compensation is achieved, which leads to the pinned Fermi level over a wide range of temperature with the low concentration of intrinsic point defects.

7.2. Future works

7.2.1. Bulk electrical conductivity of BaTiO₃

In Chapter 5, the temperature-dependent bulk conductivity obtained by fitting of Cole-Cole plots reveals that the bulk conductivity is lowest in (Mn+Y) co-doped BaTiO₃ from 500 °C to 900 °C in air. In Figure 7.1, we further explore the bulk conductivity below 500 °C and realize that the bulk conductivity of (Mn+Y) co-doped BaTiO₃ is lowest than the other compositions as decreasing temperature even below 500 °C due to the relatively high activation energy. Moreover, there is a transition of activation energy at intermediate temperature range (approximately 350 °C ~ 500 °C) in Mg-doped, Mn-doped and (Mg+Y) co-doped compositions, while the activation energy in Mn and Y co-doped BaTiO₃ is almost temperature-invariant.

At this point an origin of the change in activation energy is not clearly understood but it may be related to the motion of oxygen vacancies. At low-temperature, oxygen vacancies are expected to be frozen, however, the defects may start to move with increasing temperature. At the intermediate temperature range, the vacancies now contribute to the total electrical conductivity in Mg, Mn, and (Mg+Y) compositions. On the other hand, in the (Mn+Y) composition, the transition range is not seen because of the low concentration of oxygen vacancy.

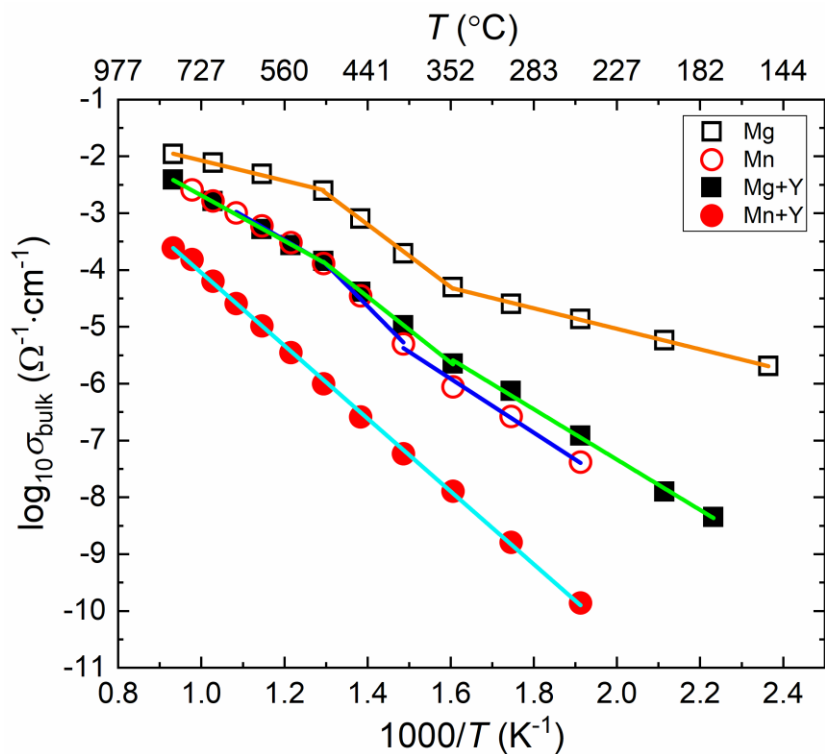


Figure 7.1 Temperature-dependent bulk conductivity of 0.5 mol% Mg-doped, 0.5 mol% Mn-doped, (0.5 mol% Mg and 1.0 mol% Y) co-doped, and (0.5 mol% Mn and 0.5 mol% Y) co-doped BaTiO₃ compositions in air.

Table 7.1 Activation energy of bulk conductivity at different temperature range.

Composition	Activation energy (eV)		
	High-temperature (900 °C ~ 500 °C)	Intermediate-temperature (500 °C ~ 350 °C)	Low-temperature (350 °C ~ 200 °C)
Mg	0.35(1)	1.01(1)	0.36(1)
Mn	0.84(2)	1.41(4)	0.88(5)
(Mg+Y)	0.79(1)	1.15(1)	0.88(2)
(Mn+Y)	1.27(1)		

7.2.2. Grain boundary effects at low-temperature in BaTiO₃

The AC impedance analyses reveal that the grain-boundary conductivity is predominant at low-temperature in the Mg, Mn, and (Mg+Y) samples as shown in Figure 7.2. However, the total conductivity is mainly limited by bulk conductivity in (Mn+Y) co-doped BaTiO₃. In addition, the higher activation energy is observed in the grain-boundary conductivity in the Mg, Mn and (Mg+Y) samples, while the activation energies of both bulk and grain-boundary conductivities are very close with each other in (Mn+Y) co-doped BaTiO₃. We presumably conclude that this phenomenon is probably related to the dopant segregation or depletion at grain-boundary, which may affect the local defect chemistry.

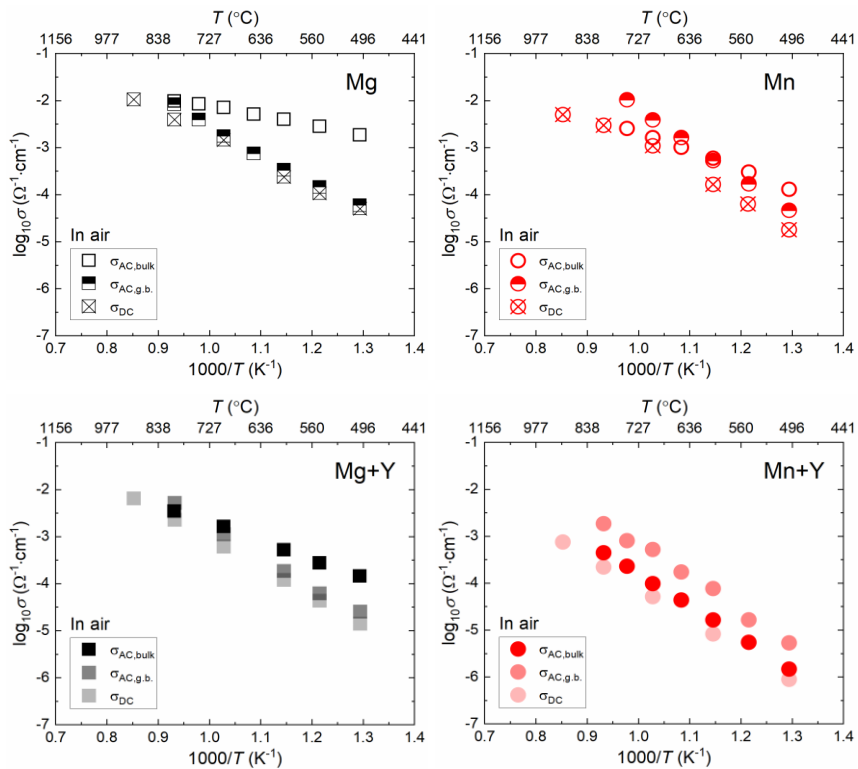


Figure 7.2 Temperature dependent bulk and grain-boundary conductivities of (a) 0.5 mol% Mg-doped, (b) 0.5 mol% Mn-doped, (c) (0.5 mol% Mg and 1.0 mol% Y) co-doped, and (d) (0.5 mol% Mn and 0.5 mol% Y) co-doped BaTiO₃ in air.

7.2.3. AC and DC conductivities versus pO_2 at low-temperature in BaTiO₃

It is important to note again that the total DC and AC conductivity is highly dependent on grain-boundary conductivity at low-temperature in acceptor-doped BaTiO₃. In Figure 7.3, we measured the AC impedance as a function of oxygen partial pressure in Mn-doped BaTiO₃ and realized that the bulk and grain-boundary conductivities show the difference in degree of pO_2 -dependence. In Mn-doped BaTiO₃, the total electrical conductivity is mainly governed by the grain-boundary conductivity in air condition, however the total conductivity is almost equally limited by the bulk and grain-boundary conductivities in 10^{-4} atm. Moreover, the grain-boundary conductivity is almost pO_2 -independent, while the grain conductivity is pO_2 -dependent. The slopes in $\log_{10}\sigma$ versus $\log_{10}pO_2$ for the DC, grain, and grain-boundary conductivity is listed in Table 7.2. In the case of Mn and Y co-doped BaTiO₃, the DC and AC total conductivities are predominantly limited by grain regardless of oxygen partial pressure. Both grain and grain-boundary conductivity are independent on oxygen partial pressure at this temperature.

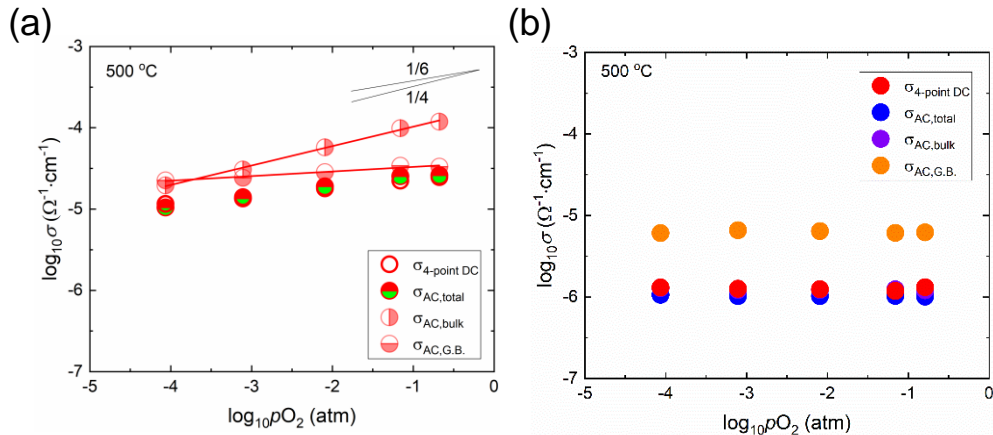


Figure 7.3 DC and AC electrical conductivities versus pO_2 of (a) 0.5 mol% Mn-doped and (b) (0.5 mol% Mn and 0.5 mol% Y) co-doped BaTiO₃ at 500 °C.

Table 7.2 Slope in $\log_{10}\sigma$ versus $\log_{10}pO_2$ measured by the DC and AC techniques in 0.5 mol% Mn-doped at 500 °C.

Type of electrical conductivity	Slope in $\log_{10}\sigma$ versus $\log_{10}pO_2$
DC conductivity	1/10
Bulk conductivity	1/4.2
Grain-boundary conductivity	1/17.7

REFERENCES

- [1] R. Zucca, "Electrical compensation in semi-insulating GaAs", *Journal of Applied Physics* **48**: 1987–1994 (1977)
- [2] M. Acosta, N. Novak, V. Rojas, S. Patel, R. Vaish, J. Koruza, G.A. Rossetti, and J. Rödel, "BaTiO₃-based piezoelectrics: Fundamentals, current status, and perspectives", *Applied Physics Reviews* **4**: 041305 (2017)
- [3] K. Hong, T.H. Lee, J.M. Suh, S.-H. Yoon, and H.W. Jang, "Perspectives and challenges in multilayer ceramic capacitors for next generation electronics", *Journal of Materials Chemistry C* **7**: 9782–9802 (2019)
- [4] M. Higashiwaki, K. Sasaki, H. Murakami, Y. Kumagai, A. Koukitu, A. Kuramata, T. Masui, and S. Yamakoshi, "Recent progress in Ga₂O₃ power devices", *Semiconductor Science and Technology* **31**: 034001 (2016)
- [5] T. Zacherle, P.C. Schmidt, and M. Martin, "Ab initio calculations on the defect structure of β -Ga₂O₃", *Physical Review B* **87**: 1–10 (2013)
- [6] A.E. Romanov, S.I. Stepanov, V.I. Nikolaev, and V.E. Bougrov, "GALLIUM OXIDE: PROPERTIES AND APPLICATIONS A REVIEW", *Rev Adv Mater Sci* **44**: 63–86 (2016)
- [7] N. Ueda, H. Hosono, R. Waseda, and H. Kawazoe, "Synthesis and control of conductivity of ultraviolet transmitting β -Ga₂O₃ single crystals", *Applied Physics Letters* **70**: 3561–3563 (1997)
- [8] T. Onuma, S. Fujioka, T. Yamaguchi, M. Higashiwaki, K. Sasaki, T. Masui, and T. Honda, "Correlation between blue luminescence intensity and resistivity in β -Ga₂O₃ single crystals", *Applied Physics Letters* **103**: 041910 (2013)

- [9] M. Orita, H. Ohta, M. Hirano, and H. Hosono, "Deep-ultraviolet transparent conductive β - Ga_2O_3 thin films", *Applied Physics Letters* **77**: 4166–4168 (2000)
- [10] E.G. Villora, K. Shimamura, Y. Yoshikawa, T. Ujiie, and K. Aoki, "Electrical conductivity and carrier concentration control in β - Ga_2O_3 by Si doping", *Applied Physics Letters* **92**: 202120 (2008)
- [11] A. Kuramata, K. Koshi, S. Watanabe, Y. Yamaoka, T. Masui, and S. Yamakoshi, "High-quality β - Ga_2O_3 single crystals grown by edge-defined film-fed growth", *Japanese Journal of Applied Physics* **55**: 1202A2 (2016)
- [12] M. Higashiwaki, K. Sasaki, A. Kuramata, T. Masui, and S. Yamakoshi, "Gallium oxide (Ga_2O_3) metal-semiconductor field-effect transistors on single-crystal β - Ga_2O_3 (010) substrates", *Applied Physics Letters* **100**: 013504 (2012)
- [13] S.J. Pearton, J. Yang, P.H. Cary, F. Ren, J. Kim, M.J. Tadjer, and M.A. Mastro, "A review of Ga_2O_3 materials, processing, and devices", *Applied Physics Reviews* **5**: 011301 (2018)
- [14] H. Kishi, Y. Mizuno, and H. Chazono, "Base-metal electrode-multilayer ceramic capacitors: Past, present and future perspectives", *Japanese Journal of Applied Physics, Part 1: Regular Papers and Short Notes and Review Papers* **42**: 1–5 (2003)
- [15] G.Y. Yang, G.D. Lian, E.C. Dickey, C.A. Randall, D.E. Barber, P. Pinceloup, M.A. Henderson, R.A. Hill, J.J. Beeson, and D.J. Skamser, "Oxygen nonstoichiometry and dielectric evolution of BaTiO_3 . Part II- Insulation resistance degradation under applied dc bias", *Journal of Applied Physics* **96**: 7500–7508 (2004)
- [16] R. Waser, T. Baiatu, and K. -H Hardtl, "dc Electrical Degradation of Perovskite-Type Titanates: I, Ceramics", *Journal of the American Ceramic Society* **73**: 1645–1653 (1990)

- [17] R. Waser, T. Baiatu, and K.-H. Hardtl, "dc Electrical Degradation of Perovskite-Type Titanates: II, Single Crystals", *Journal of the American Ceramic Society* **73**: 1654–1662 (1990)
- [18] D.M. Long, B. Cai, J.N. Baker, P.C. Bowes, T.J.M. Bayer, J.J. Wang, R. Wang, L.Q. Chen, C.A. Randall, D.L. Irving, and E.C. Dickey, "Conductivity of iron-doped strontium titanate in the quenched and degraded states", *Journal of the American Ceramic Society* **102**: 3567–3577 (2019)
- [19] J.J. Wang, H.B. Huang, T.J.M. Bayer, A. Moballeggh, Y. Cao, A. Klein, E.C. Dickey, D.L. Irving, C.A. Randall, and L.Q. Chen, "Defect chemistry and resistance degradation in Fe-doped SrTiO₃ single crystal", *Acta Materialia* **108**: 229–240 (2016)
- [20] T.J.M. Bayer, J.J. Wang, J.J. Carter, A. Moballeggh, J. Baker, D.L. Irving, E.C. Dickey, L.Q. Chen, and C.A. Randall, "The relation of electrical conductivity profiles and modulus data using the example of STO:Fe single crystals: A path to improve the model of resistance degradation", *Acta Materialia* **117**: 252–261 (2016)
- [21] T. Sasaki, and K. Hijikata, "Electrical Property of β -Gallium Sesquioxide", *Proceedings of the Institute of Natural Sciences, Nihon University* **9**: 29 (1974)
- [22] L.N. Cojocar, and I.D. Alecu, "Electrical Properties of β -Ga₂O₃", *Zeitschrift für Physikalische Chemie Neue Folge* **84**: 325–331 (1974)
- [23] L.N. Cojocar, and A. Prodan, "Electrical Conductivity and Thermogravimetric Studies of β -Ga₂O₃", *Revue Roumaine de Physique* **19**: 209–214 (1974)
- [24] M. Fleischer, L. Hollbauer, E. Born, and H. Meixner, "Evidence for a Phase Transition of beta-Gallium Oxide at Very Low Oxygen Pressures", *Journal of American Ceramics Society* **80**: 2121–2125 (1997)

- [25] M. FLEISCHER, W. Hanrieder, and H. Meixner, "Stability of Semiconducting Gallium Oxide Thin Film", *Thin Solid Films* **190**: 93–102 (1990)
- [26] N. Suzuki, S. Ohira, M. Tanaka, T. Sugawara, K. Nakajima, and T. Shishido, "Fabrication and characterization of transparent conductive Sn-doped β -Ga₂O₃ single crystal", *physica status solidi (c)* **4**: 2310–2313 (2007)
- [27] D. Gogova, G. Wagner, M. Baldini, M. Schmidbauer, K. Irmischer, R. Schewski, Z. Galazka, M. Albrecht, and R. Fornari, "Structural properties of Si-doped β -Ga₂O₃ layers grown by MOVPE", *Journal of Crystal Growth* **401**: 665–669 (2014)
- [28] J.B. Varley, J.R. Weber, A. Janotti, and C.G. Van de Walle, "Oxygen vacancies and donor impurities in β -Ga₂O₃", *Applied Physics Letters* **97**: 142106 (2010)
- [29] S. Lany, "Defect phase diagram for doping of Ga₂O₃", *APL Materials* **6**: 046103 (2018)
- [30] T. Shi, Y. Chen, and X. Guo, "Defect chemistry of alkaline earth metal (Sr/Ba) titanates", *Progress in Materials Science* **80**: 77–132 (2016)
- [31] S. Lee, and C.A. Randall, "Determination of electronic and ionic conductivity in mixed ionic conductors: HiTEC and in-situ impedance spectroscopy analysis of isovalent and aliovalent doped BaTiO₃", *Solid State Ionics* **249–250**: 86–92 (2013)
- [32] P.C. Bowes, J.N. Baker, J.S. Harris, B.D. Behrhorst, and D.L. Irving, "Influence of impurities on the high temperature conductivity of SrTiO₃", *Applied Physics Letters* **112**: 22902 (2018)
- [33] P.C. Bowes, J.N. Baker, and D.L. Irving, "Site preference of Y and Mn in nonstoichiometric BaTiO₃ from first principles", *Physical Review Materials* **4**: 084601 (2020)

- [34] Y. Wu, P.C. Bowes, J.N. Baker, and D.L. Irving, "Influence of space charge on the conductivity of nanocrystalline SrTiO₃", *Journal of Applied Physics* **128**: (2020)
- [35] P.C. Bowes, J.N. Baker, and D.L. Irving, "Survey of acceptor dopants in SrTiO₃: Factors limiting room temperature hole concentration", *Journal of the American Ceramic Society* **103**: 1156–1173 (2020)
- [36] J.N. Baker, P.C. Bowes, J.S. Harris, and D.L. Irving, "Mechanisms governing metal vacancy formation in BaTiO₃ and SrTiO₃", *Journal of Applied Physics* **124**: 114101 (2018)
- [37] S. Lee, C.A. Randall, and Z.K. Liu, "Comprehensive linkage of defect and phase equilibria through ferroelectric transition behavior in BaTiO₃-based dielectrics: Part 2. Defect modeling under low oxygen partial pressure conditions", *Journal of the American Ceramic Society* **91**: 1753–1761 (2008)
- [38] C.R. Song, and H.I. Yoo, "Chemical diffusivity of Defect chemical analysis", *Physical Review B - Condensed Matter and Materials Physics* **61**: 3975–3982 (2000)
- [39] H.I. Yoo, and C.R. Song, "Defect structure and chemical diffusion in BaTiO_{3-δ}", *Solid State Ionics* **135**: 619–623 (2000)
- [40] H.I. Yoo, and K.D. Becker, "Effect of hole-trapping on mass/charge transport properties in acceptor-doped BaTiO₃", *Physical Chemistry Chemical Physics* **7**: 2068–2073 (2005)
- [41] M.B. Choi, S.Y. Jeon, H.N. Im, and S.J. Song, "Thermodynamic quantities and oxygen nonstoichiometry of undoped BaTiO_{3-δ} by thermogravimetric analysis", *Journal of Alloys and Compounds* **513**: 487–494 (2012)
- [42] C.-R. Song, and H.-I. Yoo, "Chemical Diffusivity of BaTiO_{3-δ}: IV, Acceptor-Doped Case", *Journal of the American Ceramic Society* **83**: 773–779 (2004)

- [43] J.Y. Kim, C.R. Song, and H.I. Yoo, "Mn-doped BaTiO₃: Electrical Transport Properties in Equilibrium State", *Journal of Electroceramics* **1**: 27–39 (1997)
- [44] J. Daniels, and K.H. Hardtl, "Electrical Conductivity at High Temperatures of Donor-Doped Barium Titanate Ceramics", *Philips Res Rep* **31**: 489–504 (1976)
- [45] H.-I. Yoo, C.-R. Song, and D.-K. Lee, "BaTiO_{3-δ}: Defect Structure, Electrical Conductivity, Chemical Diffusivity, Thermoelectric Power, and Oxygen Nonstoichiometry", *Journal of Electroceramics* **8**: 5–36 (2002)
- [46] H.-J. Hagemann, and D. Hennings, "Reversible Weight Change of Acceptor-Doped BaTiO₃", *Journal of the American Ceramic Society* **64**: 590–594 (1981)
- [47] H.I. Yoo, T.S. Oh, H.S. Kwon, D.K. Shin, and J.S. Lee, "Electrical conductivity-defect structure correlation of variable-valence and fixed-valence acceptor-doped BaTiO₃ in quenched state", *Physical Chemistry Chemical Physics* **11**: 3115–3126 (2009)
- [48] S.H. Yoon, C.A. Randall, and K.H. Hur, "Difference between resistance degradation of fixed valence acceptor (Mg) and variable valence acceptor (Mn)-doped BaTiO₃ ceramics", *Journal of Applied Physics* **108**: (2010)
- [49] J. Nowotny, and M. Rekas, "Defect structure, electrical properties and transport in Barium Titanate. VI. General defect model", *Ceramics International* **20**: 257–263 (1994)
- [50] S.H. Yoon, K.H. Lee, and H. Kim, "Effect of acceptors on the segregation of donors in niobium-doped barium titanate positive temperature coefficient resistors", *Journal of the American Ceramic Society* **83**: 2463–2472 (2000)
- [51] N. -H CHAN, R.K. SHARMA, and D.M. SMYTH, "Nonstoichiometry in Undoped BaTiO₃", *Journal of the American Ceramic Society* **64**: 556–562 (1981)

- [52] P.C. Bowes, G.H. Ryu, J.N. Baker, E.C. Dickey, and D.L. Irving, "Fermi Level Pinning in Co-doped BaTiO₃ : Part II . Defect Chemistry Models", In preparation
- [53] J. Nowotny, and M. Rekas, "Defect structure, electrical properties and transport in barium titanate. III. Electrical conductivity, thermopower and transport in single crystalline BaTiO₃", *Ceramics International* **20**: 225–235 (1994)
- [54] Y.H. HAN, J.B. APPLEBY, and D.M. SMYTH, "Calcium as an Acceptor Impurity in BaTiO₃", *Journal of the American Ceramic Society* **70**: 96–100 (1987)
- [55] J. Jeong, and Y. Ho Han, "Electrical properties of MgO-doped BaTiO₃", *Physical Chemistry Chemical Physics* **5**: 2264–2267 (2003)
- [56] R.K. SHARMA, N. -H CHAN, and D.M. SMYTH, "Solubility of TiO₂ in BaTiO₃", *Journal of the American Ceramic Society* **64**: 448–451 (1981)
- [57] S. -i Osawa, A. Furuzawa, and N. Fujikawa, "Effect of the Manganese Valence State on the Electrical Conductivity of Barium Titanate", *Journal of the American Ceramic Society* **76**: 1191–1194 (1993)
- [58] S.H. Yoon, C.A. Randall, and K.H. Hur, "Effect of acceptor concentration on the bulk electrical conduction in acceptor (Mg)-doped BaTiO₃", *Journal of Applied Physics* **107**: 103721 (2010)
- [59] S.H. Yoon, C.A. Randall, and K.H. Hur, "Influence of grain size on impedance spectra and resistance degradation behavior in acceptor (Mg)-doped BaTiO₃ ceramics", *Journal of the American Ceramic Society* **92**: 2944–2952 (2009)
- [60] S.H. Yoon, M.H. Hong, J.O. Hong, Y.T. Kim, and K.H. Hur, "Effect of acceptor (Mg) concentration on the electrical resistance at room and high (200 °C) temperatures of acceptor (Mg)-doped BaTiO₃ ceramics", *Journal of Applied Physics* **102**: (2007)

- [61] S.H. Yoon, C.A. Randall, and K.H. Hur, "Effect of acceptor (Mg) concentration on the resistance degradation behavior in acceptor (Mg)-doped BaTiO₃ bulk ceramics: I. impedance analysis", *Journal of the American Ceramic Society* **92**: 1758–1765 (2009)
- [62] N.-H. Chan, and D.M. Smyth, "Defect Chemistry of Donor-Doped BaTiO₃", *Journal of the American Ceramic Society* **67**: 285–288 (1984)
- [63] C.E. Lee, S.H. Kang, D.S. Sinn, and H.I. Yoo, "Co-doping effect of Mn and Y on charge and mass transport properties of BaTiO₃", *Journal of Electroceramics* **13**: 785–791 (2004)
- [64] Y.Y. Yeoh, H. Jang, and H.I. Yoo, "Defect structure and Fermi-level pinning of BaTiO₃ co-doped with a variable-valence acceptor (Mn) and a fixed-valence donor (Y)", *Physical Chemistry Chemical Physics* **14**: 1642–1648 (2012)
- [65] J. Jeong, E.J. Lee, and Y.H. Han, "Defect chemistry and electrical degradation of BaTiO₃ co-doped with Ho and Mn", *Journal of the European Ceramic Society* **27**: 1159–1163 (2007)
- [66] E.J. Lee, J. Jeong, and Y.H. Han, "Defects and degradation of BaTiO₃ codoped with Dy and Mn", *Japanese Journal of Applied Physics, Part 1: Regular Papers and Short Notes and Review Papers* **45**: 822–825 (2006)
- [67] K. Kaneda, Y. Iwazaki, and Y. Konishi, "The mechanism of lifetime improvement through vanadium addition to multilayer ceramic capacitor with nickel electrode", *Journal of the Ceramic Society of Japan* **126**: 931–935 (2018)
- [68] H. Natsui, T. Shibahara, Y. Yonezawa, and O. Kido, "Effect of Vanadium Addition on Reliability and Microstructure of BaTiO₃-Based Multilayer Ceramic Capacitors", *Japanese Journal of Applied Physics* **51**: 09LC09 (2012)

- [69] J. Jeong, and Y.H. Han, "Effects of Mn-doping on TSDC and degradation of BaTiO₃", *Journal of Electroceramics* **17**: 1051–1055 (2006)
- [70] S.H. Yoon, C.A. Randall, and K.H. Hur, "Effect of Acceptor (Mg) concentration on the resistance degradation behavior in acceptor (Mg)-doped BaTiO₃ bulk ceramics: II. Thermally stimulated depolarization current analysis", *Journal of the American Ceramic Society* **92**: 1766–1772 (2009)
- [71] W. Liu, and C.A. Randall, "Thermally stimulated relaxation in Fe-doped SrTiO₃ systems: I. Single crystals", *Journal of the American Ceramic Society* **91**: 3245–3250 (2008)
- [72] J. Jeong, and Y.H. Han, "Effects of Mn-doping on TSDC and degradation of BaTiO₃", *Journal of Electroceramics* **17**: 1051–1055 (2006)
- [73] S.-H. Yoon, S.-H. Kim, and D.-Y. Kim, "Correlation between I (current)-V (voltage) characteristics and thermally stimulated depolarization current of Mn-doped BaTiO₃ multilayer ceramic capacitor", *Journal of Applied Physics* **114**: 074102 (2013)
- [74] S.H. Yoon, J.S. Park, S.H. Kim, and D.Y. Kim, "Thermally stimulated depolarization current analysis for the dielectric aging of Mn and V-codoped BaTiO₃ multi layer ceramic capacitor", *Applied Physics Letters* **103**: 42901 (2013)
- [75] S.H. Yoon, J.B. Lim, S.H. Kim, and D.Y. Kim, "Influence of Dy on the dielectric aging and thermally stimulated depolarization current in Dy and Mn-codoped BaTiO₃ multilayer ceramic capacitor", *Journal of Materials Research* **28**: 3252–3256 (2013)
- [76] M. Fleischer, and H. Meixner, "Electron mobility in single- and polycrystalline Ga₂O₃", *Journal of Applied Physics* **74**: 300–305 (1993)

- [77] A.T. Neal, S. Mou, S. Rafique, H. Zhao, E. Ahmadi, J.S. Speck, K.T. Stevens, J.D. Blevins, D.B. Thomson, N. Moser, K.D. Chabak, and G.H. Jessen, "Donors and deep acceptors in β -Ga₂O₃", *Applied Physics Letters* **113**: 62101 (2018)
- [78] D. Long, N. Creange, A. Moballegh, and E.C. Dickey, "Electromigration-induced leakage current enhancement and its anisotropy in single crystal TiO₂", *Journal of Applied Physics* **125**: 184101 (2019)
- [79] X.W. ZHANG, Y.H. HAN, M. LAL, and D.M. SMYTH, "Defect chemistry of BaTiO₃ with additions of CaTiO₃", *Journal of the American Ceramic Society* **70**: 100–103 (1987)
- [80] N.-H. CHAN, R.K. SHARMA, and D.M. SMYTH, "Nonstoichiometry in acceptor-doped BaTiO₃", *Journal of the American Ceramic Society* **65**: 167–170 (1982)
- [81] D.K. Lee, H.I. Yoo, and K.D. Becker, "Nonstoichiometry and defect structure of Mn-doped BaTiO_{3- δ} ", *Solid State Ionics* **154–155**: 189–193 (2002)
- [82] R. Moos, and K.H. Härdtl, "Defect chemistry of donor-doped and undoped strontium titanate ceramics between 1000° and 1400°C", *Journal of the American Ceramic Society* **80**: 2549–2562 (1997)
- [83] R.A. Maier, C.A. Randall, and J. Stevenson, "Low Temperature Ionic Conductivity of an Acceptor-Doped Perovskite: II. Impedance of Single-Crystal BaTiO₃", *Journal of the American Ceramic Society* **99**: 3360–3366 (2016)
- [84] Y. Tsur, T.D. Dunbar, and C.A. Randall, "Crystal and defect chemistry of rare earth cations in BaTiO₃", *Journal of Electroceramics* **7**: 25–34 (2001)
- [85] N. Hirose, and A.R. West, "Impedance Spectroscopy of Undoped BaTiO₃ Ceramics", *Journal of the American Ceramic Society* **79**: 1633–1641 (1996)

- [86] I.J. Clark, F.B. Marques, and D.C. Sinclair, "The influence of grain boundary impedances on the p-type conductivity of undoped BaTiO₃ ceramics", *Journal of the European Ceramic Society* **22**: 579–583 (2002)
- [87] M. Prades, N. Masó, H. Beltrán, E. Cordoncillo, and A.R. West, "Field enhanced bulk conductivity of BaTiO₃: Mg ceramics", *Journal of Materials Chemistry* **20**: 5335–5344 (2010)
- [88] M. Prades, H. Beltrán, E. Cordoncillo, P.J. Alonso, N. Masó, and A.R. West, "Non-ohmic phenomena in Mn-doped BaTiO₃", *Physica Status Solidi (A) Applications and Materials Science* **209**: 2267–2272 (2012)
- [89] T. Baiatu, R. Waser, and K. -H Härdtl, "dc Electrical Degradation of Perovskite-Type Titanates: III, A Model of the Mechanism", *Journal of the American Ceramic Society* **73**: 1663–1673 (1990)
- [90] D.W. Hahn, S.B. Sohn, and Y.H. Han, "Effects of rare-earth oxides on time-dependent dielectric properties of Mn-doped BaTiO₃", *Japanese Journal of Applied Physics* **48**: 031404 (2009)
- [91] Y. Tsur, A. Hitomi, I. Scrymgeour, and C.A. Randall, "Site Occupancy of Rare-Earth Cations in BaTiO₃", *Japanese Journal of Applied Physics* **40**: 255–258 (2001)
- [92] A. Kyrtos, M. Matsubara, and E. Bellotti, "On the feasibility of p-type Ga₂O₃", *Applied Physics Letters* **112**: 032108 (2018)
- [93] B.W. Veal, P.M. Baldo, A.P. Paulikas, and J.A. Eastman, "Understanding Artifacts in Impedance Spectroscopy", *Journal of The Electrochemical Society* **162**: H47–H57 (2015)

- [94] A.Y. Polyakov, N.B. Smirnov, I. V Shchemerov, S.J. Pearton, F. Ren, A. V Chernykh, and A.I. Kochkova, "Electrical properties of bulk semi-insulating β -Ga₂O₃(Fe)", *Applied Physics Letters* **113**: 142102 (2018)
- [95] S.M. Sze, and K.K. Ng, *Physics of Semiconductor Devices: Third Edition*. John Wiley & Sons, New York (2006)
- [96] M.E. Ingebrigtsen, J.B. Varley, A.Y. Kuznetsov, B.G. Svensson, G. Alfieri, A. Mihaila, and U. Badstübner, "Iron and intrinsic deep level states in Ga₂O₃", *Applied Physics Letters* **112**: 11301 (2018)
- [97] C. Janowitz, V. Scherer, M. Mohamed, A. Krapf, H. Dwelk, R. Manzke, Z. Galazka, R. Uecker, K. Irmischer, R. Fornari, M. Michling, D. Schmeißer, J.R. Weber, J.B. Varley, and C.G. Van de Walle, "Experimental electronic structure of In₂O₃ and Ga₂O₃", *New Journal of Physics* **13**: 085014 (2011)
- [98] R. Togashi, K. Nomura, C. Eguchi, T. Fukizawa, K. Goto, Q.T. Thieu, H. Murakami, Y. Kumagai, A. Kuramata, S. Yamakoshi, B. Monemar, and A. Koukitu, "Thermal stability of β -Ga₂O₃ in mixed flows of H₂ and N₂", *Japanese Journal of Applied Physics* **54**: 41102 (2015)
- [99] C.B. Gopal, and S.M. Haile, "An electrical conductivity relaxation study of oxygen transport in samarium doped ceria", *Journal of Materials Chemistry A* **2**: 2405–2417 (2014)
- [100] R. Waser, "Bulk Conductivity and Defect Chemistry of Acceptor-Doped Strontium Titanate in the Quenched State", *Journal of the American Ceramic Society* **74**: 1934–1940 (1991)

APPENDIX

Crystallization Behavior of Amorphous BaTiO₃ Thin Films

Published in Journal of Materials and Science (16 April 2020)

Gyung Hyun Ryu¹, Neal Lewis¹, George N. Kotsonis^{1,2}, Jon-Paul Maria^{1,2},
and Elizabeth C. Dickey^{1,*}

¹*Department of Materials Science and Engineering, North Carolina State University, Raleigh,
North Carolina 27695, USA*

²*Department of Materials Science and Engineering, The Pennsylvania State University,
University Park, Pennsylvania 16802, USA*

Abstract

The crystallization behavior of amorphous barium titanate (BaTiO₃) thin films was studied as a function of annealing temperature from 500 to 1000 °C. Quantitative phase analysis by grazing incidence X-ray diffractometry revealed that the metastable hexagonal phase preferentially nucleates at lower temperatures with a transition to stable cubic nuclei at higher temperatures. The predominance of the metastable hexagonal-phase nucleation at lower temperatures suggests that it has the lowest nucleation barrier, in accordance with the Ostwald's step rule. To help induce the nucleation of the cubic phase at lower temperatures, we explored the effects of electric fields on the crystallization behavior and found that direct-current fields moderately enhanced the cubic phase fraction in the 500–700 °C temperature range. Although the nucleation barrier of the cubic phase in the presence of an electric should be lowered more significantly with respect to that of the hexagonal phase because of the former's higher relative permittivity, the effect arising from

the change in volume free energy should only become significant at electric field strengths in the range of MV cm^{-1} , an order of magnitude higher than the experimentally accessible fields in the present study. This suggests alternative, perhaps interface-mediated, mechanisms by which the electric field modifies the nucleation behavior of BaTiO_3 .

Introduction

Dielectric, ferroelectric and piezoelectric thin films exhibit unique properties that can be utilized in many electronic applications; however, processing temperatures must be maintained below $650\text{ }^\circ\text{C}$ for integration with platinized Si substrates. Integration issues associated with chemical and thermal incompatibility are even more severe for many flexible electronic substrates, textiles and other unique platforms. Consequently, a major goal for heterogeneous materials integration is to lower the processing temperatures, thereby slowing diffusion and reaction kinetics. Typically, however, lower processing temperatures lead to poorer crystalline quality in ceramic materials compared to those processed by standard high-temperature “bulk” routes, and thus compromise properties [1]. Arguably, one of the most significant challenges for functional ceramic electronics and devices is to lower processing temperatures while not sacrificing material properties for device performance.

The quest for enhancing microstructure development in BaTiO_3 -based materials, which are important for numerous capacitive devices, has found success in using chemical fluxes [1, 2] or nucleation layers, e.g., CuO [3], to improve the crystallinity of annealed films deposited by physical vapor deposition. These chemical approaches led to marked improvements in crystalline order and dielectric properties relative to films with no additives or nucleation layers, but they did not mitigate the need for annealing temperatures in excess of $800\text{ }^\circ\text{C}$. The present study further explores the nucleation behavior of initially amorphous BaTiO_3 films. We find that at lower annealing temperatures ($600\text{ }^\circ\text{C}$), the hexagonal phase preferentially nucleates with the stable cubic structure becoming dominant at higher annealing temperatures.

Since the preferential nucleation of the hexagonal phase at lower temperatures could impede low-temperature integration strategies, we then explore the possibility of using electric fields to modulate the relative nucleation behavior of the two phases. The basic thermodynamic

argument is that the volume free energies of the competing phases are altered in an electric field; thus, contrast in the dielectric permittivity between the phases can either lower or raise the nucleation barrier depending on the sign of the permittivity difference [4, 5]. Electric-field-assisted nucleation, while not extensively studied in the solid-state nucleation, has garnered great attention in other disciplines. The food sciences community, for example, utilizes electric fields to control nucleation of ice during freezing and has developed fundamental insight into how the electric field affects both thermodynamic and kinetic aspects of the processes [6]. This field-modified nucleation barrier has also been invoked to understand phase switching mechanisms in “phase-change” alloys, e.g., $\text{Ge}_2\text{Sb}_2\text{Te}_5$ (GST), in which the amorphous-to-crystalline phase change is driven by an electric field [7]. Furthermore, phase separation and crystallization in some glasses have been demonstrated to follow qualitatively the general thermodynamic predictions [8, 9]. However, the role of electric field is still somewhat controversial in many of these studies as the effects of Joule heating complicate the interpretation.

Based on these prior studies, we investigate the effects of DC electric field on the nucleation behavior of amorphous BaTiO_3 thin films, as a possible means to enhance the nucleation of the cubic phase relative to the hexagonal phase at lower temperatures. To decouple the effect of Joule heating from direct field effects, a non-direct contact geometry was used for these experiments in which a dielectric break prevented current flow. Crystal structure and microstructure properties were investigated as a function of applied electric field and temperature. Furthermore, a thermodynamic model for nucleation and growth was used to interpret the experimental data.

Experimental Procedure

A ceramic disk target for pulsed laser deposition (PLD) was fabricated from commercial BaTiO_3 powder (Ferro Corp., Mayfield Heights, OH) by uniaxially pressing powder, sintering at 1280 °C for 1 min, and then sintering at 1200 °C for 4 h. To deposit amorphous BaTiO_3 thin films, the distance between the BaTiO_3 target and a (0001)-face sapphire substrate was held constant at 75 mm in a PLD vacuum chamber. Substrate temperature and oxygen partial pressure were fixed at 400 °C and 30 mTorr during deposition. A KrF excimer (Coherent Compex Pro 102 F, $\lambda = 248$ nm) was used as a laser source, and the laser fluence and repetition rate were fixed to 1.5 J cm⁻² and 7 Hz, respectively.

In situ temperature-dependent X-ray diffraction (XRD) patterns were examined to observe the crystallization behavior of the amorphous BaTiO₃ thin film without the presence of an electric field. The measurement was carried out from room temperature to 900 °C with a 5 °C min⁻¹ heating rate in air on a PANalytical Empyrean (Almelo, The Netherlands) X-ray diffractometer with a Cu-Kα source and in the Bragg–Brentano geometry. The omega value was intentionally offset by 2 ° to exclude the strong substrate (0006-Al₂O₃) peak around 42 in 2θ.

Ex situ glancing incidence XRD (GIXRD) patterns were measured to refine the room-temperature crystal structure of isothermally annealed films using a Smart Lab (Rigaku, Japan) X-ray diffractometer with a Cu-Kα source. The GIXRD patterns were taken from 15 to 100 ° in 2θ with a 0.05 ° scan step and dwell time of 3 s per step. The incident beam angle for all patterns was held at 1° and thus, the penetration depth was around 115 nm. The GSAS II software was utilized to refine the patterns using the Rietveld refinement method. All patterns were carefully refined, so that the weighted residuals and goodness of fit were less than 0.11 and 2.00, respectively.

Based on the in situ XRD analysis, annealing temperatures of 500, 700 and 900 °C were selected to investigate the effects of electric field on crystallization behavior of amorphous BaTiO₃ thin films. The deposited amorphous BaTiO₃ film on c-sapphire was placed on a platinum (Pt) bottom electrode, and a fused quartz (SiO₂) cover slip was placed over the thin film as a dielectric barrier to prevent current flow. A top Pt electrode was then placed on the quartz. The electric field in the BaTiO₃ was calculated from a series circuit model with the capacitance of the c-sapphire, amorphous BaTiO₃ thin film and fused quartz. An electrometer was used to monitor any possible current flow through the sample during the process. Positive electric potential was applied to the top electrode and fixed during the annealing process. A range of electric field values, up to 0.8 kV cm⁻¹, was studied. Due to catastrophic failure of the quartz layer at 900 °C and 0.8 kV cm⁻¹, only fields up to 0.6 kV cm⁻¹ were applied at 900 °C.

Microstructure analysis of annealed films was performed using an Thermo Fisher Scientific Verios 460L field-emission scanning electron microscope (SEM). Images of film surfaces were acquired by collecting low-energy secondary electrons with an Everhart–Thornley type detector inside the column. To reduce surface charging, the accelerating voltage and sample bias conditions were set to target the low energy charge balance point with the electron landing energies varying between 1.0 and 1.5 keV. Using a 13 pA beam current with these landing energies produced the best images. Grain size measurements were performed using the linear intercept method.

Results

Crystallization behavior of amorphous BaTiO₃ thin films

Figure 1a presents in situ XRD patterns of the crystallizing BaTiO₃ films as a function of temperature. As indicated by the broad peaks around 25–30°, the as-deposited BaTiO₃ is largely amorphous and the onset of crystallization is 420 °C in ambient atmosphere. Two different crystalline phases appear with increasing temperature above 420 °C, and they are maintained to 900 °C. One is the perovskite cubic BaTiO₃ phase (c-BaTiO₃) with Pm 3 m symmetry, which is thermodynamically stable from 120 °C (the Curie temperature) to 1460 °C in air. The other is the hexagonal BaTiO₃ phase (h-BaTiO₃) with P6₃/mmc symmetry, which is the thermodynamically stable phase in bulk form from 1460 to 1625 °C in air [10]. Unlike c-BaTiO₃ which has a corner-sharing TiO₆ octahedra structure, h-BaTiO₃ has both corner-sharing TiO₆ octahedra and face-sharing Ti₂O₉ polyhedra.

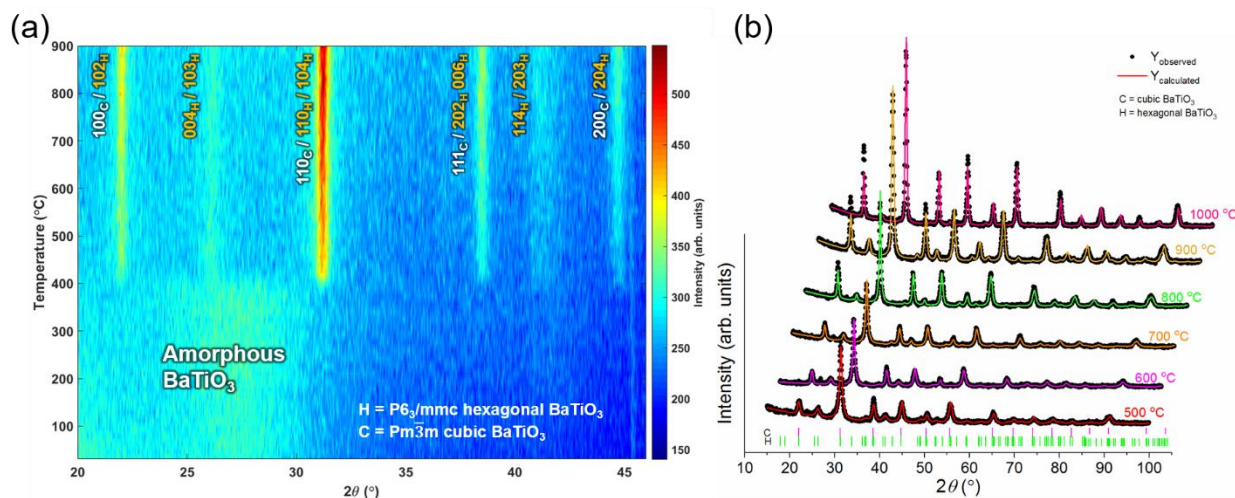


Fig. 1. (a) In-situ high-temperature x-ray diffraction patterns of amorphous BaTiO₃ film on c-sapphire. (b) Observed and fitted room temperature GIXRD patterns of BaTiO₃ films isothermally annealed at 500 °C – 1000 °C for 2 hours in air.

To investigate more quantitatively the crystallization behavior, amorphous films were isothermally annealed at temperatures between 500–1000 °C, with a ramp rate of 5 °C min⁻¹ and hold time of 2 h. The fractions of the cubic and hexagonal phases as a function of annealing

temperature were analyzed from the ex situ room-temperature GIXRD patterns via Rietveld refinement, as shown in Fig. 1b. Although the c-BaTiO₃ phase is expected to transform to tetragonal phase as it is cooled below the Curie temperature, the 0.1% tetragonality was not detectable within the relatively broad diffraction peaks, which is typical of thin-film BaTiO₃ [11, 12]; we therefore limited the fitting parameters to cubic symmetry in the Rietveld refinement. The resulting phase fractions versus the annealing temperature are plotted in Fig. 2. The hexagonal phase is predominant in the film annealed at 500 °C; however, it becomes less significant with increasing annealing temperature. Finally, the cubic phase constitutes above 85% of the film annealed at 1000 °C.

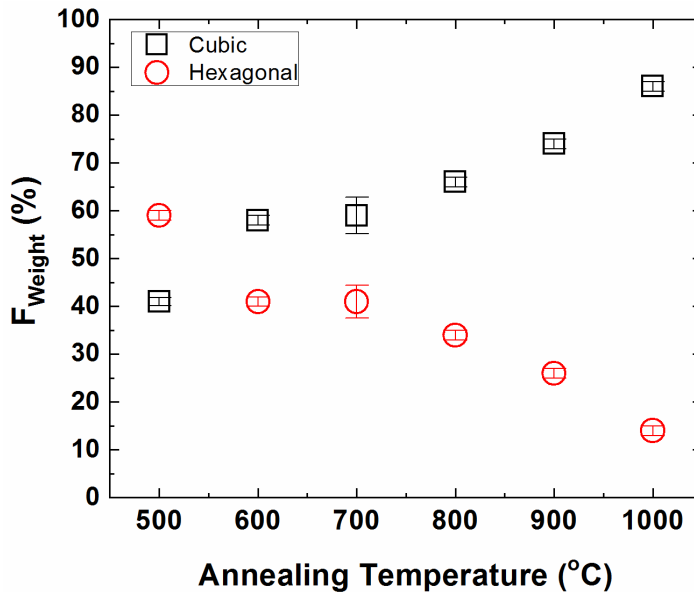


Fig. 2. Weight fraction of the cubic and hexagonal phases versus annealing temperature for 2 hour isothermal holds.

Figure 3 shows corresponding SEM images of the BaTiO₃ thin films isothermally annealed at 500, 700 and 1000 °C for 2 h in air. Small grains, 19 nm² in size, were observed in the 500 °C annealed film. At 700 °C, the grains exhibit a bimodal distribution, consisting of elongated (180 ± 49 nm) and equiaxed grains (33 ± 2 nm). The origin of the elongated grains is not clear but may be related to growth of the asymmetric hexagonal phase whose c/a is quite large (~ 2.45) [13]. Equiaxed grains are observed at annealing temperatures of 800 °C or above, with their size increasing with increasing annealing temperature, as shown in Fig. 3d. Finally, relatively dense

and large faceted grains, with an average grain size of 140 nm in size, were obtained in the 1000 °C annealed film.

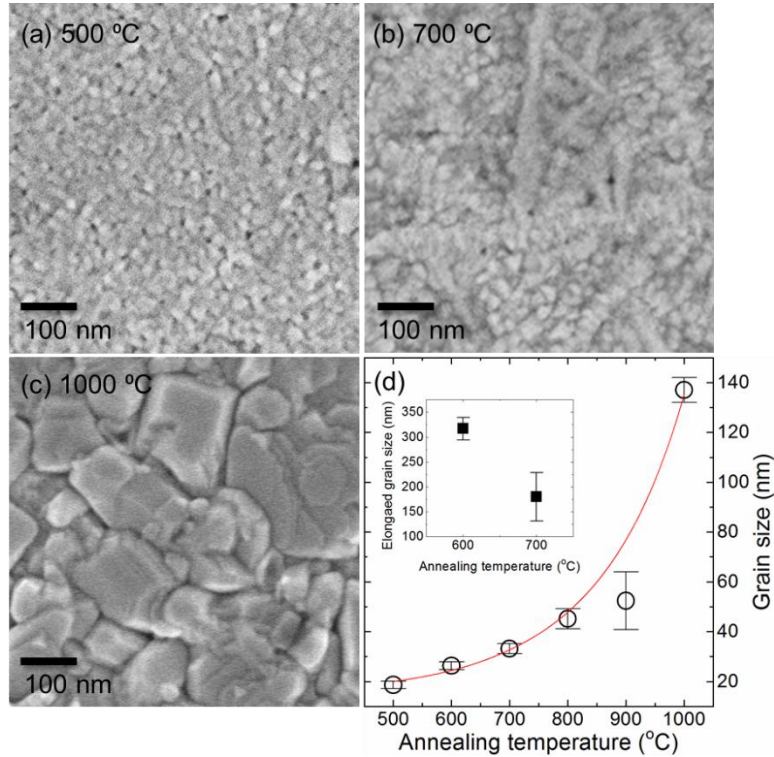


Fig. 3. Surface images of BaTiO₃ thin films isothermally annealed at (a) 500 °C, (b) 700 °C and (c) 1000 °C, and (d) grain size variation versus annealing temperature.

Phase Nucleation as a Function of Electric Field

Realizing that nucleation kinetics of the desirable cubic BaTiO₃ phase may be a fundamental limitation to low-temperature processing, we then explored the use of DC electric fields to enhance its nucleation relative to the hexagonal phase. The results of the DC biasing studies are summarized in Fig. 4. At 500 °C annealing temperature, the cubic phase fraction increased approximately linearly with increasing applied electric field, with an 18% increase from 0.41 ± 0.01 to 0.59 ± 0.01 as the electric field was increased to $0.8 \text{ kV}\cdot\text{cm}^{-1}$. The fraction of the cubic phase in the 700 °C annealed BaTiO₃, Fig. 4b, increased by 24% from 0.59 ± 0.04 to 0.70 ± 0.01 when the applied electric field increased from 0 to $0.4 \text{ kV}\cdot\text{cm}^{-1}$ and stabilized at higher field values between 0.68 ± 0.01 and 0.69 ± 0.01 . Figure 4c presents the fractions of the hexagonal and cubic phases in the 900

°C annealed BaTiO₃ films. In this case, the cubic phase fraction increased less than 10% from 0.81 ± 0.01 to 0.89 ± 0.01 from 0 to $0.4 \text{ kV}\cdot\text{cm}^{-1}$ and then slightly decreased to 0.86 ± 0.01 at $0.6 \text{ kV}\cdot\text{cm}^{-1}$. It is noteworthy that the phase ratio of the film annealed at $500 \text{ }^\circ\text{C}$ with $0.8 \text{ kV}\cdot\text{cm}^{-1}$ is very close to that of the films annealed at $700 \text{ }^\circ\text{C}$ without an electric field. Correspondingly, the microstructure of the films annealed under these conditions are also very similar (Fig. 5b and c) in terms of morphology and grain size. Furthermore, the application of a $0.4 \text{ kV}\cdot\text{cm}^{-1}$ field at $700 \text{ }^\circ\text{C}$ (Fig. 5d) leads to larger, more equiaxed and faceted grains with a dense microstructure, almost identical to that of the films annealed at $900 \text{ }^\circ\text{C}$ without an electric field (Fig. 5e).

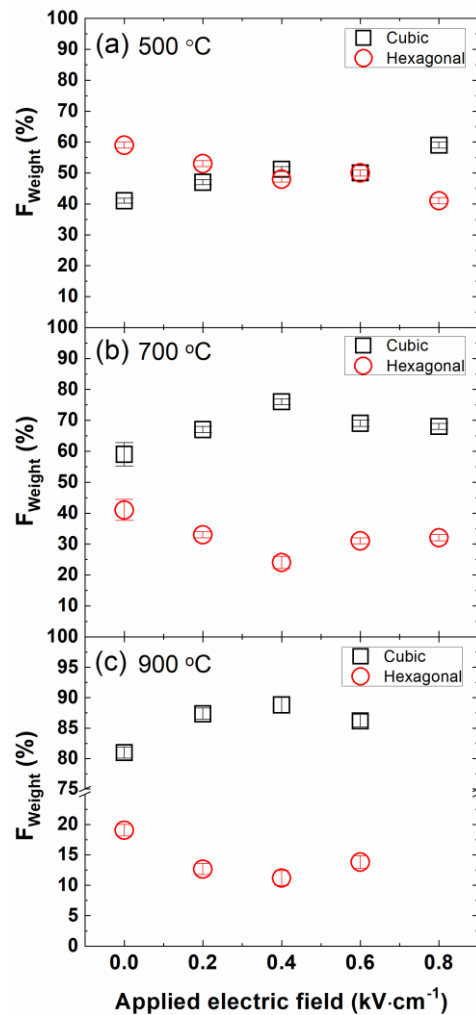


Fig. 4. Weight percent of cubic and hexagonal BT a as a function of the applied electric field in BaTiO₃ thin films during annealing process at (a) $500 \text{ }^\circ\text{C}$, (b) $700 \text{ }^\circ\text{C}$ and (c) $900 \text{ }^\circ\text{C}$.

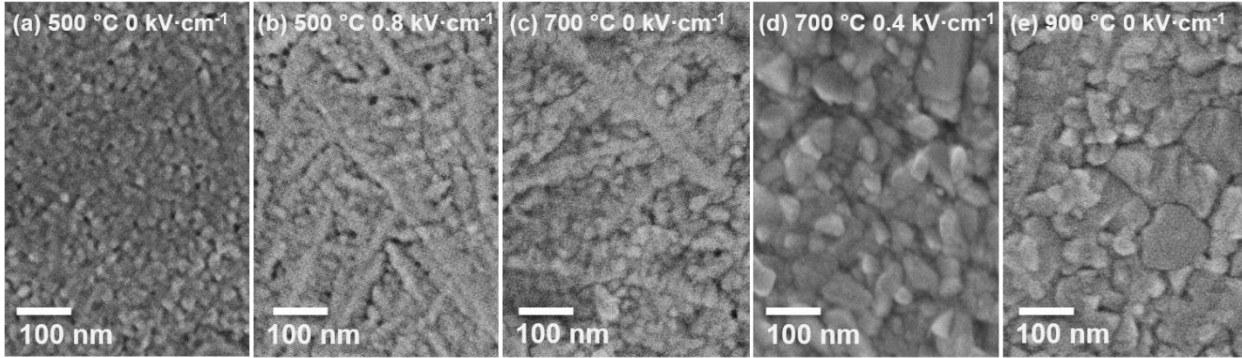


Fig. 5. SEM images of BaTiO₃ thin films after a 2 hour isothermal annealing. (a) 500 °C, 0 kV·cm⁻¹, (b) 500 °C, 0.8 kV·cm⁻¹, (c) 700 °C, 0 kV·cm⁻¹, (d) 700 °C, 0.4 kV·cm⁻¹ and (e) 900 °C, 0 kV·cm⁻¹.

Discussion

The preferential nucleation of the hexagonal BaTiO₃ phase, which is the bulk equilibrium phase only from 1460 to 1625 °C, suggests that its nucleation barrier is lower than that of the cubic phase. This may result from the fact that the hexagonal phase is of lower symmetry and lower density than the cubic phase, making it more structurally similar to the amorphous precursor. Such transient metastable nucleation phases are often observed during crystallization [14], and this general behavior is often described by Ostwald's step rule, which is attributed to the activation barrier to the metastable phase being lower, making it more kinetically accessible [15]. The present study shows that at low-temperatures, the hexagonal phase preferentially nucleates relative to the cubic phase. Given enough thermal energy, however, the stable cubic phase can be kinetically accessed and thus crystallizes and grows at higher temperatures. The effects of electric field on the both phase fraction and microstructure evolution during crystallization were apparent in the BaTiO₃ thin films. It is meaningful to discuss the possible origins of this behavior under an electric field in terms of modifications to classic nucleation theory. The change in Gibbs free energy associated with nucleation can be define as:

$$\Delta G = \Delta G_0 + \Delta W_E \quad \text{Eq. 1}$$

where ΔG_0 is change in the free energy without electric field and the additional work term ΔW_E is the free energy change due to the electric field. The ΔG_0 term is generally expressed as:

$$\Delta G_0 = 4\pi r^2 \sigma - \frac{4}{3} \pi r^3 \Delta G_V \quad \text{Eq. 2}$$

where r is the radius of a nuclei, σ is the surface free energy per unit area and ΔG_V is the change in volumetric energy per unit volume.

If a constant electrostatic potential is applied to the thin film during the process at constant T , P and no changes of phase constitution are assumed, then the free energy change induced by an electric field, ΔW_E , is given by [5]:

$$\Delta W_E = -\varepsilon_o(\bar{\varepsilon} - \varepsilon_m)E^2/8\pi n \quad \text{Eq. 3}$$

where $\bar{\varepsilon}$ is the effective relative permittivity of the medium having n nuclei per unit volume and ε_m is the relative permittivity of the matrix phase and E is the applied electric field. In this model, the shape of the cluster is assumed to be spherical, and the $\bar{\varepsilon}$ for a volume fraction δ of spherical clusters was derived by Wagner [17] and van Beek [18] as:

$$\bar{\varepsilon} = \frac{(1 - \delta)2\varepsilon_m^2 + (1 + 2\delta)\varepsilon_m\varepsilon_c}{(1 - \delta)\varepsilon_c + (2 + \delta)\varepsilon_m} \quad \text{Eq. 4}$$

where ε_c is the relative permittivity of cluster, or nucleating phase. If the total dimensions of the system during the annealing process are assumed to be constant and the total number of nuclei is held constant, then the above equation reduces to [19]:

$$\bar{\varepsilon} = \varepsilon_m[1 + 3\delta(\varepsilon_c - \varepsilon_m)/(\varepsilon_c + 2\varepsilon_m)] \quad \text{Eq. 5}$$

The fraction δ is much smaller than 1, and hence the change in free energy from the electric field is:

$$\begin{aligned} \Delta W_E(x) &= -\varepsilon_o(\bar{\varepsilon} - \varepsilon_m)E^2/8\pi n \\ &= -\frac{3}{8\pi} v_c E^2 x \varepsilon_o \varepsilon_m (\varepsilon_c - \varepsilon_m) / (\varepsilon_c + 2\varepsilon_m) \end{aligned} \quad \text{Eq. 6}$$

since $\delta = n v_c x$, where v_c is mean atom volume in the cluster and x is the size of the cluster having the relation; $x = (4\pi/3v_c)r^3$. Therefore, the total Gibbs free energy change as a function of nuclei radius is:

$$\Delta G(r) = 4\pi r^2 \sigma - \frac{4\pi}{3} \frac{H_f}{T_m} (T_m - T) r^3 - \frac{\varepsilon_o \varepsilon_m (\varepsilon_c - \varepsilon_m)}{2(\varepsilon_c + 2\varepsilon_m)} E^2 r^3 \quad \text{Eq. 7}$$

since $\Delta G_V = \frac{H_f}{T_m} (T_m - T)$ where H_f is the latent heat of fusion and T_m is the melting temperature and T is an annealing temperature.

If a relative permittivity of the nucleating cluster (ϵ_c) is larger than that of matrix (ϵ_m), the nucleation barrier and critical radius of the cluster will be decreased by the $\Delta W_E(x)$ term and therefore the nucleation process will be promoted at a given annealing temperature.

$\Delta G(r)$ in the nucleation process of our system was estimated using the thermodynamic parameters listed in the Table 1. As shown in the fig. 6, $\Delta G(r)$ at 700 °C with $E = 1 \text{ kV}\cdot\text{cm}^{-1}$ shows no significant difference in either the critical radius or energy barrier. The model shows that the difference only becomes significant at field values on the order of $10 \text{ MV}\cdot\text{cm}^{-1}$, at which point the energy barrier and critical radius of the cubic phase are lower than those of the hexagonal phase. While the model developed leading to Eq. 7 assumed a homogeneous field within the sample, ANSYS simulations (not shown here) show that the local field concentrations at the interfaces of clusters with 0.3 nm diameter can increase by a factor of 1.6 times, but this still does not account for the discrepancy between the predicted and observed critical field values. We also considered the change in Gibbs free energy with different values of H_f term since the input value ($79 \text{ kJ}\cdot\text{mol}^{-1}$) [20] is likely to be overestimated in the model, since the phase transformation in the present study is a solid-solid transformation and not a liquid-solid transformation. In a reasonable range of H_f , the calculated ΔG_0 term was highly dependent on the H_f value. However, the $\Delta W_E(x)$ term was still very small compared to ΔG_0 , and thus the effect of electric field is minor and $\text{MV}\cdot\text{cm}^{-1}$ field would still be needed to significantly affect the energy barrier and critical radius according to the model.

Table 1. Thermodynamic parameters for the free energy calculation in the nucleation process.

Parameters	Value	Unit	Reference	Note
H_f	79.6	$\text{kJ}\cdot\text{mol}^{-1}$	20	The estimated density ($4.86 \text{ g}\cdot\text{cm}^{-3}$) at melting temperature was used to convert the mole basis H_f to the volume basis H_f .
	1659	$\text{kJ}\cdot\text{cm}^{-3}$		
σ	0.22	$\text{J}\cdot\text{m}^{-2}$	25	Theoretically calculated value
T_m	1898	K		Melting temperature
ϵ_{matrix}	20	-	26	Measured at room temperature and 100 kHz
$\epsilon_{\text{cluster of cubic}}$	318	-	27	
$\epsilon_{\text{cluster of hexagonal}}$	100	-	28	

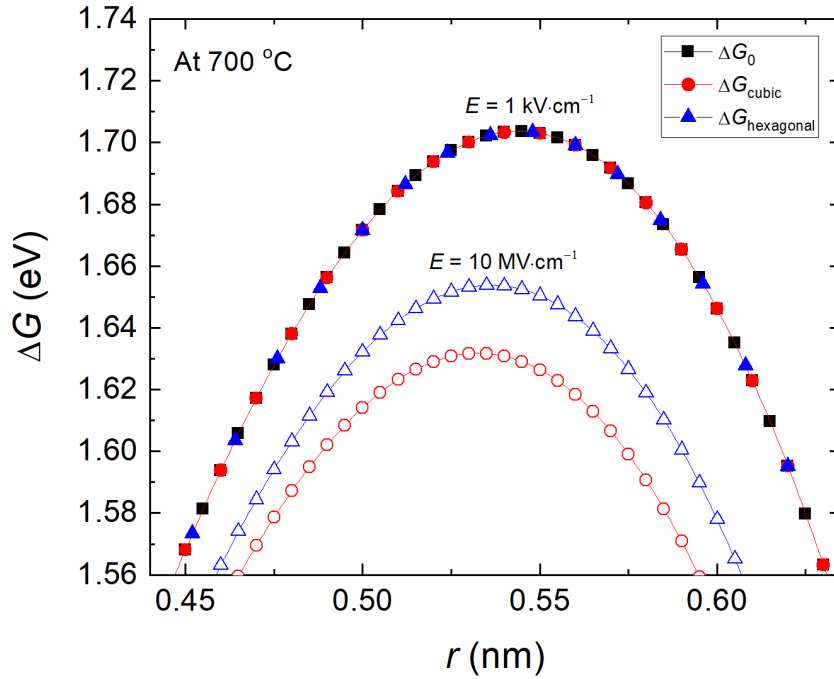


Fig. 6. Free energy change in the nucleation process as a function of cluster radius at 700 °C under $1 \text{ kV}\cdot\text{cm}^{-1}$ (solid symbols) and $10 \text{ MV}\cdot\text{cm}^{-1}$ (open symbols) electric field.

It is interesting to note that there are numerous experimental studies that show significant effects on nucleation at fields in the $\text{kV}\cdot\text{cm}^{-1}$ field range [8, 9], although these fields should be too low based off Eq. 7 alone. Even in molecular dynamics simulations of ice nucleation in which added effects of molecular rotation were introduced, the expected critical field values were on the order of $10^5 - 10^7 \text{ V}\cdot\text{cm}^{-1}$ [21]. However, two orders of magnitude lower DC electric fields ($10^3 - 10^4 \text{ V}\cdot\text{cm}^{-1}$) were experimentally observed to enhance the nucleation [6, 22-24]

In the present study the primary mechanism by which the electric field modifies the nucleation behavior remains unclear, but other factors must be also in play, such as a reduction in the interfacial energy or possible interactions of the field with charged ions or point defects.

Conclusions

Temperature-dependent phase and microstructure evolution of initially amorphous BaTiO₃ thin films was investigated to understand its crystallization behavior. Phase analysis from XRD showed that the metastable hexagonal phase preferentially nucleates at around 420 °C and this observation was explained by the rule of Ostwald step. With increasing annealing temperature, the fraction of cubic phase increases, and finally 90% cubic phase was observed at the 1000 °C annealing condition where dense and large faceted grains were obtained.

We further studied the possibility of using DC electric fields to modify the nucleation behavior. From the quantitative XRD analysis, it was confirmed that cubic phase nucleation is enhanced relative to the hexagonal phase under an electric field of the order of 1kV·cm⁻¹. While classical nucleation thermodynamics predicts that the nucleation barrier for cubic phase is lowered relative to the hexagonal phase because of the former's higher relative permittivity, the predicted magnitude of DC electric field in the model is orders of magnitude larger than those field used in the present study. Thus, we conclude that the electric field may influence other factors such as an interfacial energy or the mobility of ions or defects at the transformation front during nucleation process.

Acknowledgements

This work was performed in part at the Analytical Instrumentation Facility (AIF) at North Carolina State University, which is supported by the State of North Carolina and the National Science Foundation (award number ECCS-1542015). The AIF is a member of the North Carolina Research Triangle Nanotechnology Network (RTNN), a site in the National Nanotechnology Coordinated Infrastructure (NNCI). This work was partially supported by the II-VI Foundation under the Block-Gift Program.

Compliance with ethical standards

Conflicts of interest: The authors declare that they have no conflict of interest.

References

- [1] Ihlefeld JF, Borland WJ, Maria J-P (2007) Enhanced Dielectric and Crystalline Properties in Ferroelectric Barium Titanate Thin Films. *Adv Funct Mater* 17:1199–1203.
- [2] Harris DT, Burch MJ, Ihlefeld JF, et al (2013) Realizing strain enhanced dielectric properties in BaTiO₃ films by liquid phase assisted growth. *Appl Phys Lett* 103:012904-1–5.
- [3] Harris DT, Burch MJ, Mily EJ, et al (2016) Microstructure and dielectric properties with CuO additions to liquid phase sintered BaTiO₃ thin films. *J Mater Res* 31:1018–1026.
- [4] Kashchiev D (1972) On the influence of the electric field on nucleation kinetics. *Philos Mag* 25:459–470.
- [5] Isard JO (1977) Calculation of the influence of an electric field on the free energy of formation of a nucleus. *Philos Mag* 35:817–819.
- [6] Orłowska M, Havet M, Le-Bail A (2009) Controlled ice nucleation under high voltage DC electrostatic field conditions. *Food Res Int* 42:879–884.
- [7] Nardone M, Karpov VG, Jackson DCS, Karpov I V. (2009) A unified model of nucleation switching. *Appl Phys Lett* 94:103509-1–3.
- [8] Gu XM, Liu W, Liang KM (2000) The effect of electric field on phase separation in glasses: A model and experimental testing. *Mater Sci Eng A* 278:22–26.
- [9] Liu W, Liang KM, Zheng YK, et al (1997) The effect of an electric field on the phase separation of glasses. *J Phys D Appl Phys* 30:3366–3370.
- [10] Lee S, Randall CA, Liu ZK (2007) Modified phase diagram for the barium oxide-titanium dioxide system for the ferroelectric barium titanate. *J Am Ceram Soc* 90:2589–2594.
- [11] Kim S, Hishita S (1997) Preparation and characterization of BaTiO₃ thin films on MgO-buffered Si(100) substrates by RF sputtering. *J Mater Res* 12:1152–1159.
- [12] Appleby DJR, Ponon NK, Kwa KSK, et al (2014) Ferroelectric properties in thin film barium titanate grown using pulsed laser deposition. *J Appl Phys* 116:124105-1–6.
- [13] Akimoto J, Gotoh Y, Oosawa Y (1994) Refinement of hexagonal BaTiO₃. *Acta Crystallogr Sect C Cryst Struct Commun* 50:160–161.
- [14] Chung SY, Kim YM, Kim JG, Kim YJ (2009) Multiphase transformation and Ostwalds rule of stages during crystallization of a metal phosphate. *Nat Phys* 5:68–73.
- [15] Nývlt J (1995) The Ostwald Rule of Stages. *Cryst Res Technol* 30:443–449.

- [16] Kashchiev D (2000) Chapter 21. Electric field. In: Nucleation. Elsevier, pp 315–329
- [17] K. W. Wagner (1914) Erklärung der dielektrischen Nachwirkungsvorgänge auf Grund Maxwellscher Vorstellungen. Arch für Elektrotechnik 2:371
- [18] Beek V, L.K.H. (1967) Dielectric behaviour of heterogeneous systems. In: J.B. Birks (ed) Progress in Dielectrics. Heywood Books, London, pp 69–114
- [19] Grossman DG, Isard JO (1970) The application of dielectric mixtures formulae to glass - ceramic systems. J Phys D Appl Phys 3:1058–1067.
- [20] Lee KJ, Lee CH, Lee GW, et al (2012) Thermophysical properties of BaTiO₃ ceramics prepared by aerodynamic levitation. Thermochim Acta 542:37–41.
- [21] Vegiri A, Schevkunov S V. (2001) A molecular dynamics study of structural transitions in small water clusters in the presence of an external electric field. J Chem Phys 115:4175–4185.
- [22] Wei S, Xiaobin X, Hong Z, Chuanxiang X (2008) Effects of dipole polarization of water molecules on ice formation under an electrostatic field. Cryobiology 56:93–99.
- [23] Hozumi T, Saito A, Seiji O, Kazuharu W (2003) Effects of electrode materials on freezing of supercooled water in electric freeze control. Int J Refrig 26:537–542.
- [24] Hozumi T, Saito A, Okawa S, Eshita Y (2005) Effects of shapes of electrodes on freezing of supercooled water in electric freeze control. Int J Refrig 28:389–395.
- [25] Testino A, Buscaglia V, Buscaglia MT, et al (2005) Kinetic modeling of aqueous and hydrothermal synthesis of barium titanate (BaTiO₃). Chem Mater 17:5346–5356.
- [26] Golego N, Studenikin S a, Cocivera M (1998) Properties of Dielectric BaTiO₃ Thin Films Prepared by Spray Pyrolysis. Chem Mater 10:2000–2005.
- [27] Lee B, Zhang J (2001) Preparation, structure evolution and dielectric properties of BaTiO₃ thin films and powders by an aqueous sol-gel process. Thin Solid Films 388:107–113.
- [28] Hashemizadeh S, Biancoli A, Damjanovic D (2016) Symmetry breaking in hexagonal and cubic polymorphs of BaTiO₃. J Appl Phys 119:094105.